$5

QEX

March/April 2016

www.arrl.org

A Forum for Communications Experimenters

Issue No. 295

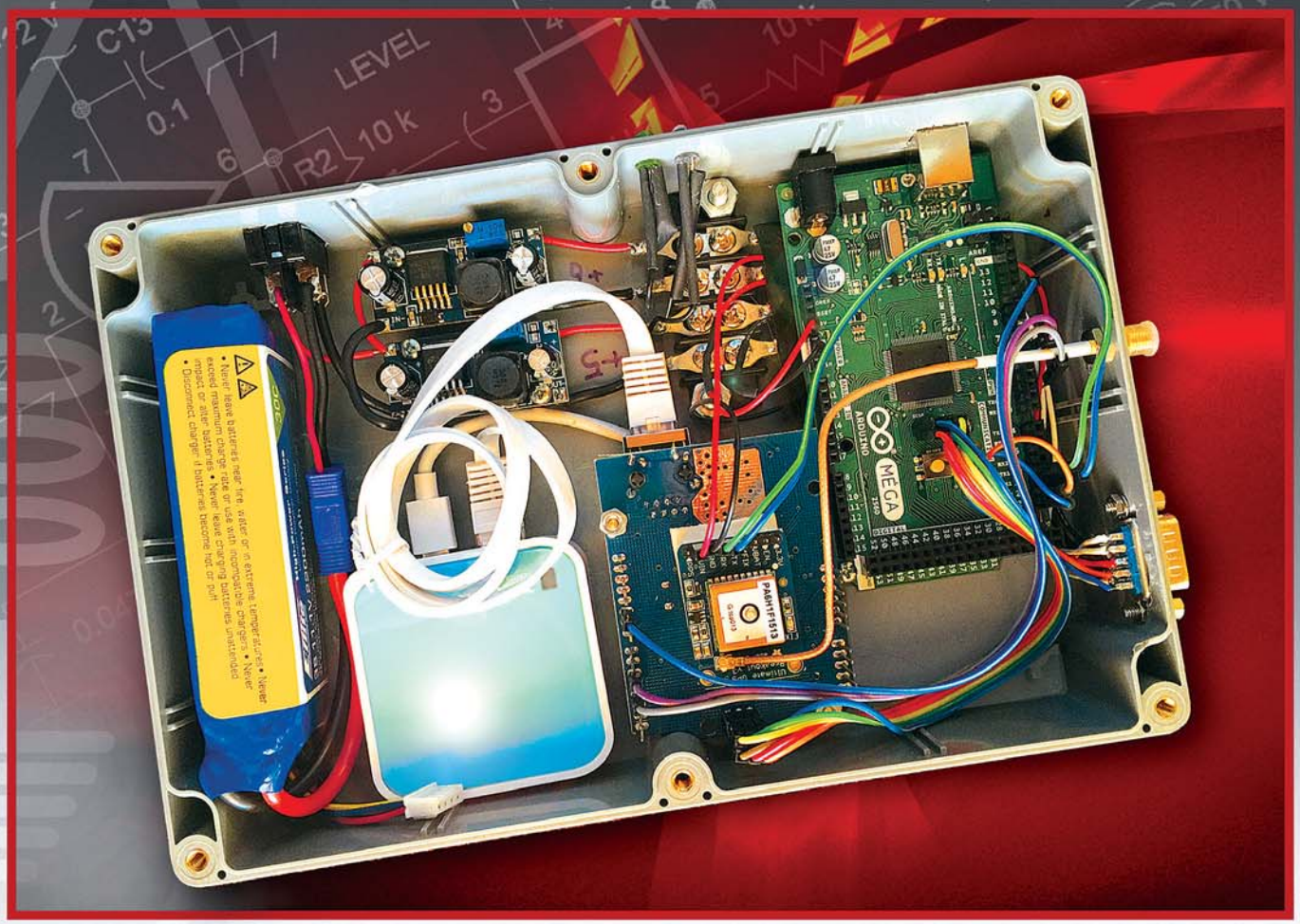

WBØOEW, shows us how to track Earth orbiting satellites using a two-axis satellite tracker that senses its spatial orientation with respect to Earth's surface, and requires no orientation setup or calibration of any kind.

ARRL *AMATEUR RADIO*™
The national association for
225 Main Street
Newington, CT USA 06111-1494

Taking HF By Storm

The TS-480HX

KENWOOD

Customer Support: (310) 639-4200
Fax: (310) 537-8235

Scan with your phone to download TS-480HX brochure.

www.kenwood.com/usa

ISO9001 Registered
JVCKENWOOD Corporation

ADS#27315

QEX (ISSN: 0886-8093) is published bimonthly in January, March, May, July, September, and November by the American Radio Relay League, 225 Main Street, Newington, CT 06111-1494. Periodicals postage paid at Hartford, CT and at additional mailing offices.

POSTMASTER: Send address changes to: QEX, 225 Main St, Newington, CT 06111-1494 Issue No 294

Harold Kramer, WJ1B
Publisher

Kazimierz "Kai" Siwiak, KE4PT
Editor

Lori Weinberg, KB1EIB
Assistant Editor

Zack Lau, W1VT
Ray Mack, W5IFS
Contributing Editors

Production Department

Steve Ford, WB8IMY
Publications Manager

Michelle Bloom, WB1ENT
Production Supervisor

Sue Fagan, KB1OKW
Graphic Design Supervisor

David Pingree, N1NAS
Senior Technical Illustrator

Brian Washing
Technical Illustrator

Advertising Information Contact:

Janet L. Rocco, W1JLR
Business Services
860-594-0203 – Direct
800-243-7768 – ARRL
860-594-4285 – Fax

Circulation Department

Cathy Stepina, *QEX Circulation*

Offices

225 Main St, Newington, CT 06111-1494 USA
Telephone: 860-594-0200
Fax: 860-594-0259 (24 hour direct line)
e-mail: **qex@arrl.org**

Subscription rate for 6 issues:

In the US: ARRL Member $24, nonmember $36;

US by First Class Mail:
ARRL member $37, nonmember $49;

International and Canada by Airmail: ARRL member $31, nonmember $43;

Members are asked to include their membership control number or a label from their QST when applying.

In order to ensure prompt delivery, we ask that you periodically check the address information on your mailing label. If you find any inaccuracies, please contact the Circulation Department immediately. Thank you for your assistance.

About the Cover

Elwood Downey, WBØOEW, designed a two-axis satellite tracker system that needs no prior alignment with respect to Earth's surface. The tracker relies on a 9-degree-of-freedom sensor attached to the antenna boom, and to a GPS receiver. The system tracks an Earth orbiting satellite in real-time with an accuracy of 2 degrees.

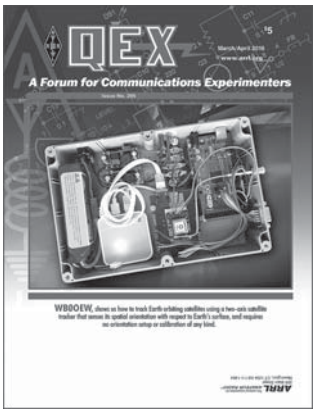

In This Issue

Features

Index of Advertisers

The American Radio Relay League

The American Radio Relay League, Inc, is a noncommercial association of radio amateurs, organized for the promotion of interest in Amateur Radio communication and experimentation, for the establishment of networks to provide communications in the event of disasters or other emergencies, for the advancement of the radio art and of the public welfare, for the representation of the radio amateur in legislative matters, and for the maintenance of fraternalism and a high standard of conduct.

ARRL is an incorporated association without capital stock chartered under the laws of the state of Connecticut, and is an exempt organization under Section 501(c)(3) of the Internal Revenue Code of 1986. Its affairs are governed by a Board of Directors, whose voting members are elected every three years by the general membership. The officers are elected or appointed by the Directors. The League is noncommercial, and no one who could gain financially from the shaping of its affairs is eligible for membership on its Board.

"Of, by, and for the radio amateur," ARRL numbers within its ranks the vast majority of active amateurs in the nation and has a proud history of achievement as the standard-bearer in amateur affairs.

A *bona fide* interest in Amateur Radio is the only essential qualification of membership; an Amateur Radio license is not a prerequisite, although full voting membership is granted only to licensed amateurs in the US.

Membership inquiries and general correspondence should be addressed to the administrative headquarters:

ARRL
225 Main Street
Newington, CT 06111 USA
Telephone: 860-594-0200
FAX: 860-594-0259 (24-hour direct line)

Officers

President: KAY C. CRAIGIE, N3KN
570 Brush Mountain Rd, Blacksburg, VA 24060

Chief Executive Officer: DAVID SUMNER, K1ZZ

The purpose of *QEX* is to:

1) provide a medium for the exchange of ideas and information among Amateur Radio experimenters,

2) document advanced technical work in the Amateur Radio field, and

3) support efforts to advance the state of the Amateur Radio art.

All correspondence concerning *QEX* should be addressed to the American Radio Relay League, 225 Main Street, Newington, CT 06111 USA. Envelopes containing manuscripts and letters for publication in *QEX* should be marked Editor, *QEX*.

Both theoretical and practical technical articles are welcomed. Manuscripts should be submitted in word-processor format, if possible. We can redraw any figures as long as their content is clear. Photos should be glossy, color or black-and-white prints of at least the size they are to appear in *QEX* or high-resolution digital images (300 dots per inch or higher at the printed size). Further information for authors can be found on the Web at **www.arrl.org/qex/** or by e-mail to **qex@arrl.org**.

Any opinions expressed in *QEX* are those of the authors, not necessarily those of the Editor or the League. While we strive to ensure all material is technically correct, authors are expected to defend their own assertions. Products mentioned are included for your information only; no endorsement is implied. Readers are cautioned to verify the availability of products before sending money to vendors.

Kazimierz "Kai" Siwiak, KE4PT

Perspectives

A Change at the Helm

Starting with this issue, *QEX* will be guided by a new Editor. My name is Kazimierz "Kai" Siwiak, KE4PT. My professional career includes electrical engineering, applied research, intellectual property analysis, and consulting in various technical aspects of the radio arts, as well as early work on RF safety. I've authored several engineering text books and patents, and have published many peer-reviewed technical papers in the professional literature. Yet, I draw the greatest pleasure from reading, authoring and editing Amateur Radio articles. My *vocation* has closely followed my Amateur Radio avocation.

In my half-century participation in Amateur Radio, I have supported the Amateur Radio activities and equipment for the *Shuttle* (later *Space*) *Amateur Radio Experiment* (SAREX). Later the HF DXing bug bit me, then low-power portable operations caught my fancy. More recently I've developed a taste for EME operations. You'll find me listed as an ARRL Contributing Editor for *QST*, and as a Member of the *ARRL RF Safety Committee*. I have served on national and international standards bodies, including as a member of the US Delegation to several ITU-R conventions, where I met ARRL representatives who spoke on behalf of Amateur Radio. Indeed, my *avocation* closely parallels my vocation.

While the outlook for *QEX* is empirical, there is a corresponding theoretical perspective. This is well illustrated in the current issue. Since we integrate empirical and theoretical views, a new title for this column has emerged – *Perspectives*. This does not affect the excellent articles that are in the publishing queue. For that matter, the content of *QEX* is driven largely by input from you, the readers. We want your opinions about what you would like to read in *QEX*. The most dramatic way to express that opinion is by authoring articles. Don't worry about whether your proposed article is a fit for *QEX* or another ARRL publication, and don't worry about being either too technical or too simple. You'll find eye-glazing equations describing the physics of radio in *QEX* and also in *QST*, I promise! The ARRL Staff and Technical Advisors will sort out the perfect venue for your article from among the ARRL family of publications.

We value your feedback, comments and opinions about these pages. After all, *QEX* is a forum for the free exchange of ideas among communications experimenters. The content is driven by you, the reader and prospective author. If you don't write it, we can't publish it. So please, put your favorite topic or innovative measurement on paper, and share it on these pages! Just follow the details on the **www.arrl.org/qex-author-guide** web page, and contact us at **qex@arrl.org**.

In this issue we touch upon several aspects of Amateur Radio — from circuit behavior, to antenna design, to the directing of radiated energy. Dr. Ulrich L. Rohde, N1UL, shares a detailed mathematical treatment of the calculation of FM and AM noise signals of Colpitts oscillator circuits. Robert J. Zavrel Jr., W7SX, investigates the mechanisms for the formation of the radiated elevation angle pattern in ground-mounted vertical antennas. Al Christman, K3LC, shows how to improve the performance of a quarter-wave radiator by adding parasitic elements to form a vertically-polarized Yagi array that is contained entirely within the same foot print as the radiator. Finally, Elwood Downey, WBØOEW, takes us through the details of a two-axis satellite tracker that relies entirely on built-in spatial sensors and needs no prior alignment with respect to the Earth's surface. In future issues we will continue to see the very fine columns *SDR Simplified* by Ray Mack, W5IFS, and *Hands on SDR* by Scotty Cowling, WA2DFI. Where appropriate we will re-print important articles from other Amateur Radio forums.

I'll finish by quoting Larry Wolfgang, WR1B, the previous Editor of these pages, "Please continue to support *QEX*, and help it remain a strong technical publication."

73,

Kazimierz "Kai" Siwiak, KE4PT

Elwood Downey, WBØOEW

8274 N Sunset Ranch Loop, Tucson, AZ, 85743-8201: **ecdowney@ClearSkyInstitute.com**

Autonomous Satellite Tracker

This two-axis tracker needs no prior alignment with respect to the Earth's surface, and tracks satellites with high accuracy entirely by reference to built-in spatial sensors.

This paper describes a completely autonomous Earth satellite tracking mount. In conjunction with a 9-DOF (degrees of freedom) sensor attached to the antenna boom and a GPS receiver, the 2-axis gimbal will track any Earth satellite within 2 degrees in real time without any orientation setup calibration of any kind. The Tracker system includes a built-in web server and Wi-Fi access point, which allows all monitoring, command and TLE upload from any web browser including smart phone. All components are off-the-shelf so no custom electronics, machining or other skills are required except that needed to attach an antenna boom to a flat plate. All electronics can be powered from a single dc supply from 7 to 18 V such as a LiPo battery pack or solar charging system. As of the time of writing, total cost of the electronics and gimbal is approximately $350, not including antenna.

Introduction

Observers have been tracking Earth satellites with gimbal mounts since the beginning of the space age.[1] One of the challenges has always been to align these mounts so the theoretical calculations of satellite azimuth and elevation could be transformed to the mount coordinate system. After reading about the availability of low cost MEMS devices that directly measure spatial orientation, I wanted to build a mount that avoided the tedious calibration step by measuring directly the pointing direction of the payload.[2]

Going one step further, I also wanted to eliminate the need to have any prior knowledge of — or make assumptions about — the gimbal geometry, axis orthogonality, motor assignment and axis rotation angles. Doing so would simplify the mechanical requirements of the gimbal and wiring, and allow the use of simple off-the-shelf hobby servo motors and robot hardware for use with light weight antennas.

The final goal was the ability to control and monitor the entire system from my smart phone without needing to first install an app. The most flexible way to accomplish this is by providing a web server, so I needed enough memory in the controller to accomplish this.

Achieving the Goals

The first goal is achieved by measuring the spatial orientation of the antenna directly using a combination of 3D magnetic, accelerometer and gyroscope sensors. When packaged together, these devices are referred to as having 9 Degrees-of-Freedom, or simply 9-DOF sensors. The magnetic sensor provides the direction of the local magnetic field, including tilt. This is combined with knowledge of the local vertical gravity vector from the accelerometer to produce local elevation and azimuth with respect to magnetic north. To get a bearing from true north, the latitude and longitude from the GPS is combined with the *World Magnetic Model* to compute the local magnetic declination correction factor.[3] Information from the gyroscope provides additional stability and repeatability information. The final correction is to apply a simple model for atmospheric refraction to elevation based on nominal assumptions for air temperature and pressure. Although these too could be measured quite easily, the maximum effect at the horizon is about one-half degree, which I decided was not worth refining further. Taken together, these measurements provide an absolute measure of antenna direction in the local horizon coordinate system, which is exactly what is produced by the orbit propagator.

Now that we have the measured antenna direction and a computed predicted direction from the propagator in the same coordinate system, the second goal is to drive the gimbal motors in such as way as to reduce any difference between the two. Normally this is done in closed-form by using a transformation matrix determined ahead of time that relates the gimbal axis coordinates to the local horizon coordinates. In order to eliminate the need for determining this matrix, my second goal is achieved by moving the motors by a small amount and just measuring whether the error increases or decreases. This is known as a gradient descent search.[4]

My first attempt at an error metric was to use the great circle distance between the measured and computed positions. However, this leads to a condition known as gimbal lock if the gimbal ends up pointing near the zenith, either intentionally because the satellite pass was high or zenith was reached unintentionally during the search procedure.[5] This is avoided if the errors in azimuth and elevation are measured separately.

The final tracking algorithm can be summarized as follows:

Step 1 – choose one axis motor at random

Step 2 – measure error in azimuth and elevation separately

Step 3 – move the current motor a small amount and stop

[1]Notes appear on page 9.

Figure 1 — Tracker gimbal is attached to a tripod and supports an Elk 2m/70cm LPDA antenna.

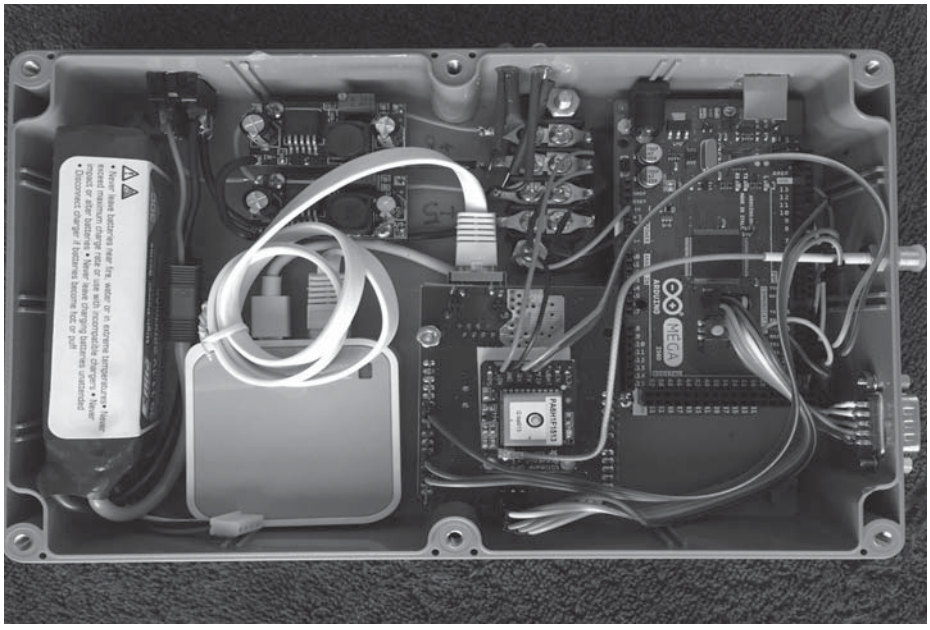

Figure 2 — Inside view of the Tracker electronics box.

Step 4 – measure the two errors again
Step 5 – if either error increased, reverse the last move and start using the other motor
Step 6 – go to Step 3, repeating forever.

Note that this does not require any knowledge of the gimbal orientation or even what motor operates what axis. The effect is the antenna will make a few small random moves to get started, then one motor will march along steadily until it causes one or the other error measures to increase. Then the other motor will do the same and the process repeats until the antenna is pointing at the satellite. This process repeats forever. So, as the satellite moves, the errors creep up and the algorithm keeps working to reduce them. The smoothness of the motion depends on the time between moves and the angle commanded for each move. These are not critical during a large slew but some care is needed in order to maintain smooth tracking performance. A rigorous approach is not required. It is easy to set reasonable values using trial and error. The algorithm could be made more efficient by introducing control-loop equations for proportional gain, so large errors are reduced more quickly, and integral gain to maintain closer tracking tolerances, but in practice these refinements are not really necessary.

The Web Server

The web server turned out to be straight forward. I already know Javascript, HTML and the HTTP headers that are used between browser and server so I wrote my own server state machine from scratch on top of the basic Arduino Ethernet library. The main page is sent, in effect, as the default *index.html* for the server URL address. All state variables are updated and reported using a consistent NAME=VALUE syntax, where the NAME usually matches the HTML name of the corresponding DOM display element. Setting a new value is performed with a POST command and retrieving values is done by asking for *getvalues.html*. An XMLHttpRequest polls for values to keep the web page updated. More details about using the web interface are provided later.

Implementation Decisions

Figure 1 shows the Tracker gimbal attached to a tripod and supporting an Elk 2 m/70 cm LPDA antenna. Figure 2 shows the inside view of the Tracker electronics box. Figure 3 is a block diagram showing how each electronic subsystem interconnects. Table 1 shows the major bill of materials.

Next, I elaborate the role of each component and share my experiences that

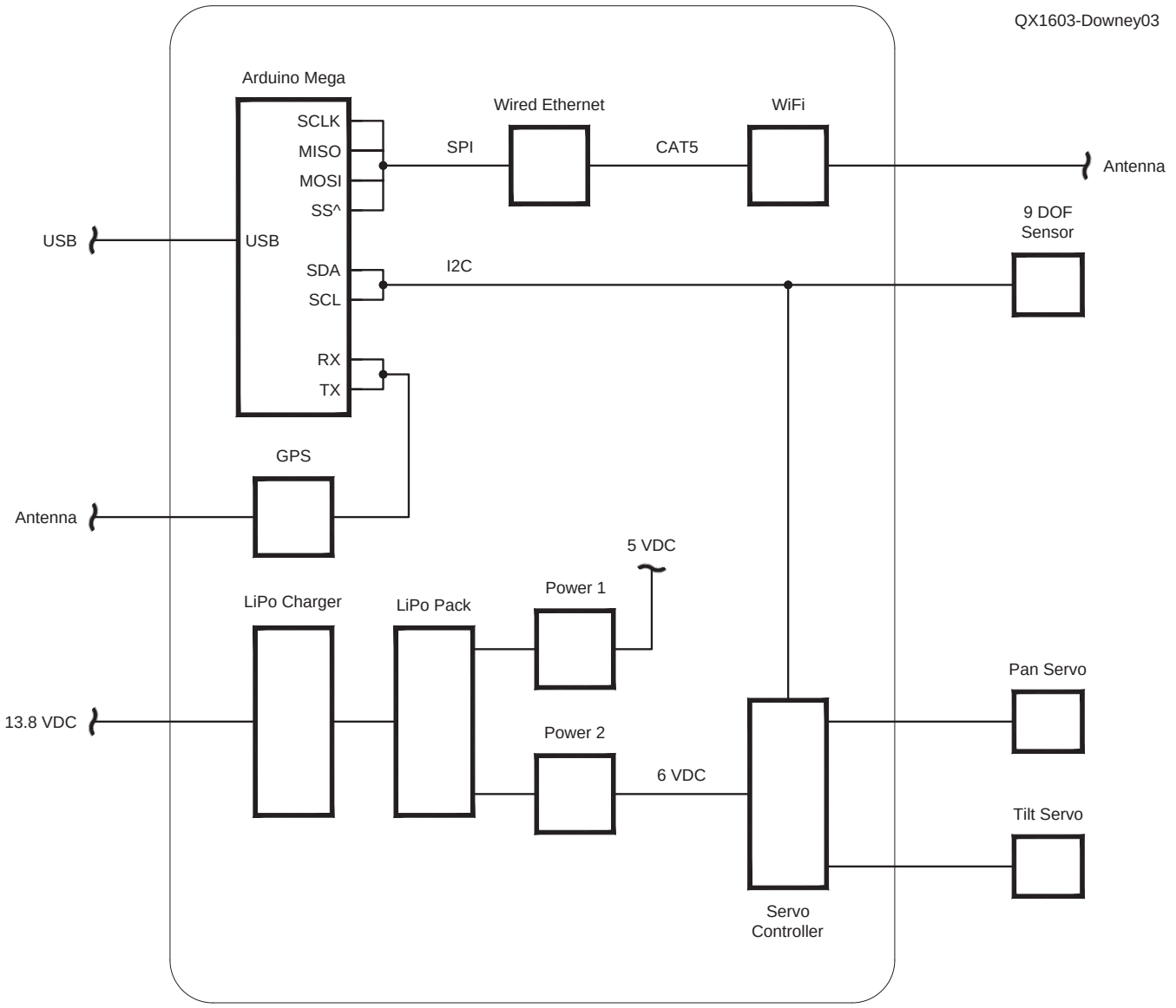

Figure 3 — Block diagram showing how each electronic subsystem interconnects. A partial bill of materials is in Table 1.

Table 1
Bill of Materials

Item	*Source*	*Approximate price*
Ardunio Mega 2560	Amazon: SunFounder Mega 2560 R3, stock number B00D9NA4CY	$18
Wired Ethernet shield	Amazon: SunFounder Ethernet Shield W5100 for Arduino, stock number B00HG82V1A	$16
Wi-Fi router	Amazon: TP-LINK TL-WR702N Wireless N150 Travel Router, stock number B007PTCFFW	$20
GPS module	Adafruit: Part ID 746	$40
Servo controller	Adafruit: Part ID 815	$15
Bosch 9 DOF sensor	Adafruit: Part ID 2472	$35
Pan platform	ServoCity: model SPG785A-CM, 5:1 ratio	$100
Tilt stage	ServoCity: model SPT400, 5:1 ratio	$95
	Total	*$339*

lead to each choice. The main processor is the Arduino Mega 2560. I began with the model Uno but eventually I could no longer squeeze everything into its 32 KB flash memory and 4 KB RAM storage. The Mega has 8 times as much flash memory and twice as much RAM, which is plenty. The Tracker uses about half of the Flash on the Arduino Mega for code and constant strings, and about half of the RAM for mutable variables, leaving 4 KB of RAM for stack.

To control the two hobby servo motors I initially used the Adafruit software servo library. However, the servos did not move smoothly. The cause turned out to be interference to the pulse timing by other libraries that lock out interrupts, even briefly. Servo position is directly related to pulse duration, which is sensitive to changes on the order of a few microseconds, so it doesn't take much timing change to cause unwanted motion. The solution My solution was the 12 channel servo controller from Adafruit. This offloads all the timing from the Arduino and requires only a two-wire connection using the I2C bus to issue the desired pulse length for each channel. It also has the added benefit that the servos actively hold position until a new command is issued.

I chose the Bosch BNO055 9-DOF sensor. It is available on a convenient breakout board from Adafruit and is compatible with their *Sensors* library. The advantage of this sensor package is it includes an onboard processor that performs all the consolidation of the three sensors automatically and outputs directly its absolute spatial orientation as Euler angles interpreted here as azimuth, elevation and roll.[6] As anyone who has tried to manually fuse together these types of sensors knows, this saves quite a lot of tedious mathematics. This sensor also connects to the Arduino using the same I2C bus as the servo controller but does not interfere because they each have a separate bus address.

I chose the GPS module from Adafruit. It has a built in antenna, which works pretty well, but I also allowed for the connection of an external antenna if necessary. This module communicates with the Arduino using a UART, or serial connection. This revealed an additional advantage to using the Arduino Mega: it has four hardware serial ports available, allowing one to be dedicated to the GPS. The Uno only has one that already serves duty with the USB boot loader. A software serial library could be used with the Uno to use other pins but at the expense of higher overhead and a more limited bandwidth.

I wanted Wi-Fi ability so I could control the system from my smart phone. I tried several Wi-Fi modules and shields but found none to be reliable. Even the best one from Adafruit would work for a random time, anywhere from seconds to hours, and then just mysteriously stop. In stark contrast, all models I tried of wired Ethernet proved to be 100% reliable, even including the oldest modules that use the WizNet W5100, so I ended up using a generic version made

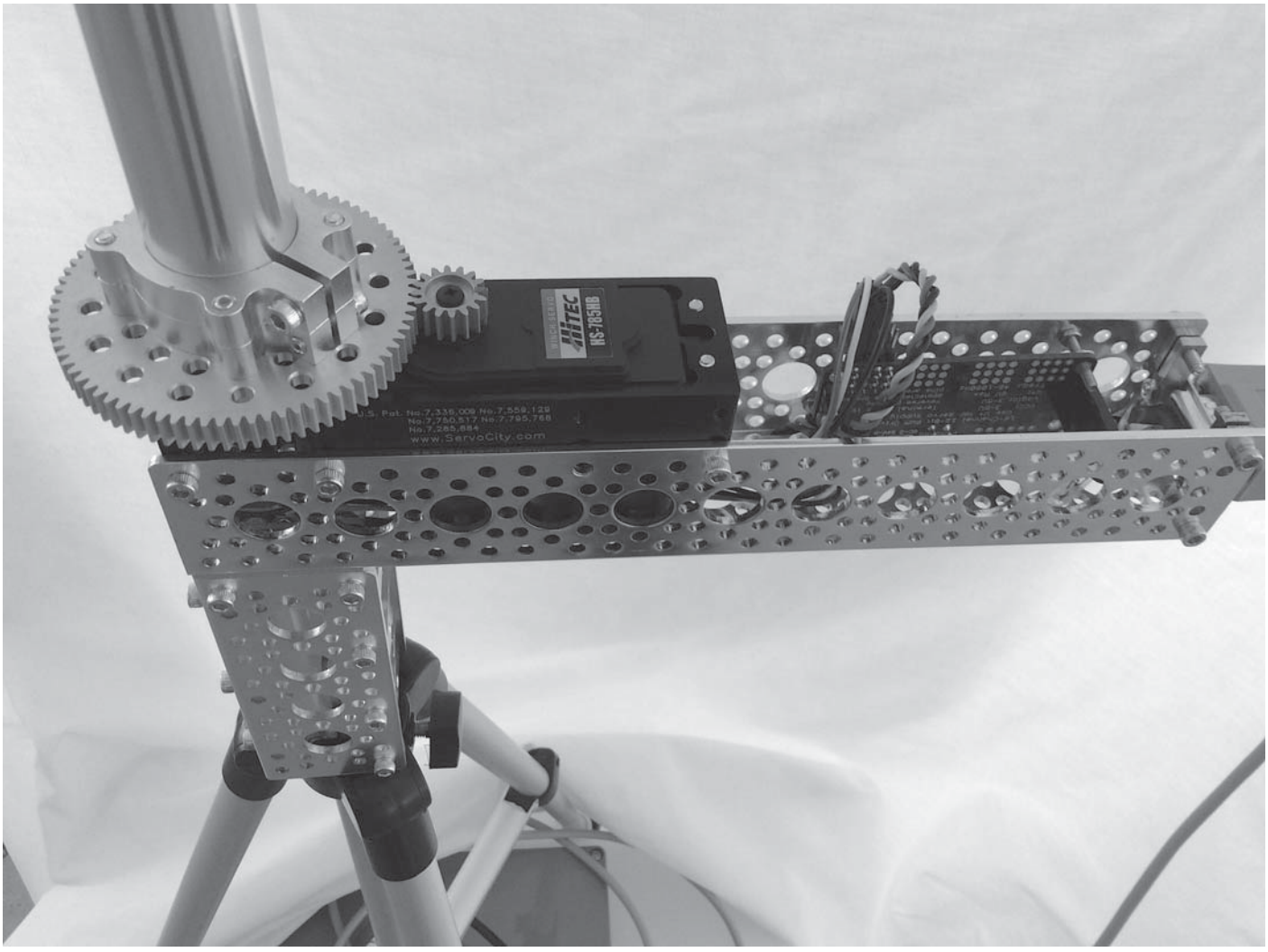

Figure 4 — The azimuth gimbal mounted on a tripod.

by Sunfounder. In order to accomplish my goal for Wi-Fi, I just connected the wired Ethernet directly to a $20 Wi-Fi adaptor made by TP-Link. This combination works beautifully. I have not experienced a single wireless communication glitch. The adaptor I bought can be configured either as its own Access Point to broadcast a separate Wi-Fi network just for the Tracker, or it can transparently bridge the Arduino to an existing Wi-Fi network. The unit comes with a simple Windows utility to perform the required one-time setup. From then on it comes up on its own every time.

I wanted everything to operate from one self-contained power source. I ended up using one LiPo battery and two separate power conditioning modules. One supplies 5 V to the Arduino and its peripherals, and the other is dedicated to powering the servo motors. This approach provides clean power to the electronics and isolates the wide load swings and voltage spikes that occur from the motors. I currently use a 7.4 V 2000 mAh pack, which operates the Tracker for several days of moderate use before needing a recharge. If desired, a solar pack could also easily be used.

The gimbal is one channel-mount pan platform (Figure 4) and one tilt platform (Figure 5) obtained from **ServoCity.com**. Together these provide about 400 degrees of azimuth motion and 135 degrees of elevation motion. Under the pan platform I installed a short section of channel with ¼-20 threaded screw plates for easy attachment to a common camera tripod. The pan platform has a hollow shaft that simplifies cabling to the 9-DOF sensor and tilt motor, and reduces tangles during rotations. I discovered that the servos would make spontaneous and sporadic moves while I am transmitting on 2 m FM with the Elk LPDA antenna. I eliminated this interference by using shielded STP CAT5 cable, taking care that only the end of the shield nearest the Arduino was connected to ground.

Assuming the Bosch spatial sensor is accurately aligned with the antenna, the largest contribution to pointing error is the sensor itself, which claims a maximum magnetic heading error of ±2.5 degrees. The next largest source of error is the orbit propagator software. The code, available in the *QEX files* web page, used here is based on a very clean rendering by Mark VandeWettering, K6HX, of the James Miller, G3RUH, *PLAN-13* code.[7,8,9] After the updates to the solar elements posted in 2014 the code produces topo-centric values within 0.2 degrees compared to a more rigorous *SGP4* code within a few days of the TLE epoch.[10]

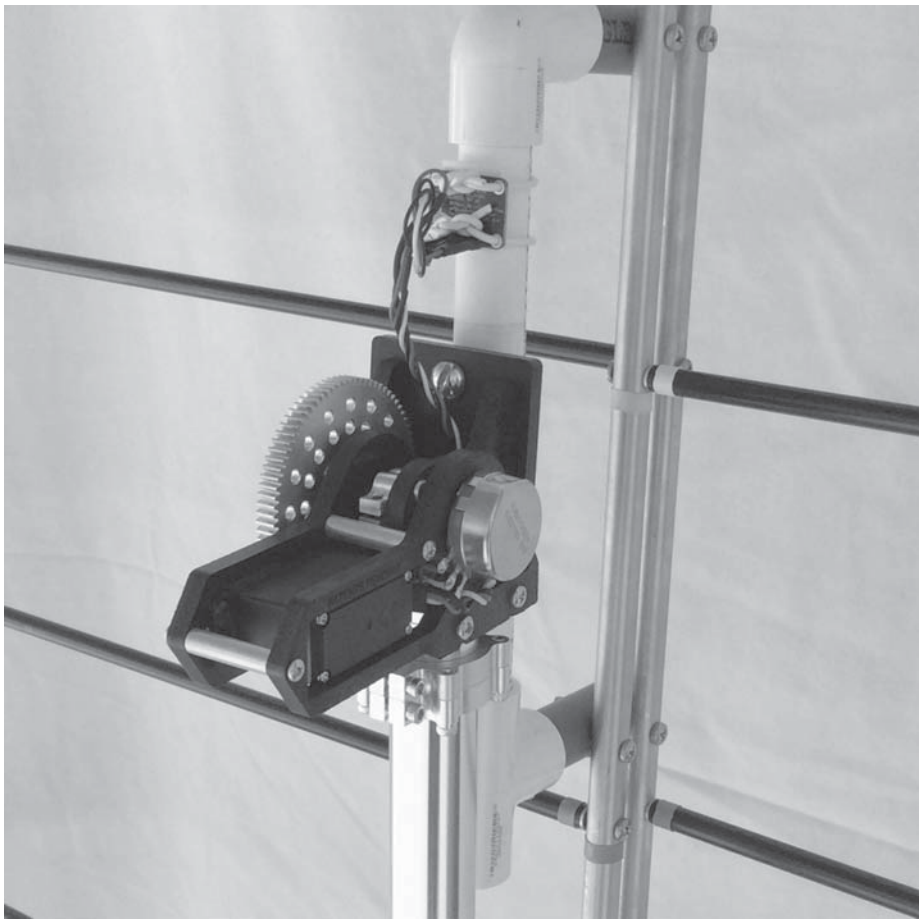

Figure 5 — The elevation gimbal shown with antenna attached.

Installation

In a nut shell, assemble the electronics and the gimbal. Attach them to your support then attach your antenna and the Bosch sensor. Attach your antenna to the tilt platform so it points straight up when the tilt platform is run all the way over on its side such that the plane of the tilt platform is also vertical. I attached my Elk LPDA antenna using two U-bolts after drilling four holes in the tilt plate. Position your antenna of choice on the tilt plate so the antenna is roughly balanced to help reduce the load on the tilt servo. There's plenty of torque so it should be fine to add a rear counter-weight to the boom if it allows you to balance the antenna better. Be aware that when the target is near zenith, the antenna will extend below the level of the gimbal. If you are using a tripod, add a vertical extension, otherwise when the antenna is pointed near zenith it will hit the tripod legs.

Attach the Bosch sensor breakout board such that:

– (1) the short dimension is parallel to the antenna boom,

– (2) the populated side of the board faces upwards and

– (3) the side with the control signals (SDA, SCL etc.) points in the rear direction of the antenna pattern.

Take some care to make this accurate and secure because the overall pointing accuracy is entirely dependent on how parallel the sensor is to the antenna bore site. The position along the boom does not matter, but since one of the sensors is measuring magnetic fields, mount it as far as possible from anything containing iron such as screws or U-bolts. It is not effected nearly as much by aluminum, but I would still stay at least an inch away from aluminum as well.

Power up the Tracker controller. Either connect with Wi-Fi or attach a CAT5 cable to the wired Ethernet controller. The default IP address is 192.168.0.122. If your computer is on the same network you can surf to that address and immediately see the main web page. If you want to change the IP of the Tracker, you have two choices. One choice is to edit the source code file *Webpage.cpp* (on the *QEXfiles* web page) and load a new image into the Ardunio. The other choice is to temporarily change your computer network to 192.168.0.0 so you can surf as above, then use the Tracker web page itself to

set a different IP address, reboot the Arduino then change your computer network back to your desired setting.

Once your web page is accessible, use the Gimbal section at the bottom to experiment with the motion range of each axis. There is no predefined assignment of which servo axis is azimuth or elevation. When setting the minimum and maximum for the elevation servo, make sure to consider the full range of azimuth. The minimum and maximum values are stored in EEPROM so they will retain their values through a power cycle.

Web Page Description

Turn on the Tracker controller and surf to its network address with your browser. You should see the web page shown in Figure 6. The page has two parts. The top part allows setting and inspecting the Two-Line Elements (TLEs) used to define the motion of the satellite of interest. The bottom part is a table showing detailed information for each of the Tracker subsystems of Target, GPS, Sensor and Gimbal. Look through the table carefully because it provides a lot of information and control capability. Most fields are self explanatory.

You will note that some of the data fields can be overwritten. This effectively turns off the automatic setting and allows you to enter your own values. Suggestions for how these can be used will be mentioned below.

Web Page in Detail

Across the very top is the title. Hovering over this title for a moment will display the software version. To the left is the network IP address of the Tracker. If this value is edited and Set, a new value will be stored in EEPROM and will be used the next time the Tracker is powered up or rebooted. To the right is a button to Reboot Arduino, mainly for this purpose. Below the title is the message line. Look here for confirmations, additional information and general messages as you use the page.

Aside from this bit of housekeeping, the top portion of the page mainly allows you to enter and Upload the TLE (two-line elements) for the satellite you wish to track. There are two text areas for showing TLEs. The top-most text area, with the darker background, is read-only and displays the TLE currently loaded into the Tracker, if any. The text area just beneath, with the white background, is writable. Here you can either copy/paste a TLE directly or you can type in the name of a satellite in the field provided and select a file that contains its TLE. The Tracker will scan through the entire file for a name match. The name is not case sensitive. The Tracker expects the file format to have the name on the line just before the TLE in typical fashion. If the satellite is found with a valid TLE, it will appear in the white text area. At this point the TLE is still just in your browser. To actually send it to the Tracker, click Upload. After successfully uploading a valid TLE, it will appear in the darker text area. This is the TLE that the Tracker will follow. You can change, or erase the writeable text area all you want and it won't matter unless you Upload it again.

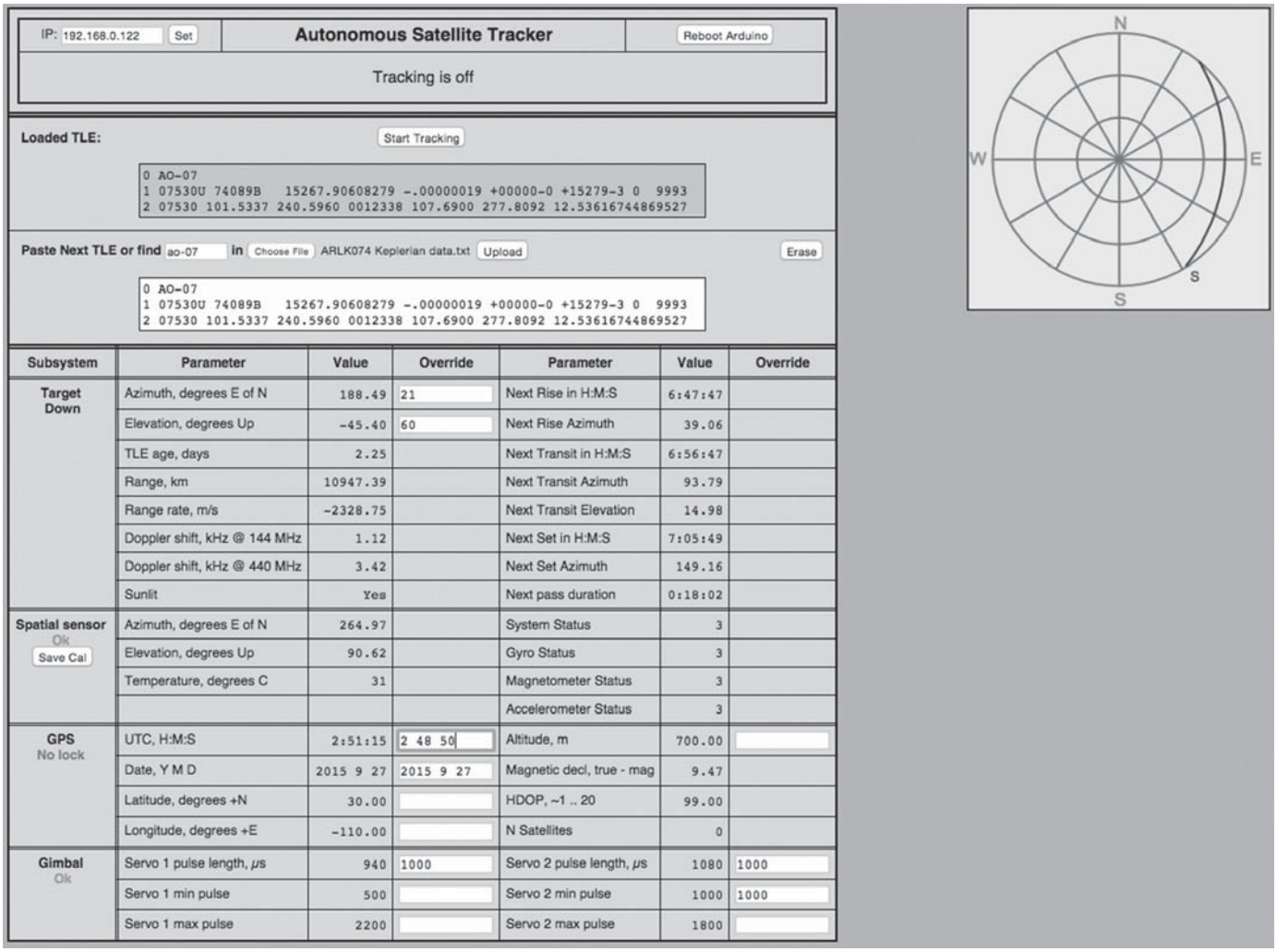

Subsystem	Parameter	Value	Override	Parameter	Value	Override
Target Down	Azimuth, degrees E of N	188.49	21	Next Rise in H:M:S	6:47:47	
	Elevation, degrees Up	-45.40	60	Next Rise Azimuth	39.06	
	TLE age, days	2.25		Next Transit in H:M:S	6:56:47	
	Range, km	10947.39		Next Transit Azimuth	93.79	
	Range rate, m/s	-2328.75		Next Transit Elevation	14.98	
	Doppler shift, kHz @ 144 MHz	1.12		Next Set in H:M:S	7:05:49	
	Doppler shift, kHz @ 440 MHz	3.42		Next Set Azimuth	149.16	
	Sunlit	Yes		Next pass duration	0:18:02	
Spatial sensor Ok Save Cal	Azimuth, degrees E of N	264.97		System Status	3	
	Elevation, degrees Up	90.62		Gyro Status	3	
	Temperature, degrees C	31		Magnetometer Status	3	
				Accelerometer Status	3	
GPS No lock	UTC, H:M:S	2:51:15	2 48 50	Altitude, m	700.00	
	Date, Y M D	2015 9 27	2015 9 27	Magnetic decl, true - mag	9.47	
	Latitude, degrees +N	30.00		HDOP, ~1 .. 20	99.00	
	Longitude, degrees +E	-110.00		N Satellites	0	
Gimbal Ok	Servo 1 pulse length, µs	940	1000	Servo 2 pulse length, µs	1080	1000
	Servo 1 min pulse	500		Servo 2 min pulse	1000	1000
	Servo 1 max pulse	2200		Servo 2 max pulse	1800	

Figure 6 — The Autonomous Satellite Tracker web interface. Note the satellite track projection in the inset on the upper right.

Monitor and Control

Below the TLE section is the main table for monitor and control. The first table section is for the Target to be tracked. In the left column you will see observing details of the uploaded satellite elements at the time and location shown in the GPS section farther down. In the right column you will see information about the next pass. Note that the Tracker never computes information in the past, so if a pass is already underway (the satellite is currently above the horizon) then the Next Rise information will be for the subsequent complete pass, since that event has already occurred for a pass that is underway. You can override the computed azimuth and elevation. If tracking is enabled, this allows you to point your antenna at any desired fixed sky location.

Beside the table (or below if your screen is narrow) is an all-sky graph that shows the pass as it will look overhead. Again, if you override the time, and jump into the middle of a pass in progress, only the path from that moment onward will be drawn.

The Spatial Sensor

Below the Target Down section of the table is the section for the Spatial sensor. This displays the azimuth and elevation that it is measuring and reporting to the Tracker. It also displays the current temperature and the status of the system processor and each of the individual sensors. These individual status values can range from 0 through 3, where 3 is the best. The Tracker will not use the data unless all system status values report at least 1. Procedures for calibrating each sensor are provided in the Bosch manual.[11] The sensor package will need to be moved around to different orientations to get all sensors at their best values. Use the pulse length override fields in the Gimbal section (see below) to perform these motions. Once all sensors report state 3, their associated internal calibration data can be stored to EEPROM by clicking the Save Cal button. Once saved, these values will be restored each time the Tracker is powered up, and all sensors will usually immediately come up in state value 3. This button is available only when all sensors report status 3. The magnetic sensor is very sensitive to local magnetic fields and iron objects, so if you relocate the Tracker, I recommend that you perform the calibration again and store a new set of values.

GPS

The GPS section shows the reported time and location, and also displays some quality metrics. HDOP is the Horizontal Dilution of Precision.[12] This is an indication of the accuracy of the latitude and longitude, the position values most important to the Tracker. HDOP values range from less than 1, which indicates ideal conditions, up to 20 or more, indicating that location can be incorrect by 300 m or more. The number of satellites used in the fix is reported, where four or more is desirable. If you don't have a GPS connected, or it does not have lock, or you just want to experiment, you can override the time, date, latitude, longitude and altitude to see the effect on the passes. You don't need a GPS at all if you enter these data carefully.

Gimbal

At the bottom of the table is the Gimbal section. These data are in units of raw pulse duration. If you are aware of how hobby servo motors function, you will recall they are commanded to a given rotation angle determined by the length of a pulse issued on their control line. Pulse durations vary by manufacturer and even among devices of the same model. Roughly speaking, pulse lengths range from about 500 µs for one position extreme up to around 2400 µs for the other extreme. Normally pulse durations are set by the tracking algorithm, and bounded by the indicated minimum and maximum limit values. You can directly set specific pulse durations for each motor if you wish. Doing so will automatically disable tracking if it is enabled. This is fun, but also important to determine the safe as-built motion limits of each axis. The limits are stored in EEPROM and used by the Tracker to avoid exceeding the limits of each servo motor.

The Gimbal section also allows you to tune each axis for best tracking performance. Recall from the tracking algorithm that a motor is moved a small amount, stops to allow a stable sensor reading, then moves again repeatedly to track the target. Fields are provided for you to set the stop period and the step size for each move. The stop period should be set to just long enough for the entire gimbal and antenna to stop shaking after a move. The step size should be set to the smallest value that results in a reliable change in reported sensor position.

Operation

After everything is set up and you are comfortable with the safe operation of the Tracker motions, you are ready to track a satellite. Set the system up in a location with a good view of the sky. Turn it on, load the TLE into the white text area and click Upload. Click Start Tracking to begin tracking the satellite. My web page for this project is **www.clearskyinstitute.com/ham/AST/**. That's all there is to it. Enjoy.

All photos courtesy of the author.

Elwood Downey, WBØOEW, has held the same call sign since he was first licensed in 1974. He is an ARRL Member. Elwood enjoys software, digital modes, antennas, and experimenting. He graduated with a BSEE cum laude in 1977 from Purdue University. Since then he has focused his career on telescope control systems and related astronomical instrumentation, which he finds very fulfilling. His career has taken him to many of the great observatories around the world.

Notes

[1]**siarchives.si.edu/collections/siris_sic_8335**.
[2]**https://en.wikipedia.org/wiki/Microelectromechanical_systems**.
[3]**https://www.ngdc.noaa.gov/geomag/WMM/DoDWMM.shtml**.
[4]**https://en.wikipedia.org/wiki/Gradient_descent**.
[5]**https://en.wikipedia.org/wiki/Gimbal_lock**.
[6]**https://en.wikipedia.org/wiki/Euler_angles**.
[7]**https://github.com/brainwagon/angst**.
[8]**www.amsat.org/amsat/articles/g3ruh/111.html**.
[9]**www.arrl.org/QEXfiles**.
[10]**www.xephem.com**.
[11]**https://www.bosch-sensortec.com/en/homepage/products_3/9_axis_sensors_5/ecompass_2/bno055_3/bno055_4**.
[12]**https://en.wikipedia.org/wiki/Dilution_of_precision_(GPS)Figure Captions**.

Al Christman, K3LC

Grove City College, 100 Campus Drive, Grove City, PA 16127-2104

Compact Top-Band Vertical Yagis

The performance of a quarter-wave radiator improves with the addition of parasitic elements to form a vertically-polarized Yagi array that is entirely within the same foot print as the radiator. This study quantifies the improvement.

Probably the most widely used transmit antenna on the 160-meter band is a vertical monopole fed against an extensive system of radials. This article was written to illustrate how the performance of an existing quarter-wave radiator is improved when parasitic elements are added to create a vertically-polarized Yagi antenna. One or more sloping wires can be suspended from the apex of the vertical radiator to create either two- or three-element arrays. Compact designs are presented, in which the ground screens of the parasitic elements fit entirely within the foot-print of the original antenna. The designs are compared with a conventional four-square phased array.

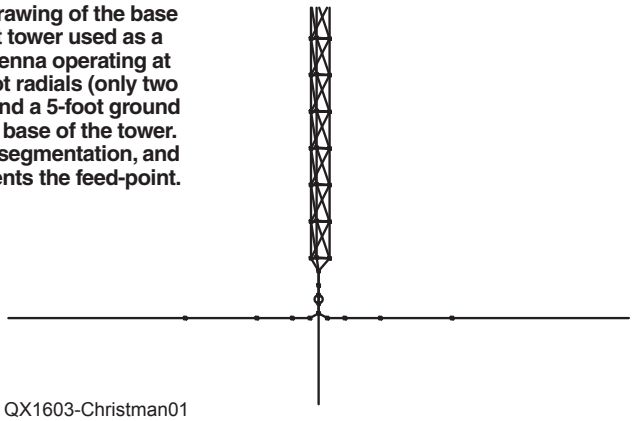

Figure 1 — Close-up drawing of the base region of the 130-foot tower used as a vertical monopole antenna operating at 1830 kHz. Sixty 130-foot radials (only two are shown for clarity) and a 5-foot ground rod are installed at the base of the tower. The dots indicate wire segmentation, and the small circle represents the feed-point.

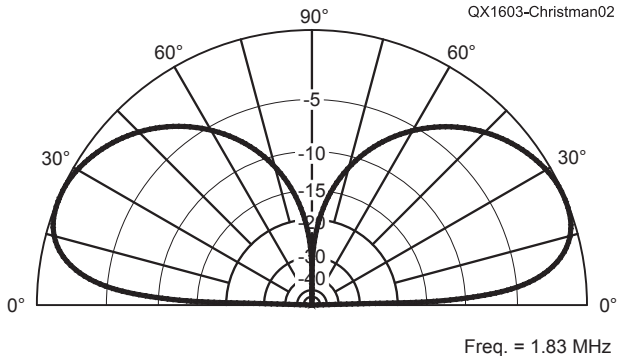

Figure 2 — Elevation-plane radiation pattern at 1830 kHz for the reference antenna (130-foot tower with a ground-screen of sixty 130-foot buried radials). The peak gain is 1.12 dBi at 22.7 degrees take-off angle.

Computer Simulations

In practice, a top-band vertical monopole would probably be constructed from either zinc-clad steel or aluminum, and the radials would likely be made from aluminum or copper wire. Therefore, the decision was made to employ aluminum for all of the metallic conductors in the computer models. The radials are #14 AWG wire buried at depths ranging from 1.5 to 6 inches. The soil was assumed to be average, with a conductivity of 0.005 S/m and a dielectric constant of 13. Each design was simulated with the Roy Lewallen, W7EL, *EZNEC* software package.[1]

A single 130-foot tower, similar to Rohn 25, was used as the reference antenna for this study. Figure 1 is a close-up drawing of the base region of the tower, showing the feed point, a five-foot ground rod, and a pair of buried radials at the base of the monopole. The complete model has sixty 130-foot radials in the ground screen, with the radials buried to a depth of three inches.

Figure 2 displays the principal elevation-plane radiation pattern for this antenna. The peak gain is 1.12 dBi at a take-off angle of 22.7 deg above the horizon, when the frequency is 1830 kHz. The input impedance at that frequency is 41.26 + *j*19.21 Ω. The tower is self-resonant at 1760 kHz.

[1]Notes appear on page 15.

Table 1.

Input SWR (50 Ω reference) for a 130-foot tower operating in the 160-meter band with two feed point configurations. The ground screen is sixty 130-foot radials buried 3 inches deep.

Frequency (kHz)	*No matching network*	*4527 pF series capacitance*
1800	1.42:1	1.36:1
1830	1.58:1	1.21:1
1860	1.81:1	1.26:1

Table 1 lists the SWR data for the antenna (using a 50 Ω reference) if there is no impedance matching employed, and also for the case where a series capacitance (4527 pF) is inserted at the base of the tower to cancel the input reactance at 1830 kHz. In either situation, the SWR is well below 2:1 from 1800 to 1860 kHz.

Two-element Yagi with Reflector

If the entire array is to fit within the confines of the ground-screen of the existing tower, then a design such as that shown in Figure 3 can be constructed. The parasitic element is a sloping reflector (#10 AWG wire) with length and distance from the monopole adjusted in order to maximize the gain of the antenna. Figure 4 illustrates the configuration of the reflector that includes a short (1.5-foot) vertical section, topped by a long sloping wire whose upper end is anchored (via an insulating rope) to the apex of the 130-foot tower. For best performance at 1830 kHz, the length of the sloping portion of the reflector turned out to be 128.5 feet (total reflector length is 130 feet), while the spacing between the base of the reflector and the tower is 72 feet.

Because of the location of the reflector, the radials in its ground-screen can be no longer than 58 feet, so 120 of them were installed at a depth of 1.5 inches. Recall that the radials in the ground-screen of the tower are buried 3 inches deep. In order to keep *EZNEC* from crashing (this would occur if one or more radials touched each other), we will place each set of radials at a slightly different burial depth. The base of the reflector must be connected directly to its ground screen in order to be operational. If the reflector is open-circuited at the base, then it electrically disappears from the circuit, and the antenna will function as a single-tower non-directional radiator.

When the reflector is active, the maximum forward gain of the resulting 2-element Yagi antenna is 4.28 dBi at a take-off angle of 24.3 degrees, at 1830 kHz. This is an improvement of 3.16 dB compared to the gain of the tower by itself. A plot of the elevation-plane radiation pattern of the array is shown in Figure 5. Notice that there is no distinct rear lobe, but the azimuth-plane radiation pattern seen in Figure 6 reveals a front-to-back ratio of 14.93 dB at the elevation angle where peak gain occurs. The half-power beamwidth is 131.7 degrees and the input impedance is 24.11 + *j*72.76 Ω. At 45 degrees to either side of the peak of the main lobe, the gain falls to 2.96 dBi, which is 1.32 dB less than the maximum value.

If we add a series capacitance of 1195 pF at the feed-point of the tower, then the input reactance can be cancelled, leaving a resistive impedance of about 24 Ω. This can be converted to 50 Ω using an "un-un" transformer. Under these conditions, the resulting 2:1 SWR bandwidth of the array extends from about 1816 to 1853 kHz (37 kHz), using 24.1 Ω as the reference impedance.

Two-element Yagi with Director

Although the parasitic element described above works well as a reflector, it can also be converted into a director, enabling it to perform double duty. This is accomplished by inserting a 2050 pF capacitance in series with the base of the reflector wire, at the point where it connects to the radial ground-screen. In this configuration, the peak forward gain at 1830 kHz is 3.37 dBi at a take-off angle of 23.1 degrees. This is an improvement of 2.25 dB compared to the gain of the tower by itself, but is 0.91 dB less than what can be obtained when the parasitic element serves as a reflector. Figure 7 displays the elevation-plane radiation patterns for the 2-element Yagi in both director mode (dashed line) and reflector mode (solid line). There is a distinct rear lobe when the array is operating in director mode, but the front-to-back ratio is very low (just 3.18 dB). Both of the corresponding azimuth-plane radiation patterns are shown in Figure 8. The half-power beamwidth is 140.5 degrees and the input impedance is 14.57 + *j*35.98 Ω for director-mode operation.

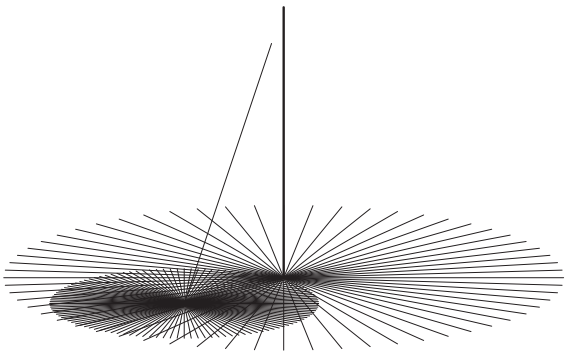

QX1603-Christman03

Figure 3 — A compact 2-element Yagi antenna, based upon the reference tower with a ground-screen of sixty 130-foot radials buried 3 inches deep. The parasitic element is a sloping wire reflector connected to a ground-screen of 120 radials that are 58 feet long buried 1.5 inches deep. The ground-screen of the reflector does not extend beyond the perimeter of the original antenna system.

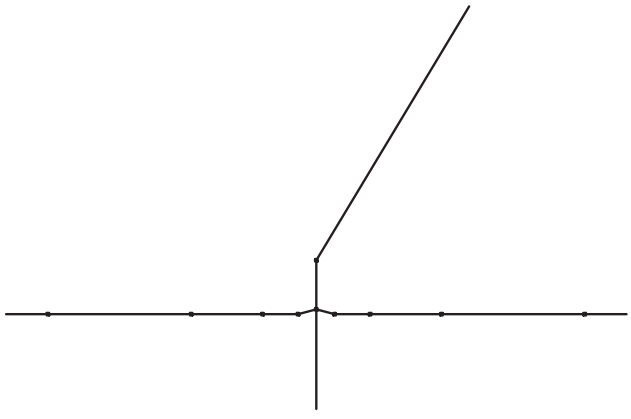

QX1603-Christman04

Figure 4 — Close-up view of the base region of the parasitic reflector from Figure 3. Just two radials are shown for clarity, along with a 3-foot ground rod. The parasitic element is a short (1.5-foot long) vertical section near the base, and a much-longer (128.5 feet for the 2-element Yagi) sloping section. The dots indicate wire segmentation.

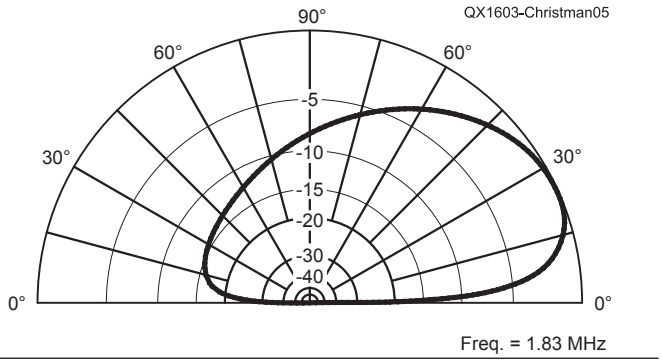

Figure 5 — Elevation-plane radiation pattern at 1830 kHz for the 2-element Yagi antenna of Figure 3. Peak gain is 4.28 dBi at 24.3 degrees take-off angle. There is no distinct rear lobe, but the front-to-back ratio is 14.93 dB at the elevation angle where maximum gain occurs.

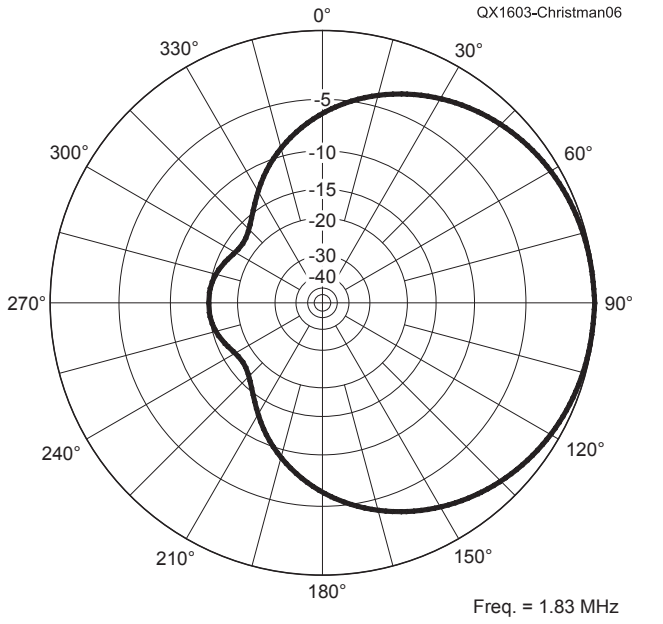

Figure 6 — Azimuth-plane radiation pattern at 1830 kHz for the 2-element Yagi of Figure 3. The front-to-back ratio is 14.93 dB at 24.3 degrees take-off angle, and the half-power beamwidth is 131.7 degrees at the same elevation angle.

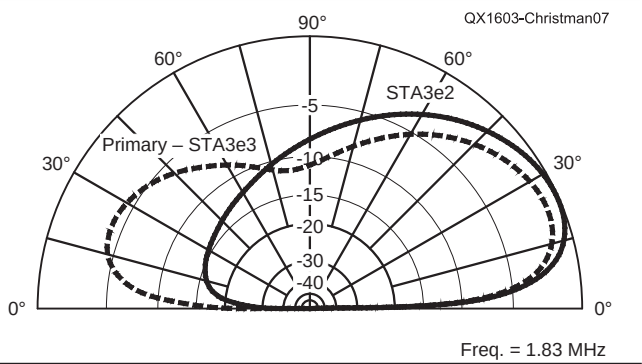

Figure 7 — Elevation-plane radiation patterns at 1830 kHz for the two-element Yagi operating in director (dashed line) or reflector (solid line) mode. The director-mode pattern has been reversed, so that both main lobes are pointing toward the right. The director mode gain is 3.37 dBi at 23.1 degrees take-off angle with a front-to-back ratio of 3.18 dB. The reflector mode peak gain is 4.28 dBi at 24.3 degrees take-off angle with a front-to-back ratio of 14.93 dB at the same elevation angle as the peak gain.

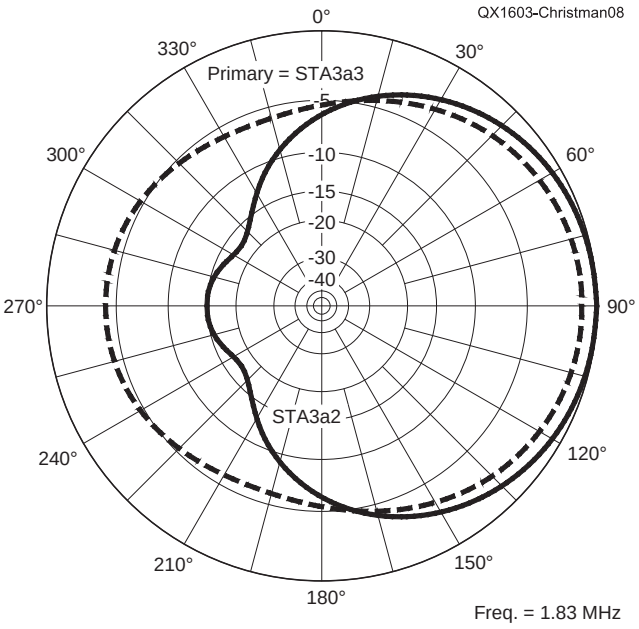

Figure 8 — Azimuth-plane radiation patterns at 1830 kHz for the two-element Yagi antenna operating in either director (dashed line) or reflector (solid line) mode. Director mode peak gain is 3.37 dBi at 23.1 degrees take-off angle with a front-to-back ratio of 3.18 dB, and half-power beamwidth of 140.5 degrees. Reflector mode peak gain is 4.28 dBi at 24.3 degrees take-off angle with a front-to-back ratio of 14.93 dB, and half-power beamwidth is 131.7 degrees. The director-mode pattern has been reversed, so that both main lobes are pointing toward the right.

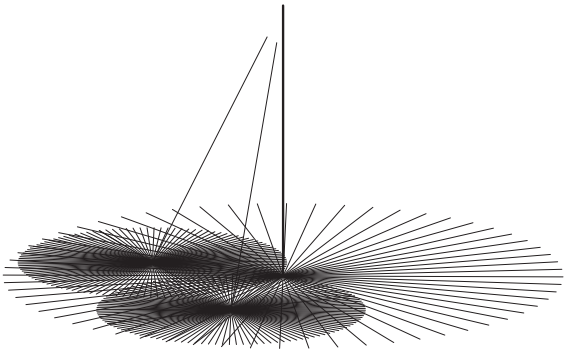

QX1603-Christman09

Figure 9 — Two parasitic elements are installed at right angles to one another. The central tower functions as an omni-directional antenna when both of these parasitic elements are open-circuited at their bases. Alternatively, either element can function as either a reflector or director, yeilding four different 2-element Yagi configurations with patterns 90 degrees apart from one another.

The input reactance of the director-mode Yagi may be eliminated by adding a 2417 pF capacitance in series with the feed-point. Then, using a reference impedance of 14.6 Ω, the resulting 2:1 SWR bandwidth extends over about 40 kHz (1807 – 1847 kHz).

Figure 9 depicts two identical multi-mode (reflector / director / open-circuit) parasitic elements installed at right angles to each other. An antenna like this could cover all four of the cardinal points of the compass, although its performance would be better in some quadrants than in others. The next logical step in the design process is to modify the array by utilizing both a reflector and a director at the same time.

Three-element Yagi

If we place one parasitic element directly opposite a second one, with the tower situated midway between them, we can create a reversible 3-element beam (see Figure 10). Each parasitic element can function either as a reflector (by short-circuiting its base to the ground-screen) or as a director (by inserting a series capacitor between the bottom of the wire and the ground-screen). Alternatively, we may also remove an element from the antenna system (rendering it electrically invisible) by open-circuiting that wire at its base. Since the radials used in conjunction with the two parasitic elements are not full-size, the reflector ground-screen does not overlap that of the director. As a result, all of these shortened radials can safely be placed at the same burial depth (1.5 inches) in our *EZNEC* model.

Computer analysis reveals that the 3-element version of the array works best when the sloping portion of each parasitic wire element is shortened from 128.5 to 128.0 feet, reducing the overall wire length to 129.5 feet. Setting the base capacitance of the director to 2050 pF will yield a peak forward gain of 5.25 dBi at a take-off angle of 23.6 degrees as seen in Figure 11. The input impedance at 1830 kHz is 14.17 + *j*47.26 Ω.

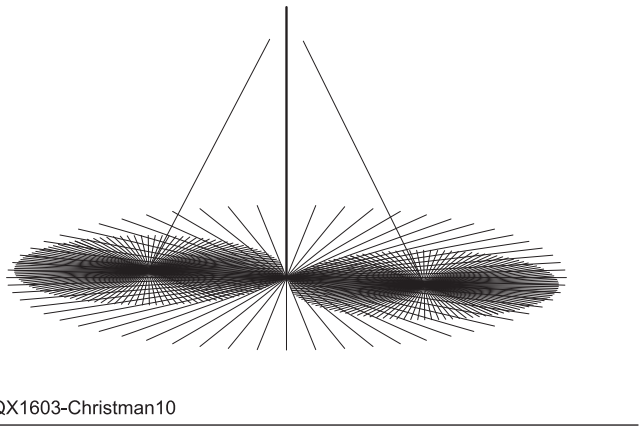

Figure 10 — The central tower is augmented by two parasitic elements positioned on opposite sides of the vertical monopole. A 3-element Yagi is created when one of the sloping-wire elements functions as a reflector while the other serves as a director. By reversing the roles of the two parasitic elements, the pattern direction can be switched by 180 degrees.

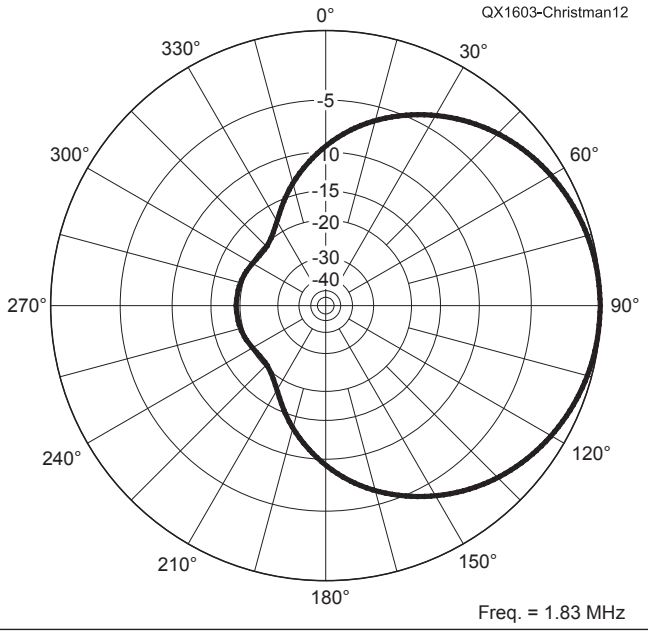

Figure 12 — Azimuth-plane radiation pattern at 1830 kHz for the 3-element Yagi of Figure 10. The peak gain is 5.25 dBi at a take-off angle of 23.6 degrees, with a front-to-back ratio of 19.23 dB, and the half-power beamwidth is 108.5 degrees. The gain at 45 degrees to either side of bore-sight is 3.23 dBi.

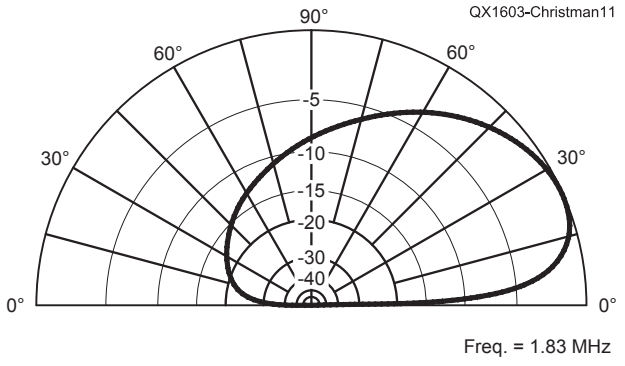

Figure 11 — Elevation-plane radiation pattern at 1830 kHz for the 3-element Yagi of Figure 10. The peak gain is 5.25 dBi at a take-off angle of 23.6 degrees, and the input impedance is 14.17 + *j*47.26 Ω. The front-to-back ratio is 19.23 dB at the elevation angle of maximum gain.

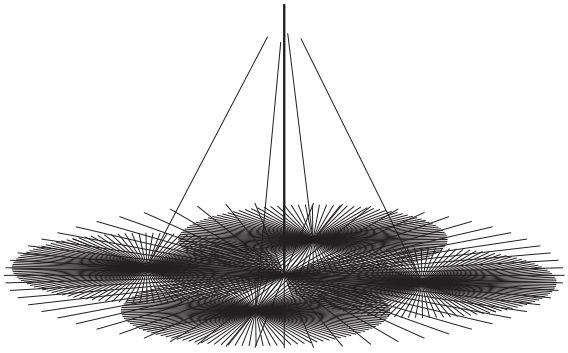

Figure 13 — When the central tower is supplemented by four parasitic elements positioned at 90 degree intervals around the monopole, two reversible 3-element Yagis can be implemented that cover any one of the four compass quadrants with equal performance.

Table 2.

Performance data for the compact 3-element Yagi antenna. The director uses a base-loading capacitance of 2050 pF with 1840 pF capacitance in series with the feed-point. The 2:1 SWR (14.2 Ω reference) bandwidth is 51 kHz.

Parameter at frequency	1806 kHz	1830 kHz	1857 kHz
Peak Gain and take-off angle(dBi and deg)	4.84 at 23.6	5.25 at 23.6	5.19 at 23.4
Front-to-Back Ratio (dB)	8.13	19.23	11.08
Half-power beamwidth in azimuth plane, (deg)	105.9	108.5	105.4
Input Impedance (Ω)	10.04 - *j*7.23	14.17 + *j*0.0	10.93 + *j*7.83
SWR (14.2 Ω reference)	1.98:1	1.0:1	1.95:1

Table 3.

Performance data for the compact 3-element Yagi. The director uses a base-loading capacitance of 2600 pF with 1843 pF capacitance in series with the feed-point. The 2:1 SWR bandwidth (10.2 Ω reference) is about 37 kHz.

Parameter at frequency	1809 kHz	1830 kHz	1846 kHz
Peak Gain and Take-off Angle (dBi and deg)	5.19 at 23.5	5.44 at 23.4	5.37 at 23.2
Front-to-Back Ratio (dB)	10.75	21.26	12.98
Half-power Beamwidth in Azimuth plane, (deg)	105.1	105.2	102.0
Input Impedance (Ω)	9.08 - j6.71	10.23 + j0.0	8.28 + j6.13
SWR (10.2 Ω reference)	2.0:1	1.0:1	1.98:1

There is no distinct rear lobe in the elevation-plane radiation pattern, but the F/B ratio is 19.23 dB at the elevation angle where maximum gain occurs (see Figure 12). In the azimuth plane, the half-power beamwidth is 108.5 degrees. The gain at 45 degrees to either side of bore sight is 3.23 dBi, or 2.02 dB below the peak of the main lobe.

The input impedance of this Yagi can be made completely real by adding a 1840 pF capacitance in series with the feed-point. Then, using a reference impedance of 14.2 Ω, the resulting 2:1 SWR bandwidth is about 51 kHz (1806 – 1857 kHz). Table 2 provides all of the important performance data for this array.

The gain of this Yagi antenna may be increased somewhat, by making the base-loading capacitance of the director even larger. However, this reduces the input resistance as well as the 2:1 SWR bandwidth. I decided to see how much gain I could get, with the stipulation that the resistance at the feed-point had to be at least 10 Ω at 1830 kHz. Utilizing a capacitance of 2600 pF (rather than 2050 pF), the peak forward gain rises to 5.44 dBi at a take-off angle of 23.4 degrees. However, the input impedance at 1830 kHz now falls to 10.23 + *j*47.20 Ω. As usual, there is no distinct rear lobe in the elevation-plane radiation pattern, but the F/B ratio is now 21.26 dB at the elevation angle where maximum gain occurs. In the azimuth plane, the half-power beamwidth shrinks slightly to 105.2 degrees. The gain at 45 degrees to either side of bore-sight is 3.28 dBi, or 2.16 dB below the peak of the main beam.

The reactance at the feed point of the Yagi antenna can be cancelled by adding a 1843 pF capacitance in series with the input terminals. Then, using a reference impedance of 10.2 Ω, the resulting 2:1 SWR bandwidth is about 37 kHz (1809 – 1846 kHz). I listed the details in Table 3.

If coverage of all compass directions is desired, then an array with four multi-mode parasitic elements can be built, as illustrated in Figure 13. Two of the parasitic wires would be active at any given time for Yagi functionality, but all four could be simultaneously open-circuited at their bases to achieve omni-directional radiation. Figure 14 overlays the azimuth patterns for all four of the of the compass directions.

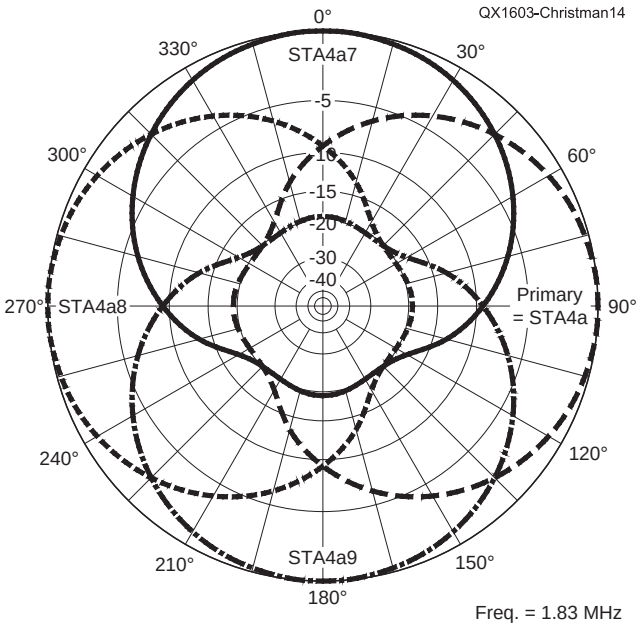

Figure 14 — Azimuth-plane radiation patterns for the antenna system of Figure 13.

Comparison with a 4-Square

A conventional four-square phased array is pictured in Figure 15. This is a full size antenna with quarter-wave vertical elements, each incorporating a ground-screen composed of sixty 130-foot radials that are buried at depths of either 1.5, 3.0, 4.5, or 6.0 inches. At 1830 kHz, the peak forward gain is 6.56 dBi at a 21.5 degree take-off angle, and the front-to-back ratio is 18.08 dB.

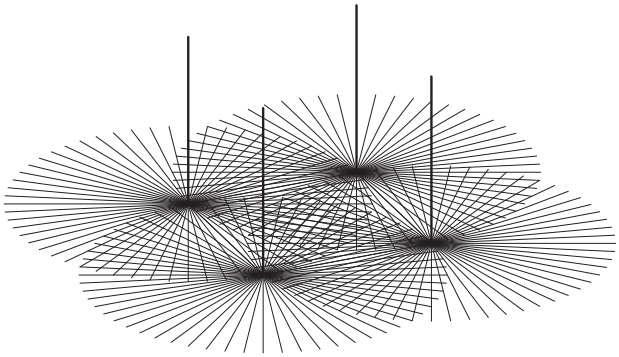

QX1603-Christman15

Figure 15 — Classic four-square phased-vertical array with 0.25 λ spacing and progressive 90 degree current phasing. Each element is 0.25 λ tall with a ground system of sixty 130-foot radials.

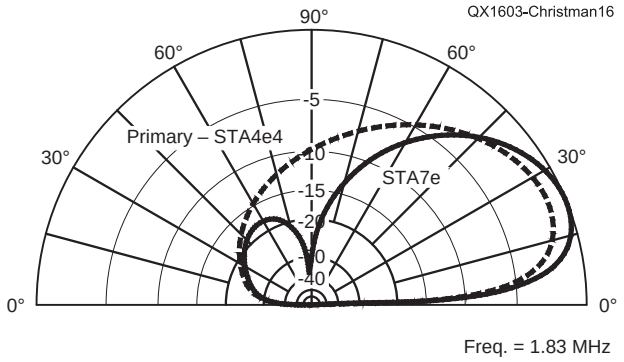

Figure 16 — Elevation-plane radiation patterns at 1830 kHz for the 4-square array of Figure 15, along with the "max-gain" version of the 3-element vertical Yagi antenna of Figure 13. The 3-element Yagi antenna pattern (Primary trace) peak gain is 5.44 dBi at 23.4 degrees take-off angle with a front-to-back ratio of 21.26 dB. The 4-square array (STA7e trace) peak gain is 6.56 dBi at 21.5 degrees take-off angle with a front-to-back ratio of 18.08 dB.

The elevation-plane radiation patterns of this four-square array (trace *STA7e*), along with the max-gain version of our three-element Yagi (peak gain of 5.44 dBi, trace *Primary – STA4e4*), are shown for comparison in Figure 16. The performance of the Yagi is clearly inferior to that of the phased array, but the parasitic antenna is much smaller in size, and should be less expensive to build. Table 4 provides information about the relative merits of both systems.

Table 4.

Performance comparison between a classic 4-square phased array and the "max-gain" version of the compact 3-element vertical Yagi antenna.

Parameter	*4-square*	*Yagi antenna*
Peak gain and take-off angle (dBi and deg)	6.56 at 21.5	5.44 at 23.4
Front-to-back ratio (dB)	18.08	21.26
Half-power beamwidth in azimuth plane (deg)	100.1	105.2
Gain at 5 deg take-off angle (dBi)	2.11	0.78
Gain at 10 deg take-off angle (dBi)	5.15	3.84
Gain at 15 deg take-off angle (dBi)	6.21	4.96
Gain at 20 deg take-off angle (dBi)	6.55	5.37
Gain at 25 deg take-off angle (dBi)	6.49	5.42
Gain at 30 deg take-off angle (dBi)	6.15	5.25
Gain at 35 deg take-off angle (dBi)	5.60	4.91
Gain at 40 deg take-off angle (dBi)	4.85	4.44
Gain at 45 deg take-off angle (dBi)	3.91	3.87

Conclusions

This article describes the performance of a variety of vertically polarized Yagi antennas for operation on the 160 m band. The driven element is a base-insulated quarter-wave tower augmented by a ground screen made up of sixty 130-foot radials. The parasitic elements are sloping wires, with their bases anchored some distance from the bottom of the tower, while their tops are attached via insulating ropes to the apex of the radiator. Each parasitic element has its own separate ground-screen, and can serve as either a reflector or director. Elements may also be electrically removed from the circuit. The ground screens of the parasitic elements are limited in size, and do not extend beyond the boundaries of the tower ground radial system. The maximum gain of the 3-element compact Yagi antenna falls about 1.1 dB below that of a classic four-square phased array, but requires less than half as much land area, and is also easier to feed. Finally, the designs shown here can easily be modified for use on other bands.

Al Christman was first licensed in 1974 as WA3WZD. He received his Doctorate in Electrical and Computer Engineering from Ohio State University and is Professor of Electrical Engineering at Grove City College in Western Pennsylvania. When not modeling antennas by computer for fun, Al chases SSB DX on 20 meters, or enjoys riding his motorcycle.

Notes

[1] *EZNEC* antenna-simulation software is available from Roy Lewallen, W7EL, P. O. Box 6658, Beaverton, OR 97007.

Robert J. Zavrel, Jr., W7SX

PO Box 91, Elmira, OR 97437; **w7sx@arrl.net**

Elevation and Pseudo-Brewster Angle Formation of Ground-Mounted Vertical Antennas

The formation of the elevation pattern of ground mounted vertical antennas is the result of two basic mechanisms. The first is a very slow lowering of the main pattern lobe over hundreds of wavelengths, and the second is ground attenuation due to dielectric losses that result from the very low center of radiation of the vertical antenna.

The purpose of this article is to investigate the mechanisms for the formation of the radiated elevation angle in ground-mounted vertical antennas. The commonly published explanation is that ground reflections reverse the phase, and thus wave cancellation occurs in the far field, and produce the pseudo-Brewster angle. The reflected cancellation wave is often made easier to visualize by referring to it as the antenna "image".

However, this explanation is not possible with ground-mounted vertical antennas ¼ wave or shorter in height. Simple geometry instructs us that this is not the case. The center of radiation from a ¼ wave or shorter ground mounted vertical antenna is at or very close to the ground. Therefore the point of ground reflection must be very close to the antenna, indeed within the radius of the radial system! Thus for the common theory to hold, the vertical antenna must have a reflection point on the antenna proper, and within the near field. Even if the near field could be considered the same as the far field for reflections, then a perfectly conducting radial system would not produce reflected waves that would cancel.

[1]Notes appear on page 20.

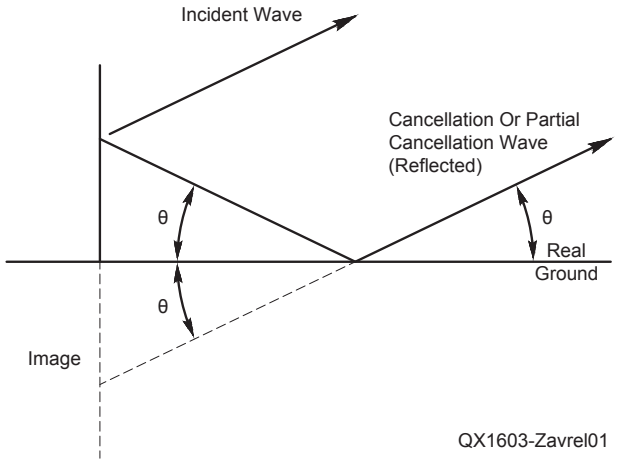

Figure 1 — The geometry for phase cancellation (or partial attenuation) from a ground-reflected interfering wave.

Vertical Antenna Over Ideal and Real Grounds

Figure 1 shows the basic principle of phase cancellation — or partial attenuation — from a reflected interfering wave. From electromagnetic theory and simple geometry the incident angle and the reflected angle θ ar*e always equal a*bove the reflector's surface. Figure 2 shows the sinusoidal current distribution along a ground-mounted quarter-wave vertical antenna. If we include the return ground current, the center of radiation is at the center of the antenna at ground level.

To complicate the matter farther, very close-in ground reflections, if they

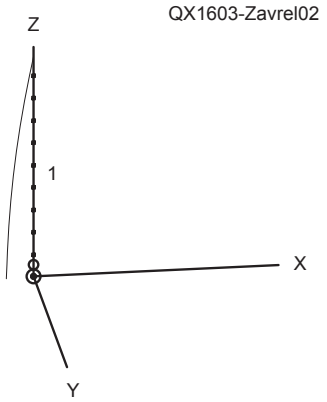

Figure 2 — The sinusoidal current distribution along a ground-mounted quarter-wave vertical antenna.

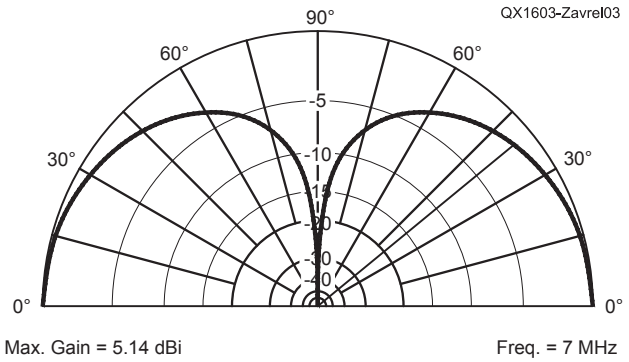

Figure 3 — Elevation pattern of a quarter-wave vertical antenna mounted over a perfectly conducting infinite ground plane.

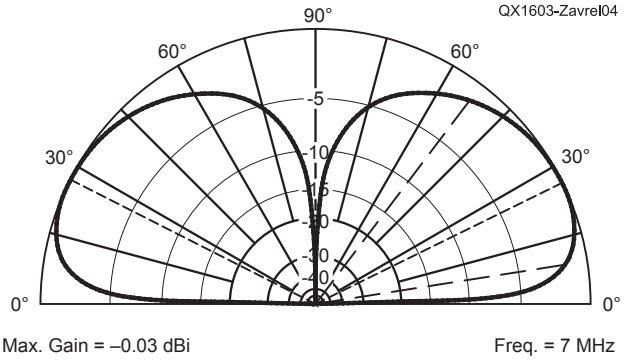

Figure 4 — Elevation pattern of a quarter-wave vertical antenna mounted over "average" ground. The pattern peak gain is at 26 degrees elevation.

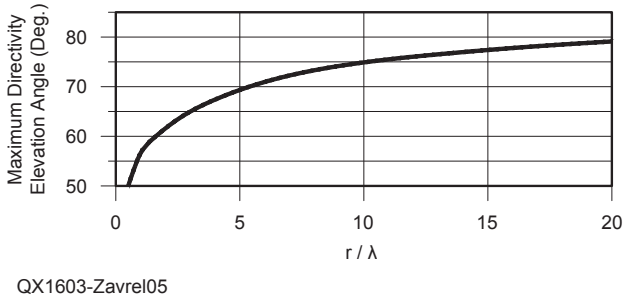

Figure 5 — The variation of the maximum directivity elevation angle (measured from the vertical) with respect to disc radius in wavelengths.

existed, would have to be determined by a rather complex integration, using antenna segmented amplitudes and phases. This is in contrast to a much simpler calculation of far-field reflections and cancellations that assume the antenna to be a point source.

If the conventional theory were true, we could lay out a more extensive radial system, say one-wavelength radials, and dramatically lower the angle of radiation and increase the overall gain, particularly at elevation angles whose associated reflection points fall on the new radial system no matter what the ground characteristics. This simply does not happen. There is very little effect upon the antenna directivity with even substantial increases in radial length. The increase in over-all gain occurs because of reduction of ground losses in the antenna *per se.*

The case for raised vertically polarized arrays — short wave broadcast curtains — is somewhat different. The elevation angle is affected by extensive ground screens and is used effectively to maximize patterns at lower elevation angles at many such facilities. This is achieved because the patterns of raised vertical antennas are affected by ground reflections as discussed later in relation to Figure 8.

Now, let us compare the elevation angle of a quarter-wave vertical antenna over a perfect ground with the same antenna over average ground. Figure 3 shows the well-known elevation pattern of a quarter-wave vertical antenna mounted over a perfectly conducting infinite ground plane. In this case we model a 7 MHz antenna. The scale is linear in decibels rather than the ARRL scale. Figure 4 shows the pattern of the same vertical antenna as in Figure 3, but over average ground. This is also quite familiar to many radio amateurs. Table 1 shows the gains of the two cases, in dBi, for elevation angles from 0 to 45 degrees.

The differences are quite striking. The gain at the "grazing angle", is maximum in Figure 3, but very heavily attenuated in Figure 4, indeed, indicating a complete null at this low angle. The grazing angle could be explained by phase cancellation since even a very low center of radiation could result in a reflection point well into the far field.

Of more interest to this discussion, the maximum gain response in Figure 4 (at 26 degrees elevation) is about 3 dB lower than at the same elevation angle in Figure 3. If this 3 dB attenuation were due to reflection cancellation (worst case ignoring the image), the reflection point would range between 0 and about 25 feet from the vertical antenna, on top of the radial field! Even at the relatively high angle of 45 degrees, we see almost 3 dB of attenuation. Furthermore, the feed-point impedances are identical, and

since the feed-point is at a current maximum on a single conductor radiator, the radiation resistances are also identical. Also, there is no ground loss in either configuration indicating that both antennas are nearly 100% efficient. What can be the cause of this very significant difference?

A Closer Look at the Grazing Angle

As Figure 3 shows, the maximum radiation over a perfect infinite ground plane is at 0 degrees for the quarter-wave vertical antenna. Again, conventional wisdom suggestes that the low-angle null in Figure 4 is due to refelction cancellation. The infinite ground plane is useful only as a theoretical model, since the ground is really the spherical Earth. The EM simulation of Figure 5 shows a ¼ wave antenna over a perfectly conducting ground of varying radius. For very small ground radius there is nearly identical radiation below the ground plane, closely approximating the pattern of an antenna using ¼ wave radials. There is considerable radiation at the horizon (including below the ground plane) for all radii, however the maximum can appear only at the horizon for an infinite radius.[1-5]

The convergence to a maximum at the horizon, occurs at several hundred wavelengths away. In principle it represents a log function and thus never reaches the maximum. In practice, even 100 wavelengths at 160 meters is 16 km. The curvature of the Earth begins to influence and distort the theoretical pattern shown in Figure 3. In effect, there are two factors at work. First, the very gradual convergence to the 0 degree elevation angle maximum, and second, the significant influence of the Earth's curvature on the planar assumption. A low band vertical antenna can be thought of as an elevated vertical antenna since it is mounted on top of a sphere (Earth), not a plane. The gain maximum of a low-band ground-mounted vertical antenna will never be realized at the 0 degree elevation angle, even over sea water.

Even with a perfect ground there is a null at very low elevation angles. This has a very important effect on the over-all elevation pattern, but does not explain the additional pattern attenuation over real ground.

Another View

By using an advanced electromagnetics modeling tool we can begin to see the mechanisms of pattern creation. I have been using *EMPro*, by Agilent for designing GPS and other antennas for some time. As an aside, I modeled a quarter-wave vertical antenna — in this case at a 7.5 GHz operating frequency. The absolute numbers in the patterns at different frequencies are products of multiple variables, but the general results show pattern similarities between Figures 4 and 6. Care must be taken to ensure that the soil characteristics are nearly identical at 7.5 GHz for simulation, and at MF and low HF in practice.

Table 1.
Gain of a vertical antenna above perfect and average grounds.

Elevation angle, deg	*Perfect ground gain, dBi*	*Average ground gain dBi*	*Δ dB gain*
0	+5.14	-∞	∞
5	+5.09	-6.32	11.41
10	+4.95	-2.55	7.54
15	+4.71	-0.99	5.70
20	+4.37	-0.28	4.65
25	+3.93	-0.04	3.97
30	+3.40	-0.10	3.50
35	+2.76	-0.40	3.16
40	+2.01	-0.89	2.91
45	+1.14	-1.56	2.70

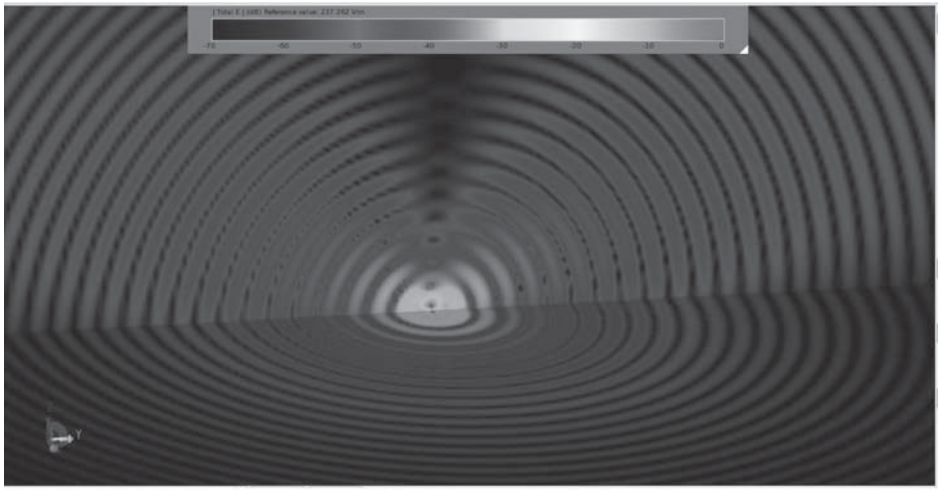

Figure 6 — *EMPro* image of both the surface and elevation angle radiated E-fields of a quarter-wave vertical antenna on average soil.

Figure 6 shows the 7.5 GHz *EMPro* simulation of both the surface and elevation angle radiated E-fields of a quarter-wave vertical antenna on average soil. As expected, Figure 6 shows no evidence of field cancellation due to reflected interfering waves. Rather, the grazing angle field intensity is equal to the field intensity along the surface of the ground. The ground intensity decreases faster than for free space due to its lossy characteristics, and the field intensity maintains a continuous function at the point of intersection with the free space just above the ground and along the surface of the ground.

FCC graphs used for plotting AM broadcast ground wave intensity for predicting coverage areas can be found at **www.fcc.gov/encyclopedia/am-broadcast-groundwave-field-strength-graphs-sections-73183-and-73184**. However, ground wave attenuation is somewhat different from the *EZNEC* and *EMPro* plots. Ground waves at MF tend to hug the ground due to a tilting of the electric fields as they propagate over lossy ground. However, for the first several wavelengths away from the antenna, lower angle radiation, in effect, is also a ground wave and is subject to the same increased attenuation as true ground waves. Thus the lower the radiation angle, the greater the ground attenuation as shown in Table 1.

Modeling the same antenna over a perfect ground yields results with much higher E-fields at the ground level, and thus in free space just above the perfect ground. With a bit of practice you can see the similarity in patterns between Figure 7 and Figure 4. In the Figure 6 far field, the blue colored — slightly left of center on the grey scale at the top of the image — field lines are more intense than the purple — extreme left on the grey scale [For color Figures see **www.arrl.org/QEXfiles** — *Ed.*]. This diagram implies a very different mechanism for pattern formation than interfering reflected waves:

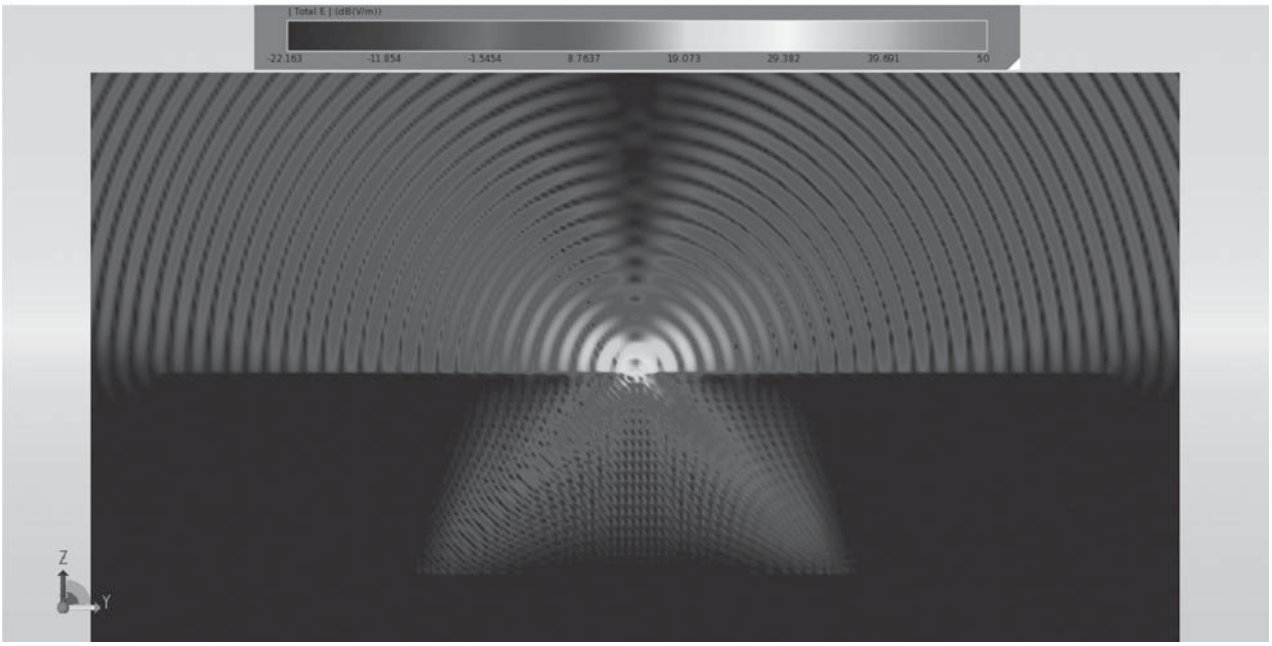

Figure 7 — Elevation plot of a base-fed ¼ λ monopole, on 24 λ diameter real ground (0.005 S/m, ε=14). Soil thickness is 5 λ. The antenna ground system is a solid ½ λ in diameter disc of a perfect conductor, to simulate a perfect antenna ground or an infinite number of ¼ λ radials.

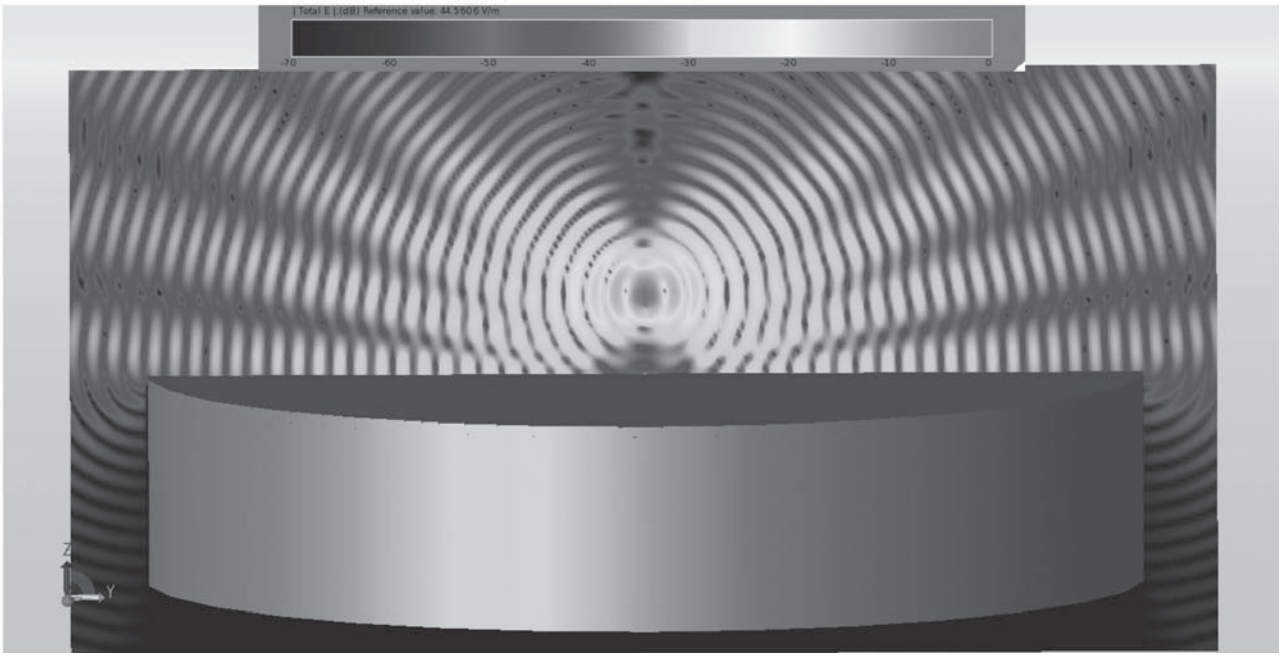

Figure 8 — The electric fields of an elevated half-wave vertical dipole, with feed point 2 wavelengths above a large slab of average ground.

ground wave attenuation as a function of ground loss. Notice that the E-field amplitude at low angles is simply attenuated faster than in free space, unlike the nearly discontinuous function the NEC models imply. Of course in the very far field, the NEC pattern becomes a good approximation, but the assumption of phase cancellation appears incorrect. The more advanced versions of *EZNEC* do permit modeling of the ground wave, but only at designated distances.

The Figure 7 simulation is the same as in Figure 6, except the ground surface field plot is removed to reveal the E-field underground. It appears from this simulation that the pseudo-Brewster angle — actually its counterpart — is formed by the attenuation of the ground-surface wave. As the radiation angle increases, its distance to the ground increases faster for a given distance from the antenna. In other words as an E-field propagates tangentially to a lossy dielectric, it is attenuated greater than in free space.

The elevation pattern is formed by the antenna's inherent pattern, and then further shaped by the lossy Earth. Also, the pattern or directivity of a ground mounted vertical antenna is independent of the antenna ground, or "image". The gain (directivity multiplied by the efficiency) *is* increased by lowering the ground losses of the antenna proper. Ground losses forming the directivity in the far field are the result of propagation

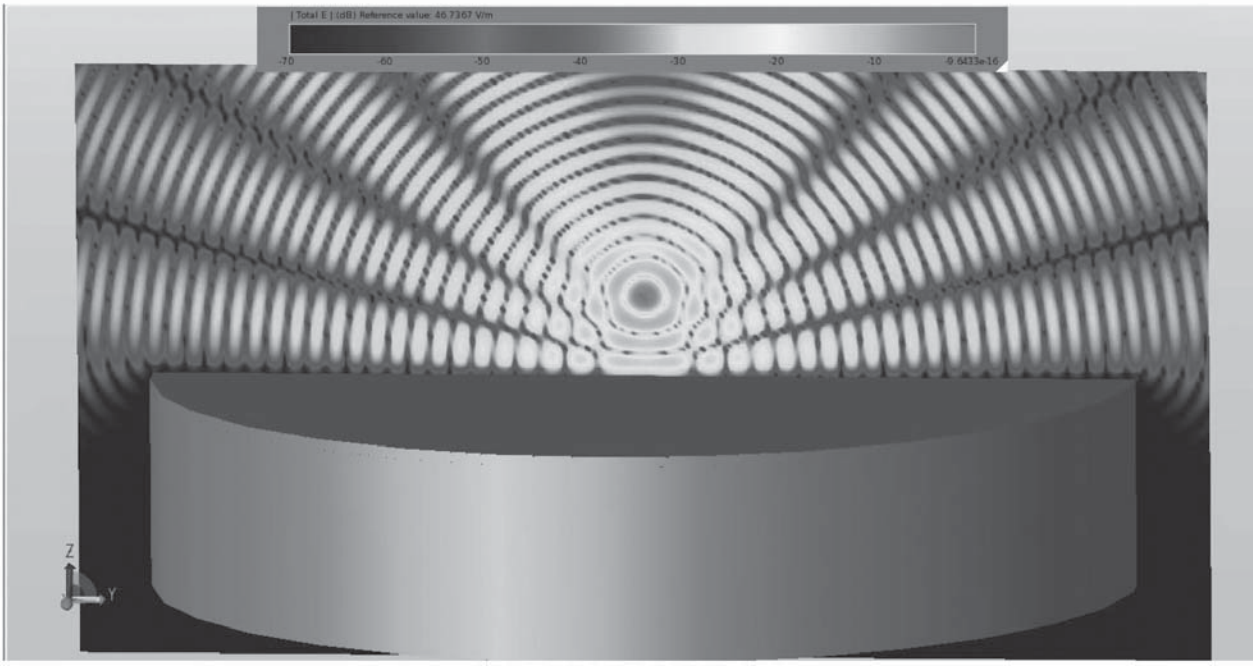

Figure 9 — The electric fields of half-wave horizontal dipole 2 wavelengths above the same average ground as in Figure 8.

losses, not antenna losses. The power that would normally be in the elevation angle close to the ground (with a perfect ground) is not cancelled because there is no cancelling wave present.

Figure 8 shows a plot of an elevated half-wave vertical dipole, with its feed point 2 wavelengths above a large slab of average ground. In this case we can clearly see the effects of reflected waves, with interfering and opposing fields creating the final pattern. If you look closely you can also see a phase difference in the various lobes that are not present in Figure 7. Here, plane waves are present and conventional wisdom of the pseudo-Brewster angle from ground reflections is valid. The cancellation and re-enforcement of far-field waves also have the effect of distorting the apparent point source of the wave. Notice that the grazing angle — lowest angle of radiation — appears to be coming from a source on the surface of the ground.

The plot of Figure 8 brings up another interesting point regarding raised vertical dipoles. The radiation resistance of a free-space vertical dipole is about 73 Ω, the same as a free-space horizontal dipole. However, as the vertical antenna is lowered closer to the ground, the radiation resistance — and in this case, also the feed-point impedance — rises to a maximum value of about 100 Ω when the end of the dipole is just above the ground surface. At lower elevations the ground actually becomes part of the antenna and thus increasing the effective height of the radiating antenna. This happens no matter what the ground characteristics are, perfect or real, and are not due to losses.

For comparison I also include a plot a half-wave horizontal dipole (Figure 9) to see the same reflected-wave cancellation mechanism at work. The view is down the axis of the dipole thus highlighting the broadside E-field pattern of the dipole. This view also shows the disc representing the real ground. Formation of nulls and peaks of gain at various elevation angels is clearly shown to be the result of reflections adding and subtracting from the field strength.

Conclusions

Antenna pattern formation by re-enforcing and cancelling reflected waves are clearly the mechanism for raised antenna systems — creating the pseudo-Brewster angle. However, for ground-mounted vertical antennas quarter-wavelength or shorter, the formation of the elevation pattern is the result of two basic mechanisms. First, there is a very slow lowering of the main pattern lobe over hundreds of wavelengths distance, and second, there is ground attenuation due to dielectric losses that result from the very low center of radiation of the vertical antenna.

There is insignificant influence of reflected waves on the antenna pattern of ground-mounted vertical antennas that are a quarter-wave or shorter height.

Bob Zavrel, W7SX, is an ARRL Life Member, Technical Advisor and Amateur Extra class licensee. He has been licensed since 1966. His primary interest in Amateur Radio is low band DXing and designing and building antennas, tuners, and amplifiers. Bob holds 5BDXCC, 5BWAZ (200), has 334 mixed, and 324 CW entities confirmed. Bob is on the DXCC Honor Roll and the CW DXCC Honor Roll, all using only tree-supported wire antennas. He also holds 9-Band DXCC on 160 through 10 meters. Previous call signs include WN9RAT, WA9RAT, WA9RAT/HR2 and SV1/W7SX.

Bob has a BS in Physics from the University of Oregon and has worked in RF engineering for over 30 years. He has five patents, and has published over 50 papers in professional and Amateur Radio publications, including the first block diagram of an SDR receiver in 1987. He was involved with the first generation of RF integrated circuits for cellular phones, and worked extensively with DDS, WLAN and passive mixer development. Bob is currently an RF Research and Development Engineer for Trimble Navigation with a primary focus on high precision GPS, down to millimeter accuracy.

Notes

[1]Z. Živković, D. Senić, C. Bodendorf, J. Skrzypczynski, and A. Šarolić, "Radiation pattern and impedance of a quarter wavelength monopole antenna above a finite ground plane", in *2012 20th International Conference on Software, Telecommunications and Computer Networks (SoftCOM),* pp. 1-5, IEEE, 11-13 Sep 2012.

[2]E. C. Jordan and K. G. Balmain, *Electromagnetic Waves and Radiating Systems*, 10th printing, 1967, Prentice-Hall Inc.

[3]R. K. Wangsness, *Electromagnetic Fields*, Wiley & Sons, 1979.

[4]J. Kraus, *Antennas*, McGraw Hill, 1988.

[5]R. C. Johnson and H. Jasik, *Antenna Engineering Handbook*, Second Edition, 1984, McGraw-Hill.

DX ENGINEERING®

8:30 am to midnight ET, Monday-Friday
1230 to 0400 UTC March-October

8:30 am to 5 pm ET, Weekends
1230 to 2100 UTC March-October

International/Tech: 330-572-3200
8:30 am to 7 pm ET, Monday-Friday
Country Code: +1 Sale Code: 1604QEX

ORDER BY 10 PM SAME-DAY SHIPPING
Mon-Fri, 10 pm ET In-Stock Items

800-777-0703 | DXEngineering.com

DX Engineering is your #1 source for antennas!

Skyhawk™ Tri-Band Yagi Antenna

The legendary Skyhawk antenna delivers the best payback in HF performance and operating ease. It boasts a trap-free design, which ensures the best bandwidth and lowest loss possible. The use of aluminum and stainless steel hardware keeps the Skyhawk's overall weight down to around 75 pounds. The Skyhawk is manufactured exclusively by DX Engineering. It is in stock and ready to ship today.

Butternut Antennas

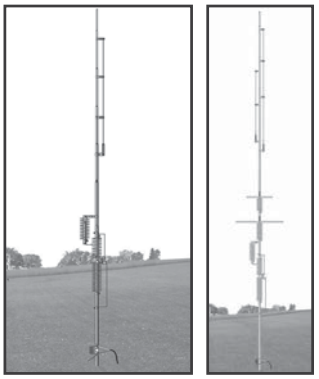

DX Engineering's Butternut Antennas line boasts three renowned designs, including 2-band, 6-band, and 9-band vertical antennas. The antennas' compact size makes them easy to install, yet they will deliver outstanding performance on each band. DX Engineering also carries a comprehensive range of repair, add-on, and replacement parts for your existing Butternut Antennas.

COMTEK Baluns

Building on the research by Jerry Sevick, W2FMI, COMTEK has designed a line of Baluns and UNUNs that are durable, highly effective and value-priced. They provide superior SWR across all HF bands. COMTEK Baluns come in 1:1 and 4:1 matching ratios, with single or dual cores.

160 Meter Thunderbolt® Vertical Antenna

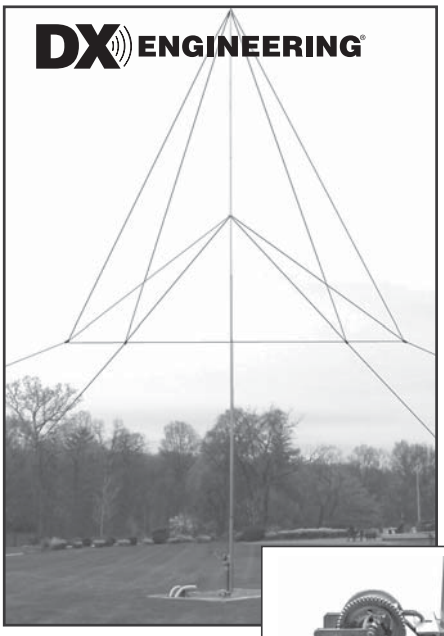

This high-efficiency vertical is made exclusively for the 160 meter band, delivering a broad 2:1 SWR bandwidth despite a relatively short 55' overall height. It handles 5 kW with anvil-like reliability. The antenna comes with DX Engineering's patented* pivoting base to make it easy to lower the antenna as needed. In fact, adding the optional manual winch makes tilting the antenna a one-person job.

*Patent no. 8,130,160

Optional manual winch, sold separately.

Maxi-Core® Current Baluns and Feedline Current Chokes

Reach your antenna's full potential by using the highest quality Maxi-Core 5, 10 and 10+ kW Baluns and Chokes. Using a legendary W8JI design, these high-efficiency, low-loss units are available in all standard ratios. Their efficient design offers the perfect balanced/unbalanced transition for maximum power delivery to your antenna.

DX Engineering Supports the VK0EK Heard Island DXpedition.

Email Support 24/7/365 at DXEngineering@DXEngineering.com ***Stay connected:***

Dr. Ulrich L. Rohde, N1UL

990 Cape Marco Island, FL 34145: **ka2weu@aol.com**

Calculation of FM and AM Noise Signals of Colpitts Oscillators in the Time Domain

Introduction

An oscillator is a combination of an amplifier, a resonator and phase modulator in a feedback loop. The value of the loop gain and its phase needs to be enough to start oscillation and after the steady state condition maintains oscillation. This is achieved either by voltage or current limiting, by AGC or limiting diodes and is well explained in [1], probably the best explanation of its kind. If such amplitude stabilization would not exist, the amplifier-oscillator would self-destruct. The limiting part of the oscillator keeps the AM (noise) well below the FM noise close-in, but very far-off they reach the same amplitude. Any deviation from this is due to a heavy unwanted non-linearity.

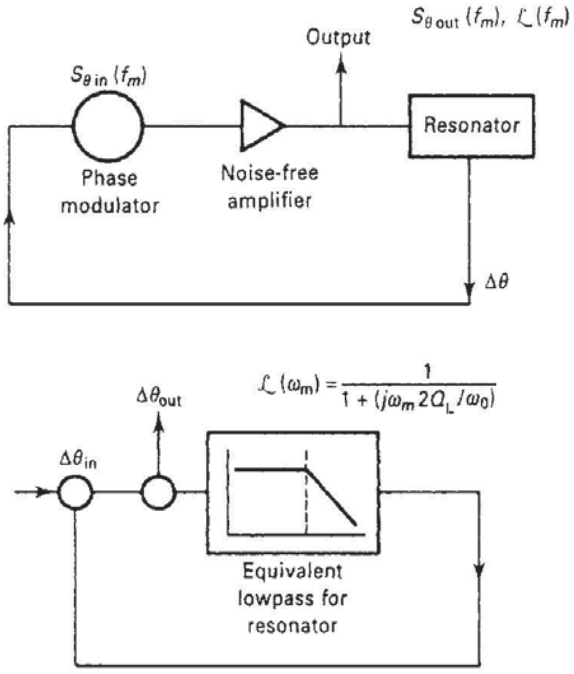

Figure 1 — Block diagram of oscillator and its low pass equivalent based on Leeson's model.

The topic here is to look at the noise of an oscillator.

The oscillator is under large signal condition and also acts like a mixer. Figure 1 shows the block diagram and its low pass equivalent based on Leeson's model [2]. The loop requirement was first mentioned in the Barkhausen analysis [3]. Initial open loop gain for getting started needs to be 3, because the steady state value is approximately 1/3 of the dc transconductance.

The noise has various sources and the following will look at all the steps [4-7]. For the reason of accuracy the following is a very detailed but complete mathematical analysis.

At the end of this, there will be a set of measurements including details about the results.

In all systems, amplifiers and oscillators, conditions of saturation (specifically with memory effects), tend to amplify AM components.

Noise Generation in Oscillators

As shown above, the qualitative linearized picture of noise generation in oscillators is very well known. The physical effects of random fluctuations taking place in the circuit are different depending on their spectral allocation with respect to the carrier:

Noise components at low frequency deviations result in frequency modulation of the carrier through mean square frequency fluctuation proportional to the available noise power.

Noise components at high frequency deviations result in phase modulation of the carrier through mean square phase fluctuation proportional to the available noise power.

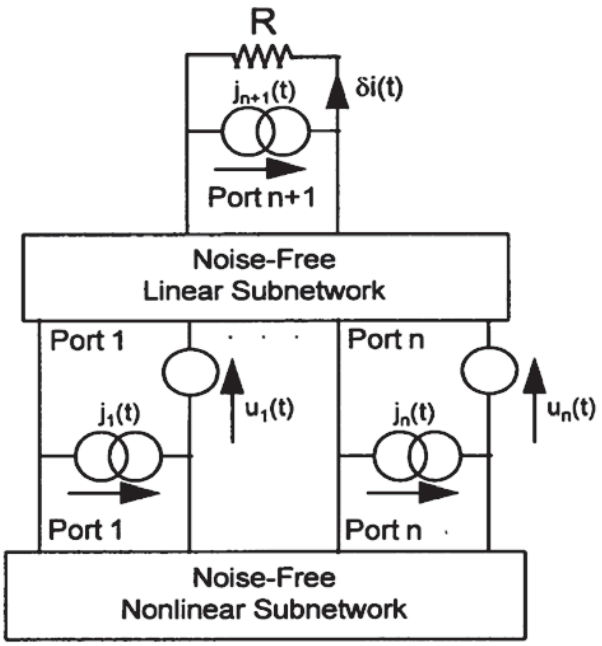

Figure 2 — Equivalent circuit of a general noisy nonlinear network

We will demonstrate that the same conclusions can be quantitatively derived from the HB equations for an autonomous circuit [5, 8].

Equivalent Representation of a Noisy Nonlinear Circuit

A general noisy nonlinear network can be described by the equivalent circuit shown in Figure 2. The circuit is divided into linear and nonlinear subnetworks as noise-free multi-ports. Noise generation is accounted for by connecting a set of noise voltage and noise current sources at the ports of the linear subnetwork [9-11].

Frequency Conversion Approach

The circuit supports a large-signal time periodic steady state of fundamental angular frequency ω_0 (carrier). Noise signals are small perturbations superimposed on the steady state, represented by families of pseudo-sinusoids located at the sidebands of the carrier harmonics. Therefore, the noise performance of the circuit is determined by the exchange of the power among the sidebands of the unperturbed steady state through frequency conversion in the nonlinear subnetwork. Due to the perturbative assumption, the nonlinear subnetwork can be replaced with a multi-frequency linear multi-port described by a conversion matrix. The flow of noise signals can be computed by means of conventional linear circuit techniques.

The frequency conversion approach frequently used has the following limitations:

The frequency conversion approach is not sufficient to predict the noise performance of an autonomous circuit. The spectral density of the output noise power, and consequently the PM noise computed by the conversion analysis are proportional to the available power of the noise sources.

- In the presence of both thermal and flicker noise sources, PM noise increases: as ω^{-1} for $\omega \to 0$; tends to a finite limit for $\omega \to \infty$.
- Frequency conversion analysis correctly predicts the far carrier noise behavior of an oscillator, and in particular the oscillator noise floor; does not provide results consistent with the physical observations at low deviations from the carrier.

This inconsistency can be removed by adding the modulation noise analysis. In order to determine the far away noise using the autonomous circuit perturbation analysis, the following applies.

The circuit supports a large-signal time-periodic autonomous regime. The circuit is perturbed by a set of small sources located at the carrier harmonics and at the sidebands at a deviation ω from carrier harmonics. The perturbation of the circuit state $(\delta \mathbf{X}_B, \delta \mathbf{X}_H)$ is given by the uncoupled sets of equations,

$$\frac{\partial E_B}{\partial E_B}\delta X_B = J_B(\omega) \quad (1)$$

$$\frac{\partial E_H}{\partial E_H}\delta X_H = J_H(\omega) \quad (2)$$

where,

E_B, E_H = vectors of HB errors

X_B, X_H = vectors of state variable (SV) harmonics (since the circuit is autonomous, one of the entries X is replaced by the fundamental frequency ω_0)

J_B, J_H = vectors of forcing terms

The subscripts B and H denote sidebands and carrier harmonics, respectively.

For a spot noise analysis at a frequency ω, the noise sources can be interpreted in either of two ways:

- Pseudo-sinusoids with random amplitude and phase located at the sidebands. Noise generation is described by Equation (1) which is essentially a frequency conversion equation relating the sideband harmonics of the state variables and of the noise sources. This description is exactly equivalent to the one provided by the frequency conversion approach. This mechanism is referred to as *conversion noise* [12-15].

Sinusoids located at the carrier harmonics are randomly phase-and-amplitude-modulated by pseudo-sinusoidal noise at frequency ω. Noise generation is described by Equation (2), which describes noise-induced jitter of the circuit-state, represented by the vector δX_H. The modulated perturbing signals are represented by replacing the entries of J_H with the complex modulation laws. This mechanism is referred to as *modulation noise*. One of the entries of δX_H is $\delta\omega_0$ where $\delta\omega_0(\omega)$ = phasor of the pseudo-sinusoidal components of the fundamental frequency fluctuations in a 1 Hz band at frequency ω. Equation (2) provides a frequency jitter with a mean square value proportional to the available noise power. In the presence of both thermal and flicker noise, PM noise raises as ω^{-3} for $\omega \to 0$ and tends to 0 for $\omega \to \infty$. Modulation noise analysis correctly describes the noise behavior of an oscillator at low deviations from the carrier and does not provide results consistent with physical observations at high deviations from the carrier.

The combination of both phenomena explains the noise in the oscillator shown in Figure 3, where the near carrier noise dominates below ω_X and far carrier noise dominates above ω_X.

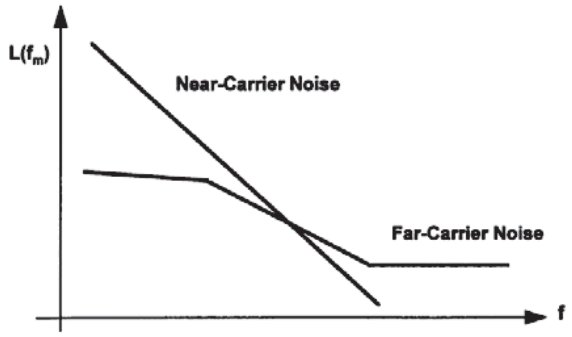

Figure 3 — Oscillator noise components.

Figure 4 (itemized form) shows the noise sources as they are applied at the IF. We have arbitrarily defined the low oscillator output as IF. This applies to the conversion matrix calculation.

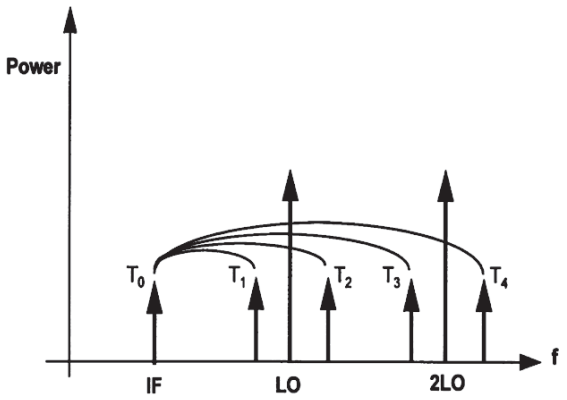

Figure 4 — Noise sources where the noise at each sideband contributes to the output noise at the IF through frequency conversion.

Figure 5 shows the total contributions which have to be taken into consideration for calculation of the noise at the output. The accuracy of the calculation of the phase noise depends highly on the quality of the parameter extraction for the nonlinear device; in particular, high frequency phenomena must be properly modeled. In addition, the flicker noise contribution is essential. This is also valid for mixer noise analysis.

Conversion Noise Analysis

The actual mathematics used to calculate the noise result (Ansoft Serenade 8.*x*) is as follows [19],

k^{th} harmonic PM noise:

$$\left\langle \left|\delta\Phi_k(\omega)\right|^2 \right\rangle = \frac{N_k(\omega) - N_{-k}(\omega) - 2\,\mathrm{Re}\left[C_k(\omega)\right]}{R\left|I_k^{SS}\right|^2} \tag{3}$$

k^{th} harmonic AM noise:

$$\left\langle \left|\delta A_k(\omega)\right|^2 \right\rangle = 2\,\frac{N_k(\omega) - N_{-k}(\omega) + 2\,\mathrm{Re}\left[C_k(\omega)\right]}{R\left|I_k^{SS}\right|^2} \tag{4}$$

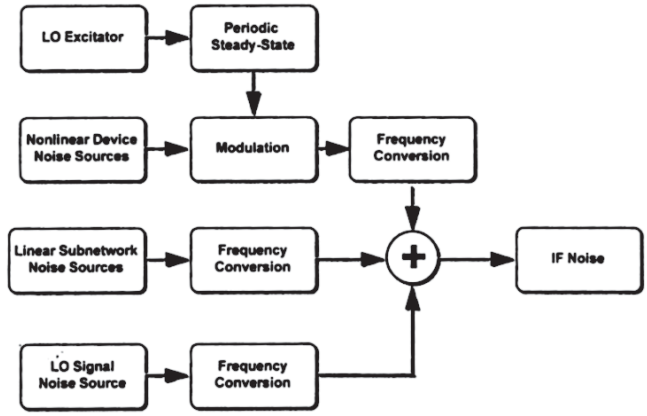

Figure 5 — Noise mechanisms.

k^{th} harmonic PM-AM correlation coefficient:

$$C_k^{PMAM}(\omega) = \left\langle \delta\Phi_k(\omega)\delta A_k(\omega)^* \right\rangle = -\sqrt{2}\,\frac{2\,\mathrm{Im}\left[C_k(\omega)\right] + j\left[N_k(\omega) - N_{-k}(\omega)\right]}{R\left|I_k^{SS}\right|^2} \tag{5}$$

where

$N_k(\omega)$, $N_{-k}(\omega)$ = noise power spectral densities at the upper and lower sidebands of the k^{th} harmonic

$C_k(\omega)$ = normalized correlation coefficient of the upper and lower sidebands of the k^{th} carrier harmonic

R = load resistance

I_k^{SS} = k^{th} harmonic of the steady-state current through the load.

Modulation Noise Analysis

k^{th} harmonic PM noise:

$$\left\langle \left|\delta\Phi_k(\omega)\right|^2 \right\rangle = \frac{k^2}{\omega^2}\,\mathbf{T}_F \left\langle \mathbf{J}_H(\omega)\mathbf{J}_H^t(\omega) \right\rangle \mathbf{T}_F^t \tag{6}$$

k^{th} harmonic AM noise:

$$\left\langle \left|\delta A_k(\omega)\right|^2 \right\rangle = \frac{2}{\left|I_k^{SS}\right|^2}\,\mathbf{T}_{Ak} \left\langle \mathbf{J}_H(\omega)\mathbf{J}_H^t(\omega) \right\rangle \mathbf{T}_{Ak}^t \tag{7}$$

k^{th} harmonic PM-AM correlation coefficient:

$$C_k^{PMAM}(\omega) = \left\langle \delta\Phi_k(\omega)\delta A_k(\omega)^* \right\rangle = \frac{k\sqrt{2}}{j\omega\left|I_k^{SS}\right|^2}\,\mathbf{T}_F \left\langle \mathbf{J}_H(\omega)\mathbf{J}_H^t(\omega) \right\rangle \mathbf{T}_{Ak}^t \tag{8}$$

where

$J_H(\omega)$ = vector of Norton equivalent of the noise sources

$\mathbf{T}_F$ = frequency transfer matrix

R = load resistance

I_k^{ss} = k^{th} harmonic of the steady-state current through the load.

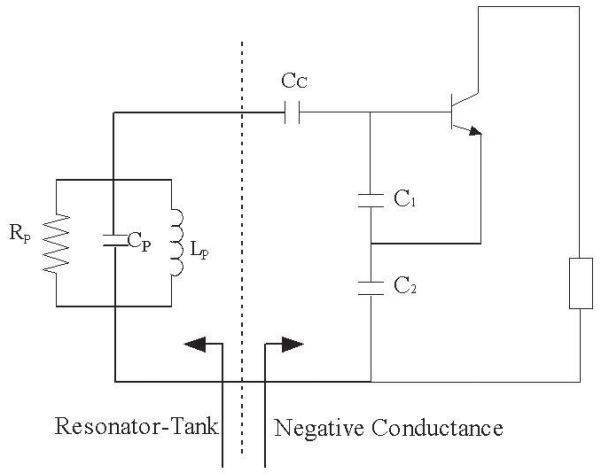

Figure 6 — Colpitts Oscillator configuration for the intrinsic case, no parasitics assumed, and an ideal transistor considered.

The following two circuits show the transition from a series tuned circuit connected with the series time-dependent negative resistance and the resulting input capacitance marked C_{IN}. Translated, the resulting configuration consists of a series circuit with inductance L and the resulting capacitance C'. The noise voltage $e_N(t)$ describes a small perturbation, which is the noise resulting from R_L and $-R_N(t)$. Figure 7 shows the equivalent representation of the oscillator circuit in the presence of noise.

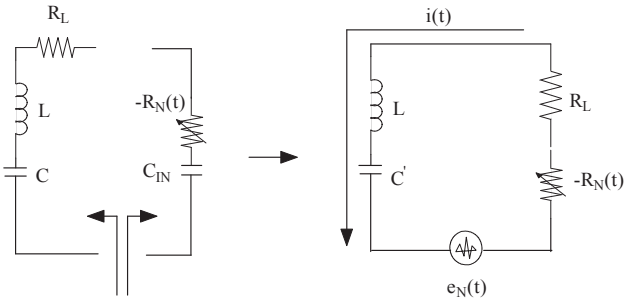

Figure 7 — Equivalent representation of the oscillator circuit in presence of noise.

The circuit equation of the oscillator circuit of Figure 7 can be given as

$$L\frac{di(t)}{dt}+(R_L-R_N(t))i(t)+\frac{1}{C'}\int i(t)dt=e_N(t) \qquad (9)$$

where $i(t)$ is the time varying resultant current. Due to the noise voltage $e_N(t)$, Equation (9) is a nonhomogeneous differential equation. If the noise voltage is zero, it translates into a homogeneous differential equation.

For a noiseless oscillator, the noise signal $e_N(t)$ is zero and the expression of the free-running oscillator current $i(t)$ can be assumed to be a periodic function of time and can be given as

$$i(t)=I_1\cos(\omega t+\varphi_1)+I_2\cos(2\omega t+\varphi_2) \qquad (10)$$
$$+I_3\cos(3\omega t+\varphi_3)+.....I_n\cos(n\omega t+\varphi_n)$$

where I_1, I_2 …..I_n, are peak harmonic amplitudes of the current and φ_1, φ_2…..φ_n are time invariant phases.

In the presence of the noise perturbation $e_N(t)$, the current $i(t)$ may no longer be a periodic function of time and can be expressed as

$$i(t)=I_1(t)\cos[\omega t+\varphi_1(t)]+I_2(t)\cos[2\omega t+\varphi_2(t)]+ \qquad (11)$$
$$I_3(t)\cos[3\omega t+\varphi_3(t)]+\ ....I_{n-2}(t)\cos[(n-2)\omega t+\varphi_{n-2}(t)]+$$
$$I_{n-1}(t)\cos[(n-1)\omega t+\varphi_{n-1}(t)]+I_n(t)\cos[n\omega t+\varphi_n(t)]$$

where $I_1(t)$, $I_2(t)$…..$I_n(t)$ are time variant amplitudes of the current and $\varphi_1(t)$, $\varphi_2(t)$…..$\varphi_n(t)$ are time variant phases.

Considering that $I_n(t)$ and $\varphi_n(t)$ do not change much over the period of $2\pi/n\omega$, each corresponding harmonic over one period of oscillation cycle remains small and more or less invariant. The solution of the differential equation becomes easy since the harmonics are suppressed due to a $Q > 10$, which prevents $i(t)$ to flow for the higher terms.

After the substitution of the value of di/dt and $\int i(t)dt$, the complete oscillator circuit equation, as given in Equation (9), can be rewritten as

$$L\{$$
$$-I_1(t)(\omega+\frac{d\varphi_1(t)}{dt})\sin[\omega t+\varphi_1(t)]+\frac{dI_1(t)}{dt}\cos[\omega t+\varphi_1(t)]+$$
$$-I_2(t)(2\omega+\frac{d\varphi_2(t)}{dt})\sin[2\omega t+\varphi_2(t)]+\frac{dI_2(t)}{dt}\cos[2\omega t+\varphi_2(t)]+$$
$$-I_3(t)(3\omega+\frac{d\varphi_3(t)}{dt})\sin[3\omega t+\varphi_3(t)]+\frac{dI_3(t)}{dt}\cos[3\omega t+\varphi_3(t)]+...$$
$$-I_n(t)(n\omega+\frac{d\varphi_n(t)}{dt})\sin[n\omega t+\varphi_n(t)]+\frac{dI_n(t)}{dt}\cos[n\omega t+\varphi_n(t)]\}+$$
$$[(R_L-R_N(t))i(t)]+$$

$$\frac{1}{C'}\left\{\begin{array}{l}\left[\left[\frac{I_1(t)}{\omega}-\frac{I_1(t)}{\omega^2}\left(\frac{d\varphi_1(t)}{dt}\right)\right]\sin[\omega t+\varphi_1(t)]+\\ \frac{1}{\omega^2}\left(\frac{dI_1(t)}{dt}\right)\cos[\omega t+\varphi_1(t)]\end{array}\right\}+$$

$$\frac{1}{C'}\left\{\begin{array}{l}\left[\left[\frac{I_2(t)}{2\omega}-\frac{I_2(t)}{4\omega^2}\left(\frac{d\varphi_2(t)}{dt}\right)\right]\sin(2\omega t+\varphi_2(t)\right.\\ \left.+\frac{1}{4\omega^2}\left(\frac{dI_2(t)}{dt}\right)\cos(2\omega t+\varphi_2(t))\right.\end{array}\right\}+$$

$$\frac{1}{C'}\left\{\begin{array}{l}\left[\left[\frac{I_3(t)}{3\omega}-\frac{I_3(t)}{9\omega^2}\left(\frac{d\varphi_3(t)}{dt}\right)\right]\sin[3\omega t+\varphi_3(t)]+\\ \frac{1}{9\omega^2}\left(\frac{dI_3(t)}{dt}\right)\cos[3\omega t+\varphi_3(t)]\end{array}\right\}+\ldots$$

$$\frac{1}{C'}\left\{\begin{array}{l}\left[\left[\frac{I_n(t)}{n\omega}-\frac{I_n(t)}{n^2\omega^2}\left(\frac{d\varphi_n(t)}{dt}\right)\right]\sin[n\omega t+\varphi_n(t)]\right.\\ \left.+\frac{1}{n^2\omega^2}\left(\frac{dI_n(t)}{dt}\right)\cos[n\omega t+\varphi_n(t)]\right.\end{array}\right\}=e_N(t) \tag{12}$$

Because Q > 10 we approximate:

$$\frac{di(t)}{dt}=-I_1(t)(\omega+\frac{d\varphi_1(t)}{dt})\sin[\omega t+\varphi_1(t)]$$
$$+\frac{dI_1(t)}{dt}\cos[\omega t+\varphi_1(t)]+$$

+ (a slowly varying function at higher order harmonics of a very small amount).

$$\int i(t)dt=\left[\frac{I_1(t)}{\omega}-\frac{I_1(t)}{\omega^2}\left(\frac{d\varphi_1(t)}{dt}\right)\right]\sin[\omega t+\varphi_1(t)]$$

$$+\frac{1}{\omega^2}\left(\frac{dI_1(t)}{dt}\right)\cos[\omega t+\varphi_1(t)]+$$

+ (a slowly varying function at higher order harmonics of a very small amount).

After the substitution of the value of di/dt and $\int i(t)dt$, the oscillator circuit Equation (12) can be rewritten as

$$L\left[\begin{array}{l}-I_1(t)(\omega+\frac{d\varphi_1(t)}{dt})\sin[\omega t+\varphi_1(t)]\\ +\frac{dI_1(t)}{dt}\cos[\omega t+\varphi_1(t)]\end{array}\right]+\left[(R_L-R_N(t))I(t)\right]+$$

$$\frac{1}{C}\left\{\begin{array}{l}\left[\left[\frac{I_1(t)}{\omega}-\frac{I_1(t)}{\omega^2}\left(\frac{d\varphi_1(t)}{dt}\right)\right]\sin[\omega t+\varphi_1(t)]\right.\\ \left.+\frac{1}{\omega^2}\left(\frac{dI_1(t)}{dt}\right)\cos[\omega t+\varphi_1(t)]\right.\end{array}\right\}=e_N(t) \tag{13}$$

Following [18], and for simplification purposes, the equations above are multiplied with $\sin[\omega t+\varphi_1(t)]$ or $\cos[\omega t+\varphi_1(t)]$ and integrated over one period of the oscillation cycle, which will give an approximate differential equation for phase $\varphi(t)$ and amplitude $i(t)$ as

$$\left[\frac{2}{IT_0}\right]\int_{t-T_0}^{t}e_N(t)\sin[\omega t+\varphi(t)]dt$$
$$=-\frac{d\varphi}{dt}\left[L+\frac{1}{\omega^2C'}\right]+\left[-\omega L+\frac{1}{\omega C'}\right] \tag{14}$$

$$\left[\frac{2}{T_0}\right]\int_{t-T_0}^{t}e_N(t)\cos[\omega t+\varphi(t)]dt$$
$$=\frac{dI(t)}{dt}\left[L+\frac{1}{\omega^2C'}\right]+\left[R_L-\overline{R_N(t)}\right]I(t) \tag{15}$$

where $\overline{R_N(t)}$ is the average negative resistance under large signal condition.

$$\overline{R_N(t)}=\left[\frac{2}{T_0I}\right]\int_{t-T_0}^{t}R_N(t)I(t)\cos^2[\omega t+\varphi)]dt \tag{16}$$

Since the magnitude of the higher harmonics are not significant, the subscript of $\varphi(t)$and $I(t)$are dropped. Based on [18], we now determine the negative resistance.

Calculation of the Region of the Nonlinear Negative Resistance

Under steady-state free running oscillation condition,

$$\frac{dI(t)}{dt}\rightarrow 0$$

implies steady current, and

$$e_N(t)\rightarrow 0$$

with I is the fundamental RF current. Solving the now homogeneous differential equation for R_L - $R_N(t)$ and inserting the two terms into 15, we obtain

$$\left[\frac{2}{T_0}\right]\int_{t-T_0}^{t}e_N(t)\cos[\omega t+\varphi(t)]dt=$$
$$\frac{dI}{dt}\left[L+\frac{1}{\omega^2C'}\right]+\left[R_L-\overline{R_N(t)}\right]I(t) \tag{17}$$

term $\rightarrow 0$

now we introduce

γ; $\gamma=\Delta R/\Delta I$; for $\Delta\rightarrow 0, \gamma\rightarrow 0$

and $[R_L-\overline{R_N(t)}]=\gamma\ \Delta I$

$$\gamma\rightarrow 0\Rightarrow[R_L-\overline{R_N(t)}]I(t)\rightarrow 0 \tag{18}$$

$$R_L - \overline{R_N(t)} = R_{Load} - \left[\frac{2}{T_0}\right]\int_{t-T_0}^{t} R_N(t)\cos^2[\omega t + \varphi(t)]dt \to 0 \quad (19)$$

$[R_L - \overline{R_N(t)}]I(t) \to 0$ gives the intersection of $[\overline{R_N(t)}]$ and $[R_L]$. This value is defined as I_0 which is the minimum value of the current needed for the steady-state sustained oscillation condition.

Figure 8 shows the plot of the nonlinear negative resistance, which is a function of the amplitude of the RF current. As the RF amplitude gets larger the conducting angle becomes narrower.

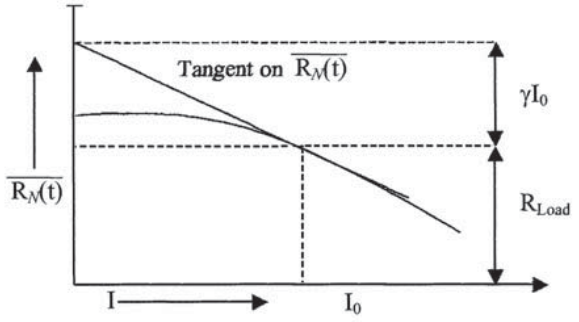

Figure 8 — Plot of negative resistance of $[\overline{R_N(t)}]$ *vs.* amplitude of current *I*.

For a small variation of the current ΔI from I_0, the relation above is expressed as

$$[R_L - \overline{R_N(t)}] = \gamma\ \Delta I \quad (20)$$

$\gamma\,\Delta I$ can be found from the intersection on the vertical axis by drawing the tangential line on $[\overline{R_N(t)}]$ at $I = I_0$. $|\Delta I|$ decreases exponentially with time for $\gamma > 0$.

Hence, I_0 represents the stable operating point. On the other hand, if $[\overline{R_N(t)}]$ intersects $[R_L]$ from the other side for $\gamma<0$ then $|\Delta I|$ grows indefinitely with time. Such an operating point does not support stable operation [18].

Calculation of the Noise Signal in Time Domain

From solving the two orthogonal equations, we need to obtain information about current $I(t)$ and $\varphi(t)$.

$$\left[\frac{2}{IT_0}\right]\int_{t-T_0}^{t} e_N(t)\sin[\omega t + \varphi(t)]dt = -\frac{d\varphi(t)}{dt}\left[L + \frac{1}{\omega^2 C'}\right] + \left[-\omega L + \frac{1}{\omega C'}\right] \quad (21)$$

$$\left[\frac{2}{T_0}\right]\int_{t-T_0}^{t} e_N(t)\cos[\omega t + \varphi(t)]dt = \frac{dI(t)}{dt}\left[L + \frac{1}{\omega^2 C'}\right] + \left[R_L - \overline{R_N(t)}\right]I(t) \quad (22)$$

The analysis of the noise signal can be accomplished by decomposing the noise signal $e_N(t)$ to an infinite number of random noise pulses represented by

$$\varepsilon\,\delta(t - t_0) \quad (23)$$

where ε is the strength of the pulse at the time instant t_0, and both ε and t_0 are independent random variables from one pulse to next pulse!

The time average of the square of the current pulses over a period of time can be shown to be

$$\frac{1}{2T}\int_{-T}^{T}\left[\sum \varepsilon\,\delta(t - t_0)\right]^2 dt = \overline{e_N^2(t)} \quad (24)$$

The mean square noise voltage $\overline{e_N^2(t)}$ is generated in the circuit in Figure 7.

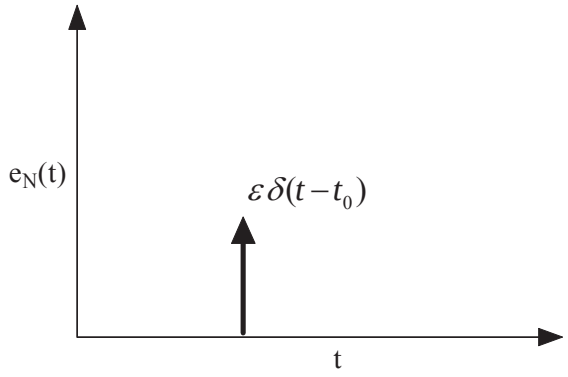

Figure 9 — The noise pulse at $I = t_0$.

Figure 9 shows the noise pulse at time instant $t = t_0$.

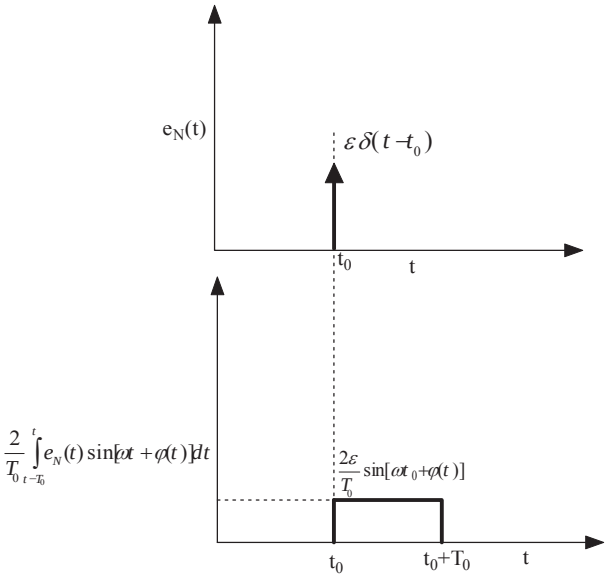

Figure 10 — The amplitude of the rectangular pulse.

The integral of the single noise pulse above gives the rectangular pulse with the height $\left[\frac{2}{T_0}\right]\varepsilon \sin[\omega t + \varphi(t)]$ and the length of T_0 as shown in Figure 10.

The integration of the single elementary noise pulse, following the Dirac Δ function, results in

$$\left[\frac{2}{T_0}\right]\int_{t-T_0}^{t} e_N(t)\sin[\omega t + \varphi(t)]dt \tag{25}$$

$$\approx \left[\frac{2}{T_0}\right]\int_{t-T_0}^{t} \varepsilon\,\delta(t-t_0)\sin[\omega t + \varphi(t)]dt]$$

$$\left[\frac{2}{T_0}\right]\int_{t-T_0}^{t} \varepsilon\,\delta(t-t_0)\sin[\omega t + \varphi(t)]dt \tag{26}$$

$$\approx \left[\frac{2}{T_0}\right]\varepsilon \sin[\omega t_0 + \varphi(t)]$$

since the length of time T_0 is considered to be sufficiently small for any variation of $\varphi(t)$and $I(t)$ during the time T_0. The corresponding rectangular pulse of the magnitude $\frac{2}{T_0}\varepsilon \sin[\omega t_0 + \varphi(t)]$ is considered to be another pulse located at $t = t_0$ and can be expressed in the form of an impulse function with the amplitude $2\varepsilon \sin[\omega t_0 + \varphi(t)$ located at $t = t_0$ for calculating the effect using Equations (21) and (22).

The effect of $\left[\frac{2}{T_0}\right]\int_{t-T_0}^{t} e_N(t)\sin[\omega t + \varphi(t)]dt$ is given by $[n_1(t)]$ which consists of a number of rectangular pulses. The time average of the square of these pulses, following [18], can be calculated as

$$\frac{1}{2T}\int_{t=-T}^{t=T}\left[\sum 2\varepsilon \sin(\omega t_0 + \varphi(t))\delta(t-t_0)\right]^2 dt \tag{27}$$

$$= \frac{1}{T}\int_{t=-T}^{t=T}\left[\sum \varepsilon\,\delta(t-t_0)\right]^2 dt$$

$$\overline{e_N^2(t)} = \frac{1}{2T}\int_{-T}^{T}\left[\sum \varepsilon\,\delta(t-t_0)\right]^2 dt \tag{28}$$

From the equation above,

$$\overline{n_1^2(t)} = 2\overline{e_N^2(t)} \tag{29}$$

Similarly, the total response of $\frac{2}{T_0}\int_{t-T_0}^{t} e_N(t)\cos[\omega t + \varphi(t)]dt$ can be expressed by $[n_2(t)]$, which consists of a large number of such pulses and the time average of the square of these pulses is

$$\overline{n_2^2(t)} = 2\overline{e_N^2(t)} \tag{30}$$

since $\frac{2}{T_0}\int_{t-T_0}^{t} e_N(t)\sin[\omega t + \varphi(t)]dt$

and $\frac{2}{T_0}\int_{t-T_0}^{t} e_N(t)\cos[\omega t + \varphi(t)]dt$ are orthogonal functions, and in the frequency domain are the upper and lower side bands relative to the carrier, and the correlation of $[n_1(t)]$ and $[n_2(t)]$ is

$$\overline{n_1(t)n_2(t)} = 0 \tag{31}$$

Now consider the narrow band noise signal, which is

$$e_N(t) = e_{N1}(t) + e_{N2}(t) \tag{32}$$

$$e_{N1}(t) = e_1(t)\sin[\omega_0 t + \varphi(t)] \tag{33}$$

$$e_{N2}(t) = -e_2(t)\cos[\omega_0 t + \varphi(t)] \tag{34}$$

where $e_{N1}(t)$ and $e_{N2}(t)$ are orthogonal functions, and $e_1(t)$ and $e_2(t)$ are slowly varying functions of time.

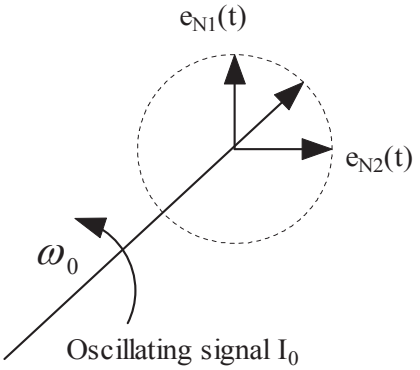

Figure 11 — Vector presentation of the oscillator signal and its modulation by the voltage e_{N1} and e_{N2}.

The calculation of $I_n(t)$ and $\varphi_n(t)$ for the free running oscillator can be derived from Equations (21) and (22) as

$$\left[\frac{2}{IT_0}\right]\int_{t-T_0}^{t} e_N(t)\sin[\omega t + \varphi(t)]dt \tag{35}$$

$$= -\frac{d\varphi(t)}{dt}\left[L + \frac{1}{\omega^2 C}\right] + \left[-\omega L + \frac{1}{\omega C}\right]$$

$$\left[\frac{2}{IT_0}\right]\int_{t-T_0}^{t} e_N(t)\sin[\omega t+\varphi(t)]dt \Rightarrow \left[\frac{1}{I}\right]n_1(t) \tag{36}$$

at resonance frequency $\omega = \omega_0$,

$$\left\{-\frac{d\varphi(t)}{dt}\left[L+\frac{1}{\omega^2 C'}\right]+\left[-\omega L+\frac{1}{\omega C'}\right]\right\}_{\omega=\omega_0} \tag{37}$$

$$= -2L\frac{d\varphi(t)}{dt}$$

and

$$\frac{1}{I}n_1(t) = -2L\frac{d\varphi(t)}{dt} \tag{38}$$

$$\frac{d\varphi(t)}{dt} = -\left[\frac{1}{2LI}\right]n_1(t) \tag{39}$$

If Equation (39) is transformed in the frequency domain, $\varphi(t)$ can be expressed as

$$\varphi(f) = \frac{n_1(f)}{2\omega LI} \tag{40}$$

Now the spectral density of $[\varphi(f)]$ is

$$\left|\varphi(f)\right|^2 = \frac{1}{4\omega^2 L^2 I^2}\left|n_1(f)\right|^2 \tag{41}$$

$$\frac{1}{4\omega^2 L^2 I^2}\left|n_1(f)\right|^2 = \frac{2\left|e_N(f)\right|^2}{4\omega^2 L^2 I^2}$$

$$\Rightarrow \left|\varphi(f)\right|^2 = \frac{2\left|e_N(f)\right|^2}{4\omega^2 L^2 I^2} \tag{42}$$

where f varies from $-\infty$ to $+\infty$.

The amplitude of the current can be written as $I(t) = I_0 + \Delta I(t)$, where I_0 represents the stable operating point of the free-running oscillator with a loop gain slightly greater than 1.

From Equation (22), we can calculate

$$\frac{2}{T_0}\int_{t-T_0}^{t} e_N(t)\cos[\omega t+\varphi(t)]dt$$

$$= \frac{dI(t)}{dt}\left(L+\frac{1}{\omega^2 C'}\right)+\left[R_L-\overline{R_N(t)}\right]I(t),$$

$$\left[\frac{2}{T_0}\int_{t-T_0}^{t} e_N(t)\cos[\omega t+\varphi(t)]dt\right]_{\omega=\omega_0} \tag{43}$$

$$= \left[2L\frac{\partial}{\partial t}[\Delta I(t)]+\Delta I(t)I_0\gamma+\Delta I^2(t)\gamma\right]$$

Since the amplitude of $\Delta I^2(t)$ is negligible, its value can be set to 0;

$$\left[2L\frac{\partial}{\partial t}[\Delta I(t)]+\Delta I(t)I_0\gamma+\Delta I^2(t)\gamma\right] \tag{44}$$

$$= 2L\frac{\partial}{\partial t}[\Delta I(t)]+\Delta I(t)I_0\gamma$$

$$n_2(t) = \frac{2}{T_0}\int_{t-T_0}^{t} e_N(t)\cos[\omega t+\varphi(t)]dt \tag{45}$$

$$n_2(t) = 2L\frac{\partial}{\partial t}[\Delta I(t)]+\Delta I(t)I_0\gamma \tag{46}$$

$$n_2(f) = 2L\omega\,\Delta I(f)+\Delta I(f)I_0\gamma \tag{47}$$

The spectral density of $[n_2(f)]$ is

$$\left|n_2(f)\right|^2 = [4L^2\omega^2+(I_0\gamma)^2]\left|\Delta I(f)\right|^2 \tag{48}$$

and the spectral density of $\Delta I(f)$ can be expressed in terms of $\left|n_2(f)\right|^2$ as

$$\left|\Delta I(f)\right|^2 = \frac{1}{[4L^2\omega^2+(I_0\gamma)^2]}\left|n_2(f)\right|^2 \tag{49}$$

$$\left|n_2(f)\right|^2 = 2\left|e_N(f)\right|^2$$

$$\Rightarrow \left|\Delta I(f)\right|^2 = \frac{2\left|e_N(f)\right|^2}{[4L^2\omega^2+(I_0\gamma)^2]} \tag{50}$$

since $n_1(t)$ and $n_2(t)$ are orthogonal function and there is no correlation between current and phase

$$\overline{n_1(t)n_2(t)} = 0 \Rightarrow \overline{I(t)\varphi(t)} = 0 \tag{51}$$

The output power noise spectral density of the current is given as

$$P_{noise}(f) = 2R_L\left|I(f)\right|^2 \tag{52}$$

The noise spectral density of the current is given as

$$\left|I(f)\right|^2 = \int_{-\infty}^{\infty} R_I(\tau)\exp(-j\omega\tau)d\tau \tag{53}$$

where $R_I(\tau)$ is the auto-correlation function of the current and can be written as

$$R_I(\tau)=\overline{\left[\begin{array}{l} I(t)I(t+\tau)\cos[\omega_0 t+\varphi(t)]\cos[\omega_0(t+\tau) \\ +\varphi(t+\tau)] \end{array}\right]} \tag{54}$$

$$R_I(\tau)=\frac{1}{2}\left[I_0^2+R_{\Delta I}(\tau)\right]\cos(\omega_0\tau)[\overline{\cos(\varphi(t+\tau)-\varphi(t))}] \tag{55}$$

Since $I(t)$ and $\varphi(t)$ are uncorrelated, auto-correlation function o f the current $R_I(\tau)$ can be given as

From [18], but taking into consideration that both side bands are correlated, we can write

$$R_I(\tau)=\frac{1}{2}\left[I_0^2+\frac{2|e_N(\tau)|^2}{2L\gamma I_0}\exp\left(-\frac{\gamma I_0}{2L}|\tau|\right)\right] \tag{56}$$

$$\exp\left(-\frac{|e_N(\tau)|^2}{4L^2I_0^2}|\tau|\right)\cos(\omega_0\tau)$$

Since the publication [18] skipped many stages of the calculation, up to here, a more complete and detailed flow is shown. These results are needed to calculate the noise performance at the component level later. Note the factor of 2, which results from the correlation.

Considering $\frac{\gamma I_0}{2L} >> \frac{2|e_N(\tau)|^2}{4L^2I_0^2}$, the noise spectral density of the current is given by

$$|I(f)|^2=\int_{-\infty}^{\infty}R_I(\tau)\exp(-j\omega\tau)d\tau \tag{57}$$

with $I = I_0 + \Delta I(t)$; all RF-currents.

$$|I(f)|^2=\frac{|e_N(f)|^2}{8L^2}\left[\begin{array}{l} \dfrac{1}{(\omega-\omega_0)^2+\left(\dfrac{|e_N(f)|^2}{4L^2I_0^2}\right)^2} \\ +\dfrac{1}{(\omega+\omega_0)^2+\left(\dfrac{|e_N(f)|^2}{4L^2I_0^2}\right)^2} \end{array}\right]+$$

$$\frac{|e_N(f)|^2}{8L^2}\left[\begin{array}{l} \dfrac{1}{(\omega-\omega_0)^2+\left(\dfrac{\gamma I_0}{2L}\right)^2} \\ +\dfrac{1}{(\omega+\omega_0)^2+\left(\dfrac{\gamma I_0}{2L}\right)^2} \end{array}\right] \tag{58}$$

With

$$\frac{|e_N(f)|^2}{8L^2}\left[\begin{array}{l} \dfrac{1}{(\omega-\omega_0)^2+\left(\dfrac{|e_N(f)|^2}{4L^2I_0^2}\right)^2} \\ +\dfrac{1}{(\omega+\omega_0)^2+\left(\dfrac{|e_N(f)|^2}{4L^2I_0^2}\right)^2} \end{array}\right]\rightarrow \text{FM noise} \tag{59}$$

$$\frac{|e_N(f)|^2}{8L^2}\left[\begin{array}{l} \dfrac{1}{(\omega-\omega_0)^2+\left(\dfrac{\gamma I_0}{2L}\right)^2} \\ +\dfrac{1}{(\omega+\omega_0)^2+\left(\dfrac{\gamma I_0}{2L}\right)^2} \end{array}\right]\rightarrow \text{AM noise} \tag{60}$$

Since

$$\frac{\gamma I_0}{2L} >> \frac{2|e_N(\tau)|^2}{4L^2I_0^2}$$

for $\omega\rightarrow\omega_0$, FM noise predominates over the AM noise.

For $\omega>>\omega_0$, both the FM noise and AM noise terms give equal contribution.

Considering $\omega+\omega_0>>\omega-\omega_0$, then

$$|I(f)|^2=\frac{|e_N(f)|^2}{8L^2}\left[\begin{array}{l} \dfrac{1}{(\omega-\omega_0)^2+\left(\dfrac{|e_N(f)|^2}{4L^2I_0^2}\right)^2} \\ +\dfrac{1}{(\omega-\omega_0)^2+\left(\dfrac{\gamma I_0}{2L}\right)^2} \end{array}\right] \tag{61}$$

$$P_{noise}(f)=2R_L|I(f)|^2 \tag{62}$$

$$P_{noise}(f)=2R_L\left(\frac{|e_N(f)|^2}{8L^2}\right)\left[\begin{array}{l} \dfrac{1}{(\omega-\omega_0)^2+\left(\dfrac{|e_N(f)|^2}{4L^2I_0^2}\right)^2} \\ +\dfrac{1}{(\omega-\omega_0)^2+\left(\dfrac{\gamma I_0}{2L}\right)^2} \end{array}\right] \tag{63}$$

Since $R_{Load}=R_L+R_o$, the effective dynamic resistance of the free running oscillator is given by

$$\sum_{effective}|R_{tot}|=R_N(t)-R_{Load}]=R_o \tag{64}$$

where R_o is the output resistance; $R_0 - R_{tot} = 0$.

The Q of the resonator circuit is expressed as

$$Q_L = \frac{\omega L}{R_0} \tag{65}$$

The oscillator output noise power in terms of Q is given by

$$P_{noise}(f) = \frac{\omega_0^2}{2Q_L^2}\frac{|e|^2}{2\overline{R_N(t)}}\left[\frac{1}{(\omega-\omega_0)^2+\left(\frac{\omega_0^2}{4Q_L^2}\right)^2\left(\frac{|e|^2}{2\overline{R_N(t)}P_{out}^2}\right)^2} + \frac{1}{(\omega-\omega_0)^2+\left(\frac{\omega_0^2}{Q_L^2}\right)^2\left(\frac{\gamma\ I_0}{2\overline{R_N(t)}}\right)^2}\right] \tag{66}$$

Figure 12 shows the Colpitts oscillator with a series resonator and the small signal ac equivalent circuit.

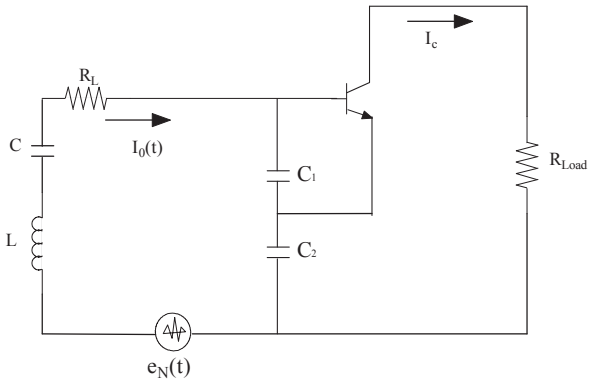

Figure 12 — Colpitts oscillator with series resonator and small signal ac equivalent circuit.

From the analytical expression of the noise analysis above, the influence of the circuit components on the phase noise can be explicitly calculated as

$$|\varphi(f)|^2 = \frac{1}{4\omega^2 L^2 I_0^2(f)}|n_1(f)|^2 \tag{67}$$

$$\frac{1}{4\omega^2 L^2 I_0^2(f)}|n_1(f)|^2 = \frac{2|e_N(f)|^2}{4\omega^2 L^2 I_0^2(f)}$$
$$\Rightarrow |\varphi(f)|^2 = \frac{2|e_N(f)|^2}{4\omega^2 L^2 I_0^2(f)} \tag{68}$$

where the frequency f varies from $-\infty$ to $+\infty$.

The resulting single sideband phase noise is

$$\pounds = \frac{|e_N(f)|^2}{4\omega^2 L^2 I_0^2(f)} \tag{69}$$

The unknown variables are $|e_N(f)|^2$ and $I_0^2(f)$, which need to be determined next. $I_0^2(f)$ will be transformed into $I_{c0}^2(f)$ by multiplying $I_0^2(f)$ with the effective current gain $Y_{21}^+/Y_{11}^+ = \beta^+$.

Calculation of $I_{c0}^2(f)$

From Figure 12, the LC-series resonant circuit is in shunt between the base and the emitter with the capacitive negative conductance portion of the transistor. We now introduce a collector load R_{Load} at the output, or better yet, an impedance Z.

The oscillator base current $i(t)$ is

$$i(t) = |I_0|\cos(\omega t) = \frac{V_{bc}(t)}{Z} \tag{70}$$

and the collector current is

$$|I_{c0}| = \left|\frac{[0.7 - V_{ce}]}{R_{Load} + j\left(\omega L - \frac{1}{\omega C_{IN}}\right)}\right| \tag{71}$$
$$\approx \left|\frac{V_{ce}}{R_{Load} + j\left(\omega L - \frac{1}{\omega C_{IN}}\right)}\right|$$

$$\overline{I_{c0}^2(f)} \approx \left\{\frac{\overline{V_{ce}^2(f)}}{[R_{Load}]^2 + \left(\omega L - \frac{1}{\omega C_{IN}}\right)^2}\right\} \tag{72}$$
$$= \left\{\frac{\overline{V_{ce}^2(f)}}{\left[\frac{\omega L}{Q}\right]^2 + \left(\omega L - \frac{1}{\omega C_{IN}}\right)^2}\right\}$$

The voltage V_{ce} is the RF voltage across the collector-emitter terminals of the transistor. Considering the steady-state oscillation $\omega \rightarrow \omega_0$, the total loss resistance is compensated by the negative resistance of the active device as $R_L = \overline{R_N(t)}$. The expression of $\left|\overline{I_{c0}^2(f)}\right|_{\omega=\omega_0}$ is

$$\left|\overline{I_{c0}^2(f)}\right|_{\omega=\omega_0} = \left|\frac{\overline{V_{ce}^2(f)}}{\left[\frac{\omega_0 L}{Q}\right]^2 + \left(\omega_0 L - \frac{1}{\omega_0 C_{IN}}\right)^2}\right| \tag{73}$$

$$= \left|\frac{\overline{V_{ce}^2(f)}}{(\omega_0 L)^2\left[\frac{1}{Q^2} + \left(1 - \frac{1}{\omega_0^2 L C_{IN}}\right)^2\right]}\right|$$

$$\left|\overline{I_{c0}^2(f)}\right|_{\omega=\omega_0}=\left|\frac{\overline{V_{ce}^2(f)}}{(\omega_0 L)^2\left[\frac{1}{Q^2}+\left(1-\frac{1}{\omega_0^2 L}\frac{C_1+C_2}{C_1C_2}\right)^2\right]}\right| \tag{74}$$

where C_{IN} is the equivalent capacitance of the negative resistor portion of the oscillator circuit.

$$C^{'}=\frac{CC_{IN}}{C+C_{IN}}, \qquad C_{IN}=\frac{C_1C_2}{C_1+C_2} \tag{75}$$

$$Q=\frac{\omega L}{R_L} \tag{76}$$

For a reasonably high Q resonator $\left|\overline{I_{c0}^2(f)}\right|_{\omega=\omega_0}\propto[C_{IN}]_{\omega=\omega_0}$

Calculation of the noise voltage $e_N(f)$

The equivalent noise voltage from the negative resistance portion of the oscillator circuit is given an open-circuit noise voltage [EMF] of the circuit as shown in Figure 13 below.

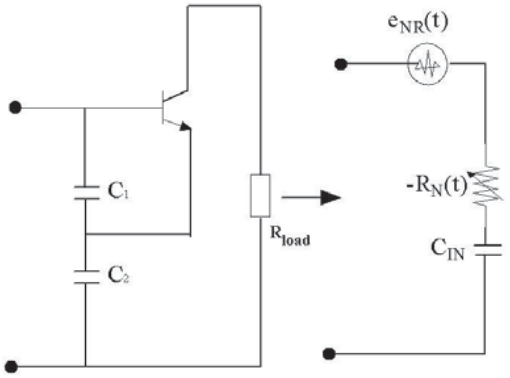

Figure 13 — Equivalent representation of negative resistance portion of the circuit at the input for the open circuit noise voltage.

The noise voltage associated with the resonator loss resistance R_s is

$$\left|\overline{e_R^2(f)}\right|_{\omega=\omega_0}=4kTBR_s \tag{77}$$

R_s denotes the equivalent series loss resistor, which can be calculated from the parallel loading resistor R_{load}, see Figure 12.

$$\left|\overline{e_R^2(f)}\right|_{\omega=\omega_0}=4kTR \text{ for } B=1 \text{ Hz bandwidth} \tag{78}$$

The total noise voltage power within 1 Hz bandwidth can be given as

$$\left|\overline{e_N^2(f)}\right|_{\omega=\omega_0}=\overline{e_R^2(f)}+\overline{e_{NR}^2(f)} \tag{79}$$

Derivation of Equation (80):

The total noise voltage power within 1 Hz bandwidth can be given as

$$\left|\overline{e_N^2(f)}\right|_{\omega=\omega_0}=\overline{e_R^2(f)}+\overline{e_{NR}^2(f)} \tag{80}$$

The first term in Equation (80) is the noise voltage power due to the loss resistance R, and the second term is associated with the negative resistance of the active device R_N.

Figure 14 and 15 illustrate the oscillator circuit for the purpose of the calculation of the negative resistance.

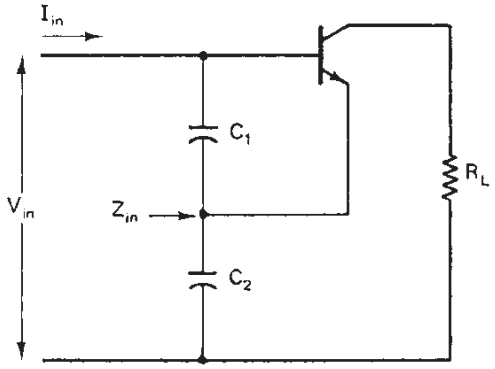

Figure 14 — Oscillator circuit for the calculation of the negative resistance.

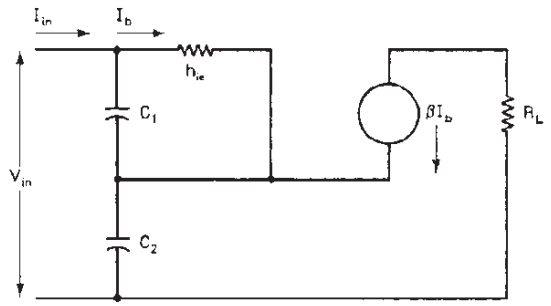

Figure 15 — Equivalent oscillator circuit for the calculation of the negative resistance.

From Figure 15, the circuit equation is given from Kirchoff's voltage law (KVL) as

$$V_{\text{in}}=I_{\text{in}}\left(X_{C_1}+X_{C_2}\right)-I_b\left(X_{C_1}-\beta X_{C_2}\right) \tag{81}$$

$$0=-I_{\text{in}}\left(X_{C_1}\right)+I_b\left(X_{C_1}+h_{ie}\right) \tag{82}$$

Considering, $\frac{1}{Y_{11}}=h_{ie}$

$$Z_{\text{in}}=\frac{V_{\text{in}}}{I_{\text{in}}}=\frac{(1+\beta)X_{C_1}X_{C_2}+h_{ie}\left(X_{C_1}+X_{C_2}\right)}{X_{C_1}+h_{ie}} \tag{83}$$

$$Z_{\text{in}} = \frac{\left(-\frac{(1+\beta)}{\omega^2 C_1 C_2} + \frac{(C_1+C_2)}{j\omega C_1 C_2}\frac{1}{Y_{11}}\right)}{\left(\frac{1}{Y_{11}} + \frac{1}{j\omega C_1}\right)} \tag{84}$$

$$Z_{\text{in}} = \frac{-jY_{11}(1+\beta) + \omega(C_1+C_2)}{\omega C_2(Y_{11} + j\omega C_1)} \tag{85}$$

$$Z_{\text{in}} = \frac{[\omega(C_1+C_2) - jY_{11}(1+\beta)][Y_{11} - j\omega C_1]}{\omega C_2(Y_{11}^2 + \omega^2 C_1^2)} \tag{86}$$

$$Z_{\text{in}} = \left[\frac{\omega Y_{11}(C_1+C_2) - (1+\beta)\omega C_1 Y_{11}}{\omega C_2(Y_{11}^2 + \omega^2 C_1^2)}\right] - j\left[\frac{Y_{11}^2(1+\beta) + \omega^2 C_1(C_1+C_2)}{\omega C_2(Y_{11}^2 + \omega^2 C_1^2)}\right] \tag{87}$$

$$Z_{\text{in}} = -R_n - jX \tag{88}$$

$$R_n = \frac{(1+\beta)\omega C_1 Y_{11} - \omega Y_{11}(C_1+C_2)}{\omega C_2(Y_{11}^2 + \omega^2 C_1^2)} = \frac{(1+\beta)C_1 Y_{11} - Y_{11}(C_1+C_2)}{C_2(Y_{11}^2 + \omega^2 C_1^2)} \tag{89}$$

$$R_n = \frac{\beta C_1 Y_{11} - Y_{11} C_2}{C_2(Y_{11}^2 + \omega^2 C_1^2)} = \frac{\beta Y_{11}}{\frac{C_2}{C_1}(Y_{11}^2 + \omega^2 C_1^2)} - \frac{Y_{11}}{(Y_{11}^2 + \omega^2 C_1^2)} \tag{90}$$

Considering $\beta = \frac{Y_{21}}{Y_{11}} \approx \frac{g_m}{Y_{11}}$

$$R_n = \frac{g_m}{\frac{C_2}{C_1}(\frac{g_m^2}{\beta^2} + \omega^2 C_1^2)} - \frac{g_m/\beta}{(\frac{g_m^2}{\beta^2} + \omega^2 C_1^2)} \tag{91}$$

$$R_n = \frac{g_m \beta^2 C_1}{(g_m^2 C_2 + \omega^2 \beta^2 C_1^2 C_2)} - \frac{g_m \beta}{(g_m^2 + \beta^2 \omega^2 C_1^2)} \tag{92}$$

$$R_n = \frac{g_m \beta^2 \omega^2 C_1 C_2}{\omega^2 C_1^2(\frac{C_2^2}{C_1^2} g_m^2 + \omega^2 \beta^2 C_2^2)} - \frac{g_m \beta \omega^2 C_2^2}{\omega^2 C_1^2(\frac{C_2^2}{C_1^2} g_m^2 + \beta^2 \omega^2 C_2^2)} \tag{93}$$

$$R_n = \left[\frac{g_m^2}{\omega^2 C_1^2(\frac{C_2^2}{C_1^2} g_m^2 + \omega^2 \beta^2 C_2^2)}\right]\left[\frac{\beta^2 \omega^2 C_1 C_2}{g_m} - \frac{\beta \omega^2 C_2^2}{g_m}\right] \tag{94}$$

$$R_n = \left[\frac{g_m^2}{\omega^2 C_1^2(\frac{C_2^2}{C_1^2} g_m^2 + \omega^2 \beta^2 C_2^2)}\right]\left[g_m\left[\left(\frac{\omega C_1}{Y_{11}}\right)\left(\frac{\omega C_2}{Y_{11}}\right) - \frac{\omega^2 C_2^2}{\beta Y_{11}^2}\right]\right] \tag{95}$$

$$R_n = \left[\frac{g_m^2}{\omega^2 C_1^2(\frac{C_2^2}{C_1^2} g_m^2 + \omega^2 \beta^2 C_2^2)}\right]\left[g_m\left[\left(\frac{\omega C_1}{Y_{11}}\right)\left(\frac{\omega C_2}{Y_{11}}\right) - \frac{1}{\beta}\left(\frac{\omega C_2}{Y_{11}}\right)\left(\frac{\omega C_2}{Y_{11}}\right)\right]\right] \tag{96}$$

Considering $\left(\frac{\omega C_1}{Y_{11}}\right)\left(\frac{\omega C_2}{Y_{11}}\right) >> \frac{1}{\beta}\left(\frac{\omega C_2}{Y_{11}}\right)\left(\frac{\omega C_2}{Y_{11}}\right)$

and $\left(\frac{\omega C_1}{Y_{11}}\right)\left(\frac{\omega C_2}{Y_{11}}\right) \approx 1$ (97)

$$\left[g_m\left[\left(\frac{\omega C_1}{Y_{11}}\right)\left(\frac{\omega C_2}{Y_{11}}\right) - \frac{1}{\beta}\left(\frac{\omega C_2}{Y_{11}}\right)\left(\frac{\omega C_2}{Y_{11}}\right)\right]\right] \tag{98}$$

$$\cong \frac{I_C}{V_T} = \frac{I_C}{kT/q} \Rightarrow \frac{qI_C}{kT}$$

From (96) and (98)

$$R_n = \left[\frac{g_m^2}{\omega^2 C_1^2(\frac{C_2^2}{C_1^2} g_m^2 + \omega^2 \beta^2 C_2^2)}\right]\frac{qI_C}{kT} \tag{99}$$

From (80), the total noise voltage power within a 1 Hz bandwidth can be given as

$$\left|\overline{e_N^2(f)}\right|_{\omega=\omega_0} = \overline{e_R^2(f)} + \overline{e_{NR}^2(f)} \tag{100}$$

$$\left|\overline{e_N^2(f)}\right|_{\omega=\omega_0} = [4kTR] + \left[\frac{4qI_c g_m^2 + \frac{K_f I_b^{AF}}{\Delta\omega} g_m^2}{\omega_0^2 C_1^2(\omega_0^2(\beta^+)^2 C_2^2 + g_m^2 \frac{C_2^2}{C_1^2})}\right] \tag{101}$$

where

$\beta^+ = \left[\frac{Y_{21}^+}{Y_{11}^+}\right]\left[\frac{C_1}{C_2}\right]^p$, $g_m = [Y_{21}^+]\left[\frac{C_1}{C_2}\right]^q$, redefined

$$\left|\overline{e_N^2(f)}\right|_{\omega=\omega_0}=[4kTR]+\left[\frac{4qI_{c0}g_m^2+\frac{K_fI_b^{AF}}{\Delta\omega}g_m^2}{\omega_0^2C_1^2(\omega_0^2(\beta^+)^2C_2^2+g_m^2\frac{C_2^2}{C_1^2})}\right] \quad (102)$$

where

$$\beta^+=\left[\frac{Y_{21}^+}{Y_{11}^+}\right]\left[\frac{C_1}{C_2}\right]^p,\ g_m=\left[Y_{21}^+\right]\left[\frac{C_1}{C_2}\right]^q,\quad \text{redefined.}$$

The values of p and q depend upon the drive level.

The flicker noise contribution in Equation (80) is introduced by adding term $\frac{K_fI_b^{AF}}{\Delta\omega}$ in I_{c0}, where K_f is the flicker noise coefficient and AF is the flicker noise exponent. This is valid only for the bipolar transistor. For an FET, the equivalent currents have to be used.

In this case we use a value of 10^{-8}, some publications claim much smaller numbers such as 10^{-11}. The authors must have done some magic to get the measured curve fitted. In my opinion these small numbers violate the laws of physics for bipolar transistors.

The first term in the expression above is related to the thermal noise due to the loss resistance of the resonator tank and the second term is related to the shot noise and flicker noise in the transistor.

Now, the phase noise of the oscillator can be expressed as

$$\left|\overline{\varphi^2(\omega)}\right|=\frac{2\left|\overline{e_N^2(\omega)}\right|}{4\omega_0^2L^2I_0^2(\omega)} \quad (103)$$

$$\left|\overline{\varphi^2(\omega)}\right|_{SSB}=\frac{1}{2}\left|\overline{\varphi^2(\omega)}\right|=\frac{\left|\overline{e_N^2(\omega)}\right|}{4\omega_0^2L^2I_0^2(\omega)} \quad (104)$$

$$\left|\overline{\varphi^2(\omega)}\right|_{SSB}=\left\{[4kTR]+\left[\frac{4qI_cg_m^2+\frac{K_fI_b^{AF}}{\omega}g_m^2}{\omega_0^2C_1^2(\omega_0^2(\beta^+)^2C_2^2+g_m^2\frac{C_2^2}{C_1^2})}\right]\right\} \quad (105)$$
$$\left[\frac{(\omega_0)^2\left[\frac{1}{Q^2}+\left(1-\frac{1}{\omega_0^2L}\frac{C_1+C_2}{C_1C_2}\right)^2\right]}{4\omega^2\left|V_{ce}^2(\omega)\right|}\right]$$

$$\left|\overline{\varphi^2(\omega)}\right|_{SSB}=\left[4kTR+\left[\frac{4qI_cg_m^2+\frac{K_fI_b^{AF}}{\omega}g_m^2}{\omega_0^2C_1^2(\omega_0^2(\beta^+)^2C_2^2+g_m^2\frac{C_2^2}{C_1^2})}\right]\right] \quad (104)$$
$$\left[\frac{\omega_0^2}{4\omega^2V_{ce}^2}\right]\left[\frac{1}{Q^2}+\left(1-\frac{1}{\omega_0^2L}\frac{C_1+C_2}{C_1C_2}\right)^2\right]$$

Considering

$\left(\frac{1}{\omega_0^2L}\frac{C_1+C_2}{C_1C_2}\right)>>1$; for

$\omega_0=2\pi f=6.28\times10^{-9}$ Hz, $L=10^{-9}$ H , $C_1=10^{-12}$ F, $C2=10^{-12}$ F

$\left(\frac{1}{\omega_0^2L}\frac{C_1+C_2}{C_1C_2}\right)=50.7$.

Since the phase noise is always expressed in dBc/Hz, we now calculate, after simplification of Equation (84),

$$£(\omega)=10\log\left\{\left[4kTR+\left[\frac{4qI_cg_m^2+\frac{K_fI_b^{AF}}{\omega}g_m^2}{\omega_0^2C_1^2(\omega_0^2(\beta^+)^2C_2^2+g_m^2\frac{C_2^2}{C_1^2})}\right]\right]\left[\frac{\omega_0^2}{4\omega^2V_{cc}^2}\right]\left[\frac{1}{Q^2}+\frac{[C_1+C_2]^2}{C_1^2C_2^2\omega_0^4L^2}\right]\right\} \quad (107)$$

For the bias condition (which is determined from the output power requirement), the loaded quality factor, and the device parameters [transconductance and β^+], the best phase noise can be found by differentiating $\left|\overline{\varphi^2(\omega)}\right|_{SSB}$ with respect to C_1/C_2 .

Considering that all the parameters of $\left|\overline{\varphi^2(\omega)}\right|_{SSB}$ are constants for a given operating condition (except the feedback capacitor), the minimum value of the phase noise can be determined for any fixed value of C_1 as

$$\left|\overline{\varphi^2(\omega)}\right|=\left[k_0+\frac{k_1}{k_2C_1^2C_2^2+k_3C_2^2}\right]\left[\frac{C_1+C_2}{C_1C_2}\right]^2 \quad (108)$$

$$k_0=\frac{kTR}{\omega^2\omega_0^2L^2V_{ce}^2} \quad (109)$$

$$k_1=\frac{qI_{c0}g_m^2+\frac{K_fI_b^{AF}}{\omega}g_m^2}{\omega^2\omega_0^2L^2V_{ce}^2} \quad (110)$$

$$k_2=\omega_0^4(\beta^+)^2 \quad (111)$$

$$k_3 = g_m^2 \tag{112}$$

Where k_1, k_2, and k_3, are constant only for a particular drive level, with $y = C_1/C_2$. Making k_2 and k_3 also dependent on *y*, as the drive level changes, the final noise equation is

$$\pounds(\omega) = 10 \times \log \left[\left[\left[k_0 + \left(\frac{k^3 k_1 \left[\frac{Y_{21}^+}{Y_{11}^+} \right]^2 [y]^{2p}}{\left[Y_{21}^+ \right]^3 [y]^{3q}} \right) \right] \left[\frac{[1+y]^2}{y^2} \right] \right] \left(\frac{1}{(y^2 + k)} \right) \right] \tag{113}$$

where

$$k_0 = \frac{kTR}{\omega^2 \omega_0^2 L^2 V_{cc}^2}$$

$$k_1 = \frac{qI_c g_m^2 + \dfrac{K_f I_b^{AF}}{\omega} g_m^2}{\omega^2 \omega_0^4 L^2 V_{cc}^2}$$

$$k_2 = \omega_0^2 (\beta^+)^2$$

Figure 16 shows the simulated phase noise and its minimum for two values of C_1, 2 pF and 5 pF. 5 pF, provides a better phase noise and a flatter response. For larger C_1, the oscillator will cease to oscillate.

$$\frac{\partial \left| \phi^2(\omega, y, k) \right|}{\partial y} \Rightarrow 0$$

$$\frac{\partial}{\partial y} \left\{ \left[\left[k_0 + \left(\frac{k^3 k_1 \left[\frac{Y_{21}^+}{Y_{11}^+} \right]^2 [y]^{2p}}{\left[Y_{21}^+ \right]^3 [y]^{3q}} \right) \left(\frac{1}{(y^2 + k)} \right) \right] \right\} \right\}_{y=m} \Rightarrow 0 \tag{114}$$

From curve-fitting attempts, the following values for *q* and *p* in Equation (114) were determined:

q=1 to 1.1; *p* = 1.3 to 1.6.

q and *p* are a function of the normalized drive level *x* and need to be determined experimentally.

The transformation factor *n* is defined as

$$n = 1 + \frac{C_1}{C_2} \rightarrow 1 + y \tag{115}$$

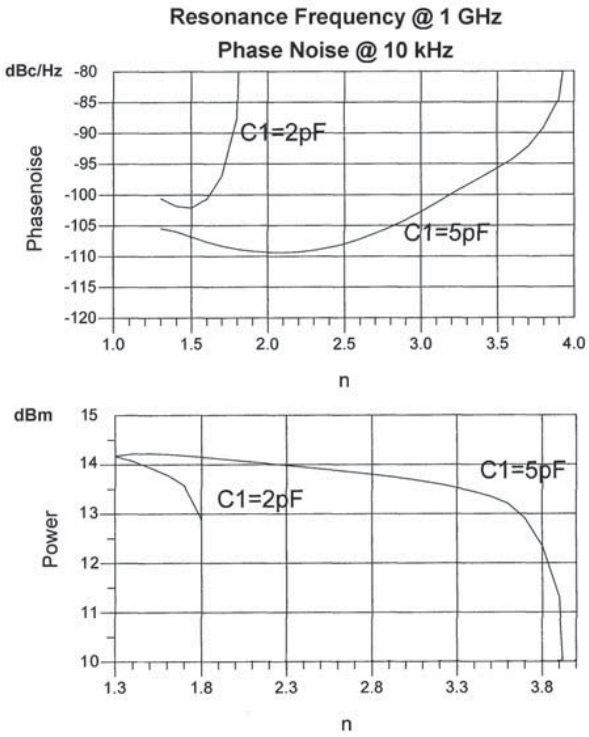

Figure 16 — Phase noise vs. *n* and output power.

The following plot in Figure 17 shows the predicted phase noise resulting from Equation (114). For the first time, the flicker corner frequency was properly implemented and gives answers consistent with the measurements. In the following chapter all the noise sources will be added, but the key contributors are still the resonator noise and the flicker noise. The Schottky noise dominates further out. The break point for the flicker noise can be clearly seen.

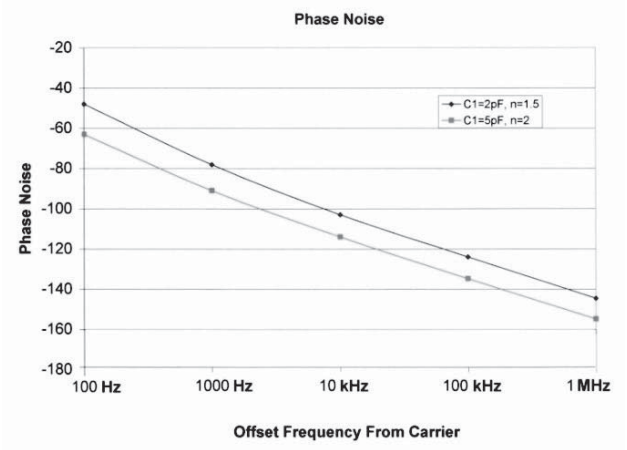

Figure 17 — Using Equation (114), the phase noise for different values of *n* for constant C_2 can be calculated.

Summary Results

The analysis of the oscillator in the time domain has given us a design criteria to find the optimum value of

$y = C_1/C_2$ with values for $y + 1$ (or n) ranging from 1.5 to 4. For values above 3.5, the power is reduced significantly.

Consistent with the previous chapters, we note

$$C_1 = C_1^* \pm X(C_P \text{ or } L_P) \tag{116}$$

$$X(C_{be} \text{ or } L_b) \rightarrow C_P \text{ or } L_P \tag{117}$$

In the case of a large value of C_P (C_P>C_1), X_1 has to be inductive to compensate extra contributions of the device package capacitance to meet the desired value of C_1!

The following is a set of design guides to calculate the parameters of the oscillator.

$$\omega = \sqrt{\frac{1}{L\left[\frac{C_1C_2}{C_1+C_2}+C\right]}} \tag{118}$$

$$\left|R_n(L_P=0)\right| = \frac{Y_{21}}{w^2C_1C_2} \tag{119}$$

$$C_1 = \frac{1}{w_0}\sqrt{\frac{Y_{11}}{K}} \tag{120}$$

C_2 is best be determined graphically from the noise plot.

$$C_C > \left\{\frac{(w^2C_1C_2)(1+w^2Y_{21}^2L_P^2)}{[Y_{21}^2C_2 - w^2C_1C_2)(1+w^2Y_{21}^2L_P^2)(C_1+C_P+C_2)]}\right\} \tag{121}$$

$$\frac{C}{10} \geq [C_C]_{L_P=0} > \left[\frac{(w^2C_1C_2)}{[Y_{21}^2C_2 - w^2C_1C_2)(C_1+C_P+C_2)]}\right] \tag{122}$$

The phase noise in dBc/Hz is shown as

$$\pounds(\omega) = 10\times\log\left[\left[k_0 + \left(\frac{k^3k_1\left[\frac{Y_{21}^+}{Y_{11}^+}\right]^2[y]^{2p}}{\left[Y_{21}^+\right]^3[y]^{3q}}\right)\left(\frac{1}{(y^2+k)}\right)\right]\left[\frac{[1+y]^2}{y^2}\right]\right] \tag{123}$$

The phase noise improves with the square of the loaded Q_L! 10% higher $Q \rightarrow$ 20% better phase noise!

$$L(\omega) \propto \frac{1}{C_{IN}^2} \tag{124}$$

The loaded Q of the resonator determines the minimum possible level of the oscillator phase noise for given bias voltage and oscillator frequency.

To achieve close to this minimum phase noise level set by the loaded Q_L of the resonator, the optimum (rather, how large the value of the C_{IN} can be) value of C_{IN} is to be fixed.

To achieve the best possible phase noise level, the feedback capacitors C_1 and C_2 should be made as large as possible, but still generate sufficient negative resistance for sustaining steady-state oscillation.

$$[-R_N]_{\substack{\text{negative}\\ \text{resistance}}} \propto \frac{1}{\omega_0^2}\frac{1}{C_1C_2}, \text{ (no parasitics)} \tag{125}$$

The negative resistance of the oscillator circuit is inversely proportional to the feedback capacitors. Therefore, the limit of the feedback capacitor value is determined by the minimum negative resistance for a loop gain greater than unity.

From the phase noise equation discussed, the feedback capacitor C_2 has more influence compared to C_1. The drive level and conduction angle of the Colpitts oscillator circuit is a strong function of C_2.

The time domain approach has provided us with the design guide for the key components of the oscillator; however, it did not include all the noise sources of the transistor. By using the starting parameters, such as C_1 and C_2 and the bias point, as well as the information about the resonator and the transistor, a complete noise model/analysis will now be shown.

The time domain approach has provided us with the design guide for the key components of the oscillator; however, it did not include all the noise sources of the transistor. By using the starting parameters, such as C_1 and C_2 and the bias point, as well as the information about the resonator and the transistor, a complete noise model/analysis will be shown now.

After some lengthy calculations and approximations, adding shot noise, flicker noise and the loss resistor, the equivalent expression of the phase noise can be derived as

$$\pounds(\omega) = \left[\begin{array}{c} 4kTR + \\ \dfrac{\left|g_m^2(t)\right|(4qI_c) + \left|g_m^2(t)\right|\left(\dfrac{K_fI_b^{AF}}{\omega}\right)}{\omega_0^4\beta^2C_{ce}^2(C_2+C_{b'e}-L_1C_2C_{be}\omega_0^2)^2 + \left|g_m^2(t)\right|\omega_0^2(C_2+C_{b'e}-L_1C_2C_{b'e}\omega_0^2)^2} \end{array}\right] \times \frac{\omega_0^2}{4\omega^2V_{ce}^2}\left[\frac{Q_0^2}{Q_L^2} + \left(1-\frac{1}{\omega_0^2L_1}\left(\frac{[(C_2+C_{b'e}-L_1C_2C_{b'e}\omega_0^2)+C_{ce}]}{C_{ce}[(C_2+C_{b'e}-L_1C_2C_{b'e}\omega_0^2)]}\right)\right)^2\right] \tag{126}$$

The flicker noise contribution in equation (126) is introduced by adding term $K_f I_b^{AF} / \omega$ in RF collector current I_C, where K_f is the flicker noise coefficient and *AF* is the flicker noise exponent. This is valid only for the bipolar transistor. For an FET, the equivalent current transformations have to be used.

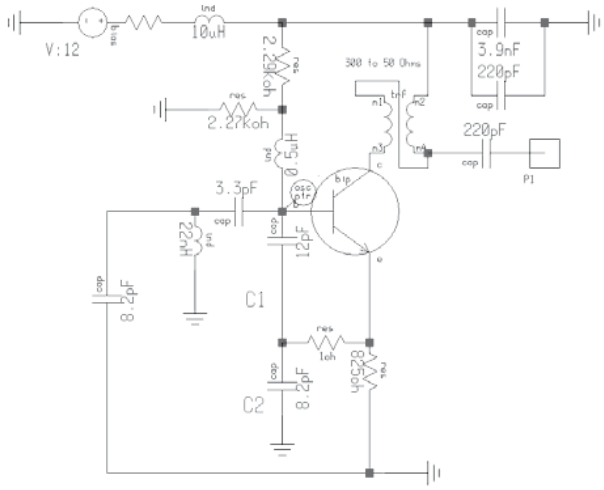

Figure 18 — Colpitts Configuration – Test Circuit.

This is the most complete noise model derived and tested.

Validation

After so many calculations a proof of concept is called for [14-20]. Figure 18 shows the test circuit. It is the typical Colpitts oscillator with the RF output taken from the collector. The transistor BFG 520 is made by Philips and is a 9 GHz NPN device used at a small fraction of I_C max.

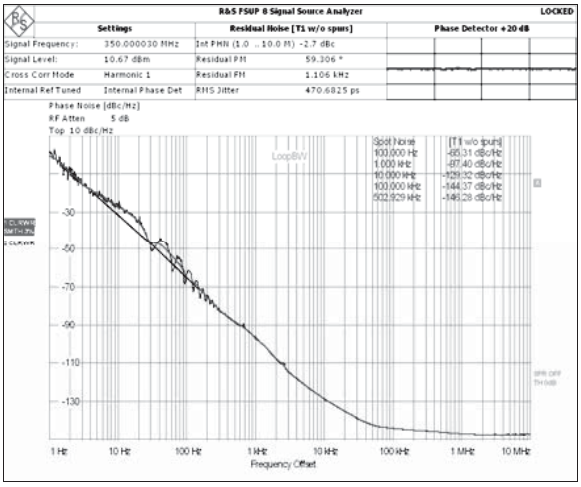

Figure 19: Measured Data for a 350MHz Oscillator.

The measured phase noise data is shown in Figure 19 and the simulated data in Figure 20. When applying the analytical noise equation we obtain good agreement with the actual measurements also.

This proves that the calculations are valid, any one need not spend $ 25,000 for a Harmonic Balance based simulator.

The phase noise, far out, is limited by the needed isolation/buffer stage.

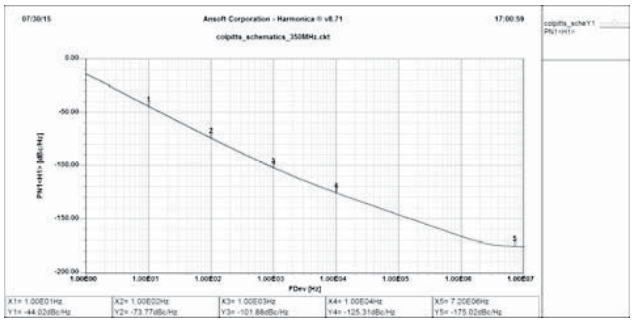

Figure 20 — Simulated Phase Noise Data for the test circuit of Figure 18.

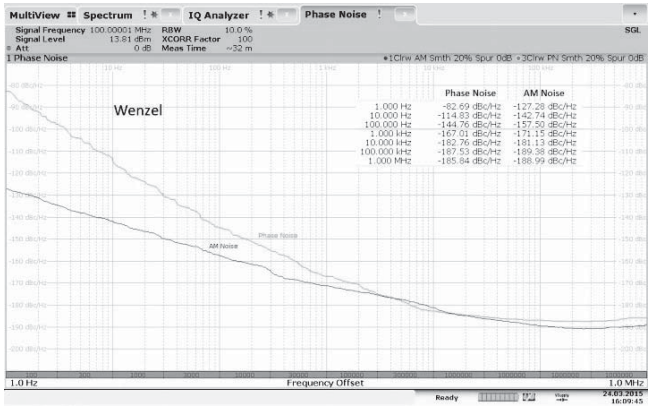

Figure 21 — Phase Noise Measurements (AM and FM noise) of a popular Wenzel 100 MHz Crystal Oscillator.

With the latest test equipment (R&S FSWP) FM and AM noise can be measured separately. Using a popular crystal oscillator at 100 MHz made by Wenzel, both AM and FM components can be inspected.

There is an area where the AM noise (unfortunately) is larger than the FM noise. That indicates the internal buffer stage is partially driven into saturation. By changing some component values this can be avoided.

$Ic = 6.2\cdot10^{-3}$ $Ib = 43.2\cdot10^{-6}$ $L = 22\cdot10^{-9}$ $C_1 = 12\cdot10^{-12}$ $C_2 = 8.2\cdot10^{-12}$ $C_c = 3.3\cdot10^{-12}$

$qcharge = 1.602\cdot10^{-19}$ $T = 300\ K = 1.3806\cdot10^{-23}$ $R = 0.3$ $kf = 1\cdot10^{-7}$ $af = 2$ $KT = 4.143\cdot10^{-21}$

$Qmac = 120$ $Q = 60$ $Vt = 12$ $f = 350\cdot10^{6}$ $w0 = 2\pi\cdot f$ $\beta = 140$ $y21 = (0.193 - 0.0051j)$

$i = 0..7$ $fo_i = 10^i$ $r_e = \frac{26\cdot10^{-3}}{Ic}$ $gm1 = \frac{1}{r_e}$ $gm1 = 0.238$ $y11 = (0.00141 + 0.000984j)$

$wo_i = 2\cdot\pi\cdot fo_i$

$$Lw_i = 10\cdot\log\left[\left[4\cdot KT\cdot R + \left[\frac{4\cdot qcharge\cdot Ic\cdot gm1^2 + \frac{kf\cdot Ib^{af}}{wo_i}\cdot gm1^2}{(w0)^2\cdot C_1^2\cdot\left[(w0)^2\cdot\beta^2\cdot C_2^2 + gm1^2\cdot\frac{C_2^2}{C_1^2}\right]}\right]\right]\cdot\left[\frac{w0^2}{4\cdot(wo_i)^2\cdot Vt^2}\cdot\left[\frac{1}{Q^2} + \frac{(C_1 + C_2)^2}{C_1^2\cdot C_2^2\cdot(w0)^4\cdot L^2}\right]\right]\right]$$

fo_i	Lw_i
1	-5.227
10	-35.222
100	-65.165
$1\cdot10^3$	-94.633
$1\cdot10^4$	-121.303
$1\cdot10^5$	-143.272
$1\cdot10^6$	-163.529
$1\cdot10^7$	-183.555

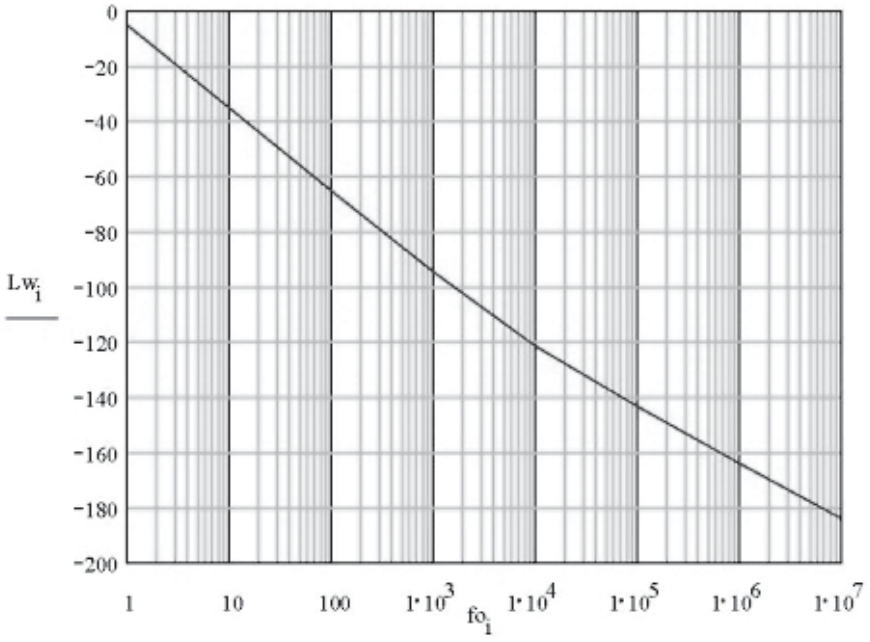

Figure 22 — Mathcad Worksheet for calculated Phase Noise of a 350 MHz Colpitts Oscillator.

The MathCad worksheet, Eqn_107_350MHz.mcd file, can be found at **www.arrl.org/QEXfiles.**

References

[1] **www.scribd.com/doc/213845621/Communication-Circuits-Clarke-Hess#scribd**

[2] **rfic.eecs.berkeley.edu/~niknejad/ee242/pdf/eecs242_lect22_phasenoise.pdf**.

[3] **https://en.wikipedia.org/wiki/Barkhausen_stability_criterion**.

[4] U. L. Rohde, A. K. Poddar, *The Design of Modern Microwave Oscillators*, John Wiley, 2005.

[5] U. L. Rohde, M. Rudolph, *RF/Microwave Circuit Design for Wireless Applications*, Wiley, New York, 2013.

[6] Agilent Phase Noise Measurement Solution (**www.home.agilent.com/agilent/application**)

[7] R. G. Rogers, *Low Phase Noise Microwave Oscillator Design*, Artech House, Inc. 1991.

[8] Enrico Rubiola, "Phase Noise and Frequency Stability in Oscillators", Cambridge University Press, 2010.

[9] U. L. Rohde and A. K. Poddar, "An Analytical Approach of Minimizing VCO Phase Noise," Asia-Pacific Microwave Conference, China, December 4-7, 2005.

[10] U. L. Rohde and A. K. Poddar, "Noise Minimization Techniques for RF & MW Signal Sources (Oscillators/VCOs)", Microwave Journal, Sept. 2007.

[11] U. L. Rohde and A. K. Poddar, "Techniques Minimize the Phase Noise in Crystal Oscillators", 2012 IEEE FCS, pp. 01-07, May 2012.

[12] Marvin E. Frerking, *Crystal Oscillator Design and Temperature Compensation*, Van Nostrand Reinhold Company ISBN: 0-442-22459-1

[13] Brendon Bentley, "An Investigation into the Phase Noise of Quartz Crystal Oscillators", MS Thesis, Stellenbosch University, March 2007.

[14] Ajay Poddar, Ulrich Rohde, Anisha Apte, " How Low Can They Go, Oscillator Phase noise model, Theoretical, Experimental Validation, and Phase Noise Measurements", IEEE Microwave Magazine, Vol. 14, No. 6, pp. 50-72, Sep/Oct 2013.

[15] Ulrich Rohde, Ajay Poddar, Anisha Apte, "Getting Its Measure", IEEE Microwave Magazine, Vol. 14, No. 6, pp. 73-86, Sep/Oct 2013.

[16] Grant Moulton, "Analysis and Prediction of Phase Noise in Resonators and Oscillators", Hewlett Packard, (**citeseerx.ist.psu.edu/viewdoc/download?doi=10.1.1.309.5449&rep=rep1&type=pdf**).

[17] **www.ieee-uffc.org/frequency-control/learning/pdf/everard.pdf**.

[18] K. Kurokawa, " Noise in Synchronized Oscillators," IEEE Trans. on MTT, Vol. 16, pp. 234-240, Ap 1968.

[19] V. Rizzoli, F. Mastri, C. Cecchefti, "Computer-Aided Noise Analysis of MESFET and HEMT Mixers," IEEE Trans. Microwave Theory and Techniques, Vol. MTT-37, pp 1401-1410, Sep 1989.

[20] A. Apte, V. Madhavan, A. Poddar**,** U. Rohde, T. Itoh, "A Novel Low Phase Noise X-band Oscillator", IEEE BenMAS 2014, Drexel Univ., Philadelphia.

The IEEE Microwave Theory and Techniques Society (MTT-S) awarded the 2016 Microwave Application Award to Dr. Ulrich L. Rohde, N1UL / DJ2LR, for

"*Significant contributions to the development of low-noise oscillators*".

The Microwave Application Award recognizes an individual, or a team, for an outstanding application of microwave theory and techniques, which has been reduced to practice nominally 10 years before the award.

Upcoming Conferences

Society of Amateur Radio Astronomers Western Regional Conference

March 11-13, 2016, Prescott, Arizona

www.radio-astronomy.org

The Society of Amateur Radio Astronomers (SARA) announces a regional conference will be held at Embry-Riddle Aeronautical University in Prescott, Arizona, March 11 – 13, 2016. SARA member Ray Fobes is a Staff Radio Astronomer at the University and is coordinating the event. He can be reached by e-mail at **westernconference@radio-astronomy.org**.

Expected papers include topics on radio astronomy hardware, software, education, research strategies, philosophy, observing efforts and methods.

Registration for the 2016 Western Conference is $60.00. This includes breakfast and lunch Saturday and Sunday. Checks payable to SARA Treasurer should be mailed to at 904 Towering Oak Court, Purcellville, VA 20132. Please include an e-mail address so a confirmation can be sent upon receipt of payment. Payment can also be made through **PayPal**. See website for details.

You can receive a reduced hotel rate at the SpringHill Suites by Marriott, 200 East Sheldon Street, Prescott, Arizona. When you call, ask for the "Embry-Riddle Friends" rate. 928-776-0998; **www.marriott.com/prcsh.**

See website for information.

MicroHAMS Digital Conference 2016

March 19, 2016, Redmond, Washington

www.microhams.com/mhdc/

Check website for information.

VHF Super Conference

April 15-17, 2016, Sterling, Virginia

www.vhfsuperconference.com

Sponsored by Southeastern VHF Society, North East Weak Signal Group, and the Mt Airy VHF Radio Club; hosted by the Grid Pirates Contest Group and Directive Systems and Engineering.

The conference will be held April 15-17, 2016 at the Holiday Inn, Washington-Dulles International Airport, 45425 Holiday Drive, Sterling, Virginia.

Hotel rooms are $89 (plus tax) for either king or double through March 15, 2016. Breakfast is included for Friday and Saturday and will be held privately in the conference room area for conference attendees only. Please call hotel at 1-877-875-9823 and mention code E06, or visit **vhfsuperconference.com/hotel/** to booking hotel reservations.

Conference registration, early bird discount! Sign up before March 15, 2016 and registration with lunch, all day beverages and *Proceeding* for both days will be $89. Sign up for the banquet before March 15, 2016 and the cost is $39. (A combined savings of $20.)

After March 15, registration will increase to $99, and the banquet cost will increase to $49.

A microwave, loop Yagi workshop will also be offered during the weekend. For an additional fee, understand how loop Yagis work, how to adjust them and build one with guidance from W8ZN and K4MEP of Directive Systems and Engineering. Choose a band from 902 MHz to 3456 MHz.

There will be free shuttle service to the Udvar-Hazy Air & Space Museum on Thursday April 14, 2016. Family programs also available on April 14 and 15.

See website for information.

Call for Papers

We're looking for presentations and/or papers on VHF, UHF, microwaves, and higher. All aspects are welcome — operating, contesting, homebrewing, software, EME, surplus, antennas, test equipment, amplifiers, SDR, 47 GHz superregen, whatever.

N2CEI and W1GHZ will be coordinating the *Proceedings*. Submissions and questions to: **scpapers@downeastmicrowave.com**

50th Anniversary Central States VHF Society Conference

July 28 – 31, 2016, Rochester, Minnesota

www.csvhfs.org

Call for Papers

The Central States VHF Society is soliciting papers, presentations, and poster displays for the 50th Annual CSVHFS Conference to be held in Rochester, Minnesota, July 28 – 31, 2016. Papers, presentations, and posters on all aspects of weak signal VHF and above Amateur Radio are requested. You do not need to attend the conference, nor present your paper, to have it published in the *Proceedings*.

• Posters will be displayed during the two days of the Conference.

• Topics of interest include (but are not limited to):

• Antennas — including Modeling/Design, Arrays, and Control

• Construction of equipment, such as transmitters, receivers, and transverters

• RF amplifiers (power amps) including single-band and multi-band vacuum tube and solid-state

• Pre-amplifiers (low noise)

• Propagation, including ducting, sporadic-E, and meteor scatter, etc.

• Test Equipment — including homebrew, using, and making measurements

• Regulatory topics

• Operating — including contesting, roving, and DXpeditions

• EME

• Digital Signal Processing (DSP)

• Software-defined Radio (SDR)

• Digital Modes — such as WSJT, JT65, etc.

Generally, topics not related to weak signal VHF, such as FM Repeaters and packet-radio, are not accepted for presentation or publication. However, there are always exceptions.

Please contact either the *Technical Program* Chairman, Barry Malowanchuk, ve4ma@shaw.ca, or the *Proceedings* Chairman, Glen Overby, kc0iyt@arrl.net.

Deadline for submissions:

For the *Proceedings*: **Sunday, May 22, 2016**

For Presentations to be delivered at the conference: **Tuesday, July 5, 2016**

For Posters to be displayed at the conference: **Thursday, July 29, 2026**

Further information is available at the CSVHFS web site (**www.csvhfs.org**), "The 2016 Conference," and "Guidance for Proceedings Authors," "Guidance for Presenters," and "Guidance for Table-top/ Poster Displays."

2016 Society of Amateur Radio Astronomers Annual Conference

July 10-13, 2016, Green Bank, West Virginia
radio-astronomy.org

The Society of Amateur Radio Astronomers (SARA) solicits papers for presentation at its 2016 Annual Conference to be held July 10 – 13, 2016. Sunday July 10, will start with an introduction to Radio Astronomy at the Jansky Auditorium, followed by learning to operate the forty foot radio telescope — 1,420 MHz (21 cm).

Presentations by SARA members and guests are scheduled on Monday and Tuesday. A high tech tour of the NRAO facility will be conducted on Tuesday July 12.

Papers are welcome on subjects directly related to radio astronomy including hardware, software, education and tutorials, research strategies, observations and data collection and philosophy. SARA members and supporters wishing to present a paper should e-mail a letter of intent, including a proposed title and abstract to the conference coordinator at **vicepres@radio-astronomy.org** no later than April 20, 2016.

Drafts of papers are due May 4, and final versions of the papers due no later than May 18. Be sure to include your full name, affiliation, postal address, email address, and indicate your willingness to attend the conference to present your paper. Submitters will receive an email response, typically within one week.

Guidelines for presenter papers are located at: **radio-astronomy.org/pdf/guidelines-submitting-papers.pdf**

NEW!

ARRL's

Portable Antenna Classics

Thirty antennas to get you on the air from anywhere!

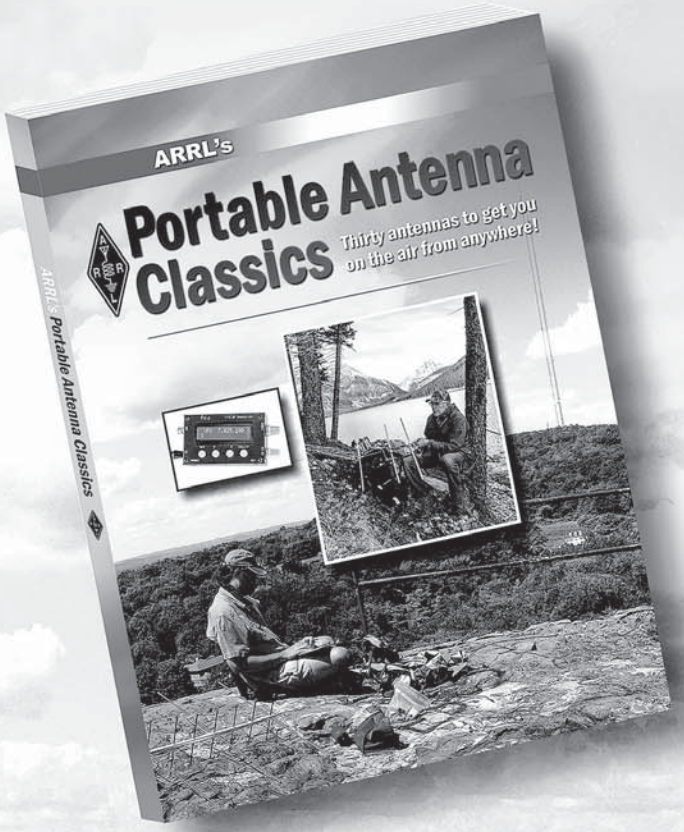

Portable operating is gaining popularity in the Amateur Radio community. For amateurs who are unable to install permanent outdoor antennas at home, portable installtions are often the only way they can get on the air. There are also amateurs who simply enjoy operating outdoors, in nature. For them, portable antennas are necessities.

ARRL's Portable Antenna Classics is a collection of helpful articles gathered from more than three decades of *QST*, ARRL's membership journal. Featuring easily constructed antenna systems that offer adequate performance, this book offers practical ideas and projects to get you on the air from anywhere:

HF Antennas
Single and multiband designs for all bands from 80 through 10 meters.

VHF/UHF Antennas
Antennas for 6 meters, 2 meters and even 70 centimeters.

Masts and Other Supports
Ingenious ideas for getting your portable antenna off the ground and keeping it there.

ARRL Item No. 0345
Special Member Price!
Only $19.95 (retail $22.95)

ARRL The national association for AMATEUR RADIO®

www.arrl.org/shop

Toll-Free US 888-277-5289,
or elsewhere +1-860-594-0355

QEX 3/2016

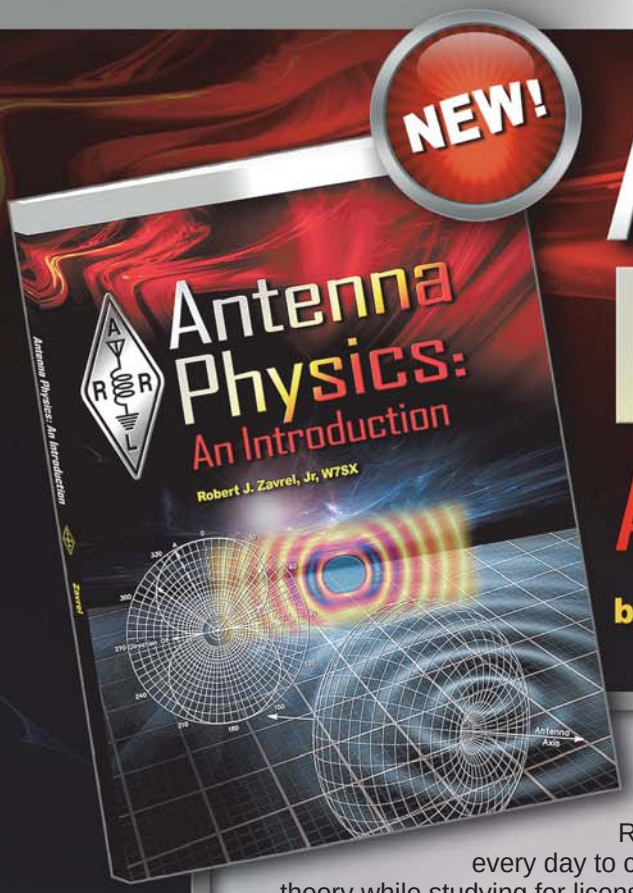

Antenna Physics: An Introduction

by Robert J. Zavrel, Jr, W7SX

Delve Deeper into Antenna Theory

Radio amateurs are familiar with antennas and use them every day to communicate on the air. We learned some basic antenna theory while studying for license exams, and most of us have built an antenna or two. We know the basics and turn to the *ARRL Handbook*, *ARRL Antenna Book*, and other general texts when thinking about our next antenna project.

We know how long to make a dipole or vertical antenna for a particular frequency, but do we know how the antenna really works? ***Antenna Physics: An Introduction*** was written to bridge the gap between basic theory and graduate-level engineering texts. **Robert J. Zavrel**, **Jr**, **W7SX**, a well-known author and professional antenna engineer, explains many of the underlying principles of antennas and antenna physics and introduces the reader to the mathematics behind these principles. Note that this is not a book of "how-to" projects, but rather a theoretical and mathematical approach to the topic.

Although some competence in mathematics is required to get the most from this book, readers may follow along and understand the concepts without needing to solve the complex equations presented. In later chapters, examples tie the concepts learned in earlier chapters to a number of antenna types familiar to radio amateurs.

Includes:

Antenna Physics

- Development of Antenna Physics
- Fundamentals
- Radiation of Radio Waves
- Transmission Line
- Antennas Using Multiple Sources

Applied Antenna Physics

- Dielectric Effects Upon Radio Waves
- Vertical Antennas
- Yagi-Uda and Cubical Quad Antennas
- Specialized Antenna Configurations
- Noise, Temperature, and Signals

Antenna Physics: An Introduction
ARRL Item No.0499
Only $29.95 plus shipping and handling

ARRL The national association for AMATEUR RADIO®

www.arrl.org/shop

Toll-Free US 888-277-5289 or elsewhere +1-860-594-0355

QEX 3/2016

Quicksilver Radio

Test Equipment

USB Microscope

Up to 500X magnification. Captures still images and records live video. Built in LED Lighting. A must for working on suface mount components.

Wireless Relay Switch

200'+ Range. We have single, four, and eight channel models.

GO-PWR Plus™

Portable power to go or backup in the shack. Includes Powerpoles, bright easy to read meter, and lighted switch. For U1 size (35 ah) and group 24 (80 ah) batteries.

Digital Voltmeter/ Ammeter

Two line display shows both current and voltage. Included shunt allows measurement up to 50A and 99V. Snaps into a panel to give your project a professional finish.

LCR and Impedance Meter

Newest Model. Analyzes coils, capacitors, and resistors. Indicates complex impedance and more.

Automatic Passive Component Analyzer

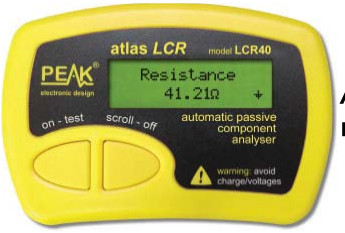

Analyzes coils, capacitors, and resistors.

Advanced Semiconductor Component Analyzer

Analyzes transistors, MOSFETs, JFETs, IGBTs, and more. Graphic display. Enhanced functionality with included PC software.

Semiconductor Component Analyzer

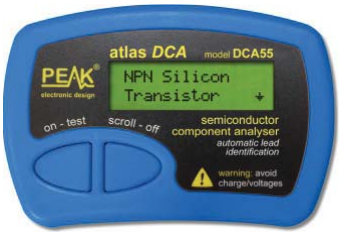

Analyzes transistors, MOSFETs, JFETs and more. Automatically determines component pinout.

Capacitance and ESR Meter

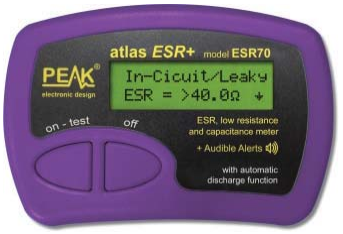

Analyzes capacitors, measures ESR.

Get All Your Ham Shack Essentials at Quicksilver Radio Products. Safe and Secure Ordering at:

www.qsradio.com